3-21-2013

Design of a Control Moment Gyroscope Attitude Actuation System for the Attitude Control Subsystem Proving Ground

Samuel C. Johnson

Follow this and additional works at: https://scholar.afit.edu/etd

Part of the Aerospace Engineering Commons

DESIGN OF A CONTROL MOMENT GYROSCOPE ATTITUDE ACTUATION SYSTEM FOR THE ATTITUDE CONTROL SUBSYSTEM PROVING GROUND

THESIS

Samuel C. Johnson, 2Lt, USAF

AFIT-ENY-13-M-19

DEPARTMENT OF THE AIR FORCE
AIR UNIVERSITY

AIR FORCE INSTITUTE OF TECHNOLOGY

Wright-Patterson Air Force Base, Ohio

The views expressed in this thesis are those of the author and do not reflect the official policy or position of the United States Air Force, the Department of Defense, or the United States Government. This material is declared the work of the U.S. Government and is not subject to copyright protection in the United States.

AFIT-ENY-13-M-19

DESIGN OF A CONTROL MOMENT GYROSCOPE ATTITUDE ACTUATION SYSTEM FOR THE ATTITUDE CONTROL SUBSYSTEM PROVING GROUND

THESIS

Presented to the Faculty

Department of Aeronautics and Astronautics

Graduate School of Engineering and Management

Air Force Institute of Technology

Air University

Air Education and Training Command

In Partial Fulfillment of the Requirements for the

Degree of Master of Science in Aeronautical Engineering

Samuel C. Johnson, BS

2Lt, USAF

March 2013

AFIT-ENY-13-M-19

DESIGN OF A CONTROL MOMENT GYROSCOPE ATTITUDE ACTUATION SYSTEM FOR THE ATTITUDE CONTROL SUBSYSTEM PROVING GROUND

Samuel C. Johnson, BS

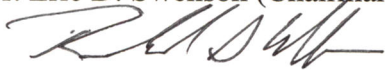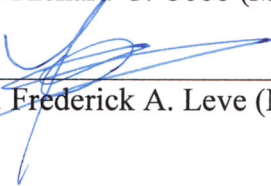2nd Lieutenant, USAF

Approved:

_____
Dr. Eric D. Swenson (Chairman)

_____
Dr. Richard G. Cobb (Member)

_____
Dr. Frederick A. Leve (Member)

_____
12 March 2013
Date

_____
12 MARCH 2013
Date

_____
03/07/2013
Date

Abstract

All spacecraft represent a considerable investment of both time and money. To ensure mission success, testing and validation of all vital systems is crucial to the design process. The attitude control subsystem (ACS) is typically tested thoroughly, to include both hardware and control algorithms. Computer simulations offer a simple and relatively cheap method of predicting the performance of the ACS; however, computer simulations cannot provide the assurances necessary to qualify an ACS hardware configuration or control algorithm spaceworthy. For this reason, physical spacecraft simulators must be used to validate ACS dynamics. Previous research showed there is room for significant improvement to the design methodology of lab-rated control moment gyroscopes (CMGs), which can be used as attitude control devices. An improved design methodology was created to streamline the design process and develop best practices. To evaluate the design methodology, a CMG ACS was designed for the Attitude Control Subsystem Proving Ground (ACSPG), and a prototype was tested.

Acknowledgements

Table of Contents

vi

List of Figures

List of Tables

List of Abbreviations

DESIGN OF A CONTROL MOMENT GYROSCOPE ATTITUDE ACTUATION SYSTEM FOR THE ATTITUDE CONTROL SUBSYSTEM PROVING GROUND

I. Introduction

1.1 Background

Attitude control is the process by which an object manipulates its orientation relative to other objects or an inertial reference frame in order to achieve a desired orientation, angular rate, or angular acceleration. The attitude control subsystem (ACS) is an especially important subsystem in a satellite (also referred to as spacecraft or vehicle), where a satellite's mission will directly determine its attitude control requirements. As an example, an imaging satellite must orient itself relative to its targets, changing orientation each time it collects a new image.

Most modern satellites utilize an active ACS, which monitors the vehicle's orientation, compares the current orientation to the desired orientation, and takes corrective action. There are two main methods of active attitude control: external torque and momentum exchange. The first method uses some form of external torque, most commonly thrusters. This torque is considered external, because there is a net change to the angular momentum of the spacecraft. The drawback to using thrusters is that they require fuel, which is perishable. Magnetorquers are another common form of producing external torque for attitude control; however, in comparison to thrusters, magnetorquers produce very little torque and consume a relatively high amount of electrical power. Other, less common methods of producing an external torque on the spacecraft to achieve attitude control include gravity gradient, solar radiation pressure, and air drag; however, these methods offer less precise control[2].

The second method of active attitude control is achieved using momentum exchange devices such as reaction wheels or control moment gyroscope (CMGs). Reaction wheels and CMG arrays can provide very precise control and do not consume fuel, making

1

them the preferred means of attitude control on most modern spacecraft. For large or particularly agile satellites, the preferred ACS is a CMG array, due to its high torque-to-weight and torque-to-power ratios. A CMG produces torque in a process known as torque amplification. Torque amplification is created by changing the gimbal orientation of a constantly spinning flywheel (also referred to as a rotor). Because the flywheel spin rate is constant, it requires little power to maintain its angular momentum. A motor which changes the flywheel's orientation can have relatively low torque capability, as it must overcome only the torque required to control the gimbal and the induced gyroscopic torque. The output torque of a CMG is a product of the flywheel's angular momentum h_0 and the gimbal rate ω_g. The output torque is much greater than the torque required to turn the gimbal; hence, torque amplification.

The drawback of CMG arrays concerns the complex control algorithms needed to control them. Attitude control using a CMG array is prone to geometric singularities. Singularities are commonly avoided by limiting a vehicle's performance via limitation of the CMG's gimbal angles and rates away from situations where singularities. Improved algorithms to control CMGs will better exploit their performance while keeping their hardware specifications fixed, or reduce their size, weight, power, and cost when their performance is fixed. An improvement in ACS performance, an increase in the available computing power onboard satellites, and the increase in the desire for agile satellites has increased recent interest in CMGs, with a significant focus on CMG steering algorithm development. A steering algorithm commands the rotation of the CMG gimbals to generate the desired control torques. The final phase of steering algorithm development is hardware-in-the-loop testing. The high cost and risk of testing an untested algorithm on a currently operational satellite generally precludes operational testing of steering algorithms on orbit. Satellite simulators, such as AFIT's SimSat, shown in Figure 1.1, or the Attitude Control Subsystem Proving Ground (ACSPG) operated by Air Force Research Laboratory (AFRL) Space Vehicles Directorate, as shown in Figure 1.2 offer a way to develop and test CMG ACS steering algorithms in a laboratory environment at a fraction of the cost and risk.
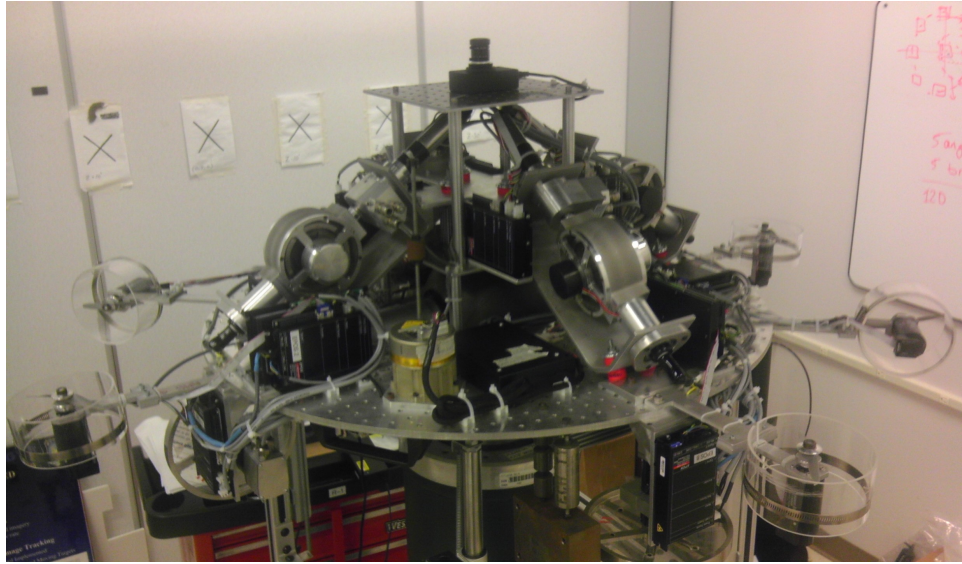
Figure 1.1:   SimSat

Figure 1.2:   The Attitude Control Subsystem Proving Ground

3

1.2 Problem Statement

It is the author's contention that there is room for significant improvement to the design methodology of lab-rated CMGs, which can be used as attitude control devices; therefore, an improved design methodology was created to streamline the design process and develop and/or document best practices. This design methodology was created as part of an effort to design the CMG ACS for the ACSPG. The ACSPG is a large satellite simulator developed and operated by AFRL that is balanced on a spherical air-bearing, and shown in Figure 1.2.

The first step in this process is to determine the sponsor's requirements. AFRL Space Vehicles Directorate tasked AFIT to design a CMG ACS to meet the following requirements:

- Max angular velocity of the ACSPG with a payload and under control of the CMG ACS must be not less than $10°/s$.

- Max angular acceleration of the ACSPG with a payload and under control of the CMG ACS must be not less than $10°/s^2$.

- The inclination angle of the gimbal on the CMGs will be a fixed $45°$.

- The CMG array should be configured such that a 4-CMG pyramid array, 4-CMG box array, and 6-CMG rooftop array can be mounted on the underside of the ACSPG.

- The CMG subsystem should be designed to have minimal acoustic noise and vibration.

- The CMG subsystem must have a minimum lifetime of 15 years, with minimal to no maintenance requirements.

1.3 Research Objectives

The primary objective of this research effort is to develop a methodology for the design, development, and testing of CMG ACSs, and to use this methodology to design a CMG ACS for the ACSPG that would meet the requirements in Section 1.2. The

4

secondary objectives were to develop and test a prototype CMG. The end goal of this research is to provide AFIT and AFRL with an improved method of designing CMGs and ACSs and provide a design for the CMG ACS of the ACSPG.

1.4   Preview

Chapter II consists of a review of topics related to this research, including an overview of relevant literature and background information about satellite simulators, rigid body dynamics, spacecraft control and CMGs and their components. Chapter III covers the design process that was developed for this research effort and how it was applied to the design and testing of the CMG ACS for the ACSPG. Chapter IV provides the results and analysis of simulation and testing detailed in Chapter III. Finally, Chapter V outlines the conclusions drawn from this research and provides recommendations for future work.

5

II. Background

2.1 Satellite Simulators

All spacecraft represent a considerable investment of both time and money. To ensure return on investment, testing and validation is crucial to the design process. Most current spacecraft use space-proven or at least well-understood subsystems. If a new or unique capability is introduced on the spacecraft, it is typically thoroughly tested before it is flown. The attitude control subsystem (ACS) is no different, to include testing both novel hardware and control algorithm. Computer simulations offer a simple and relatively cheap method of predicting the performance of the ACS; however, computer simulations cannot provide the assurances necessary to qualify an ACS hardware configuration or control algorithm spaceworthy. In other words, simulations can only model known behaviors and known uncertainties, whereas unknown uncertainties impact real systems in undesirable ways.[3]

Experiments with hardware-in-the-loop systems partially address the problem of testing a system in the presence of unknown uncertainties. High fidelity tests of hardware-in-the-loop systems should closely model the important aspects of the environment being simulated. Some relevant aspects of the space environment impacting a satellite include micro-gravity, vacuum, large temperature changes, micro-torque, and radiation, to name a few.[4] Many of these environmental factors can be simulated on Earth; however, it is prohibitively difficult to simulate all aspects of the space environment in a test environment without leaving Earth's atmosphere. Therefore, it is necessary to determine the most important aspect of the space environment to the system being tested, and simulate that aspect. For the purpose of testing attitude control, matching the micro-torque environment is the most vital, as the ACS controls the attitude of the spacecraft by applying torque to the vehicle.[5, 6]

2.1.1 Micro-Gravity Experiments.
Creating a micro-gravity environment will inherently create a micro-torque environment. Currently, there are three main methods employed to create a micro-gravity environment without going to space. The first and most commonly used method is neutral buoyancy. The primary use of neutral buoyancy is to simulate the micro-gravity environment for the purpose of astronaut training, as

6

is conducted at the Sonny Carter Training Facility at Johnson Space Center.[7] While neutral buoyancy does provide adequate micro-gravity simulation for many uses, neutral buoyancy does not provide a good fit for the micro-torque desired for attitude control testing. The main drawback to using a neutral buoyancy environment for ACS testing is that the vehicle is subjected to the viscosity of the fluid in which it is submersed. Although the vehicle is in a micro-torque environment when stationary, any type of rate will induce a torque on the vehicle, and the micro-torque environment is lost.

The second way to create a micro-gravity environment on Earth is to conduct tests using a drop tower. Drop tower testing consists of dropping an experiment from a tower into a net below. During free fall, the experiment experiences the micro-gravity environment for a brief period. The only potential force or torque acting on the experiment is air drag, which can be reduced if the drop tower is partially evacuated. Unfortunately, drop tower testing is not without its limitations: experiments can only experience a few seconds of micro-gravity, and upon test completion, the testing apparatus is subjected to rapid deceleration. For example, NASA Glenn's Zero Gravity Facility provides only 5.18 seconds of drop time, and test hardware are subject to a deceleration of approximately 65-g's. Because of the time constraints and durability requirements of drop tower testing, drop tower testing is not a feasible means of testing an ACS either.[8]

The third commonly used method of creating a micro-gravity environment without leaving Earth is by flying an aircraft on a zero-g trajectory. NASA's Reduced Gravity Research Program, commonly known as the "Vomit Comet", exemplifies this type of testing. The aircraft provides the micro-gravity environment by flying in alternating parabolic trajectories from approximately 24,000 feet to 34,000 feet in altitude. At the peak of the maneuver, the aircraft and everything in it experiences approximately 25 seconds of micro-gravity. Because the air inside the cabin is traveling with the aircraft, the effect of air drag on most experiments is minimal, especially when compared to drop tower testing. After the micro-gravity maneuver, the aircraft pulls out of its dive at approximates 2-g's and climbs to begin a new test. While micro-gravity testing does address the main issues of neutral buoyancy and drop tower testing, the experimental

7

time constraint and high recurring cost of aircraft operations limit its usefulness and applicability to ACS testing.[9]

Another option for ACS testing is creating a micro-torque environment while accepting the effect of gravity. For ACS testing, the air-bearing is one way to provide the micro-torque environment desired for an indefinite amount of time. An air-bearing is a mechanical device that provides support between two surfaces while minimizing friction between the surfaces. Air-bearings provide the micro-torque environment by continuously supplying compressed air between the two surfaces. Separating the surfaces with a thin layer of air, which is a low-viscosity fluid, provides a near frictionless environment between the two surfaces. Although air-bearings require continuous flow of pressurized air, a few liters per minute at 6 atmospheres of pressure, they can support several thousand kilograms. Prolonged testing ability in an easy-to-achieve micro-torque environment have made air-bearings the preferred testing apparatus for the ground based development and testing of ACSs.[6]

2.1.2 Planar Air-Bearing. A planar air-bearing is an apparatus with generally a large, flat, smooth surface, across which the test subject is allowed to glide. One example of a simplified version of a planar air-bearing is an air hockey table. Planar air-bearings provide three unconstrained degrees of freedom: one rotational and two translational. For the air hockey example, the puck is allowed to spin and move freely in the x and y directions. Contrary to an air hockey table, most planar air-bearings used in laboratories provide air via the test apparatus rather than the bearing surface. Planar air-bearings are commonly used for testing proximity flight operations, deployment mechanism, and robotic actuators; however, they are not typically used for attitude control experiments, as the primary desire for ACS is three degrees of freedom for rotation. Because planar air-bearings can provide only one degree of freedom in rotation, they were not examined in this research effort.

2.1.3 Spherical Air-Bearings. Spherical air-bearings provide the desired three rotational degrees of freedom by floating a ball on top of a socket joint with the same radius of curvature using compressed air. Because air is a low viscosity fluid, the torque

exerted on the ball and socket is minimal, and the desired micro-torque environment is achieved if gravitational balance can be achieved. In addition to providing three rotational degrees of freedom, the spherical air-bearing fixes all translational motion. For the purpose of ACS testing, this is desirable, as adding extra degrees of freedom would only complicate an already challenging problem. Although the spherical air-bearing provides three rotational degrees of freedom, at least one degree of freedom will almost always be restricted due to the physical geometry of the pedestal and vehicle, as indicated in Figure 2.1. All satellite simulators using spherical air-bearings generally fall into one of three basic designs: dumbbell, tabletop, and umbrella.[6]
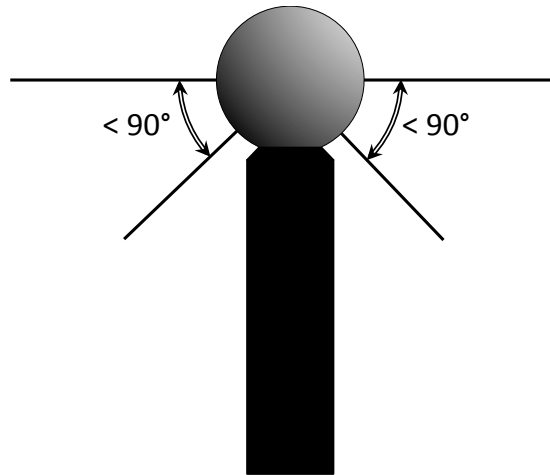
Figure 2.1:   Spherical Air-Bearing Constraints

The dumbbell design, seen in Figure 2.2, places either half of the satellite on each end, mounted on a sphere in the center. The dumbbell provides a unique advantage in that there is unrestricted movement about two axes, while maintaining the center of mass at the center of rotation. Misalignment between the center of mass and center of rotation will result in gravity providing an undesired torque on the vehicle, as shown in Figure 2.4. AFIT's first satellite simulator, SimSat I, as seen in Figure 2.3, was of this configuration, and afforded several years of sound research. The major drawback of this design is the large masses bend the center barbell, and the satellite simulator takes on a preferred orientation.

www.manaraa.com
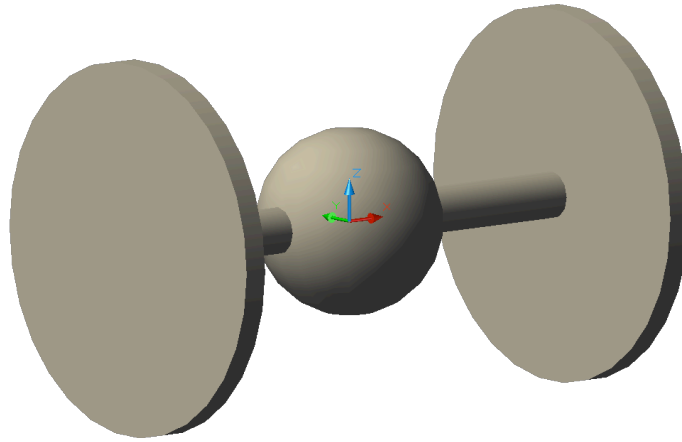
Figure 2.2:   Dumbbell Satellite Simulator
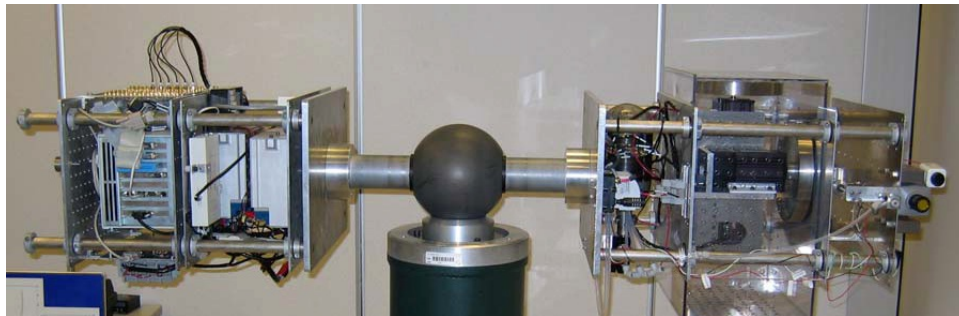
Figure 2.3:   SimSat I

The tabletop design, seen in Figure 2.5, places satellite simulator on the top half of the ball of the air-bearing, and in some cases, around the outer edge of the lower half of the tabletop. As with the dumbbell configuration, the tabletop configuration allows for a coincident center of mass and center of rotation; however, unlike the dumbbell configuration, the tabletop configuration only has one unrestricted axis of rotation. SimSat II, shown in Figure 2.6, AFIT's second generation satellite simulator, and the ACSPG, shown in Figure 1.2, are of the tabletop configuration. Although the tabletop's design restricts movement about two axes, the design is more compact, resulting in smaller values for the moments of inertia than for a similar sized dumbbell configuration, and making the tabletop design well suited for testing ACS for more highly maneuverable satellites.

10
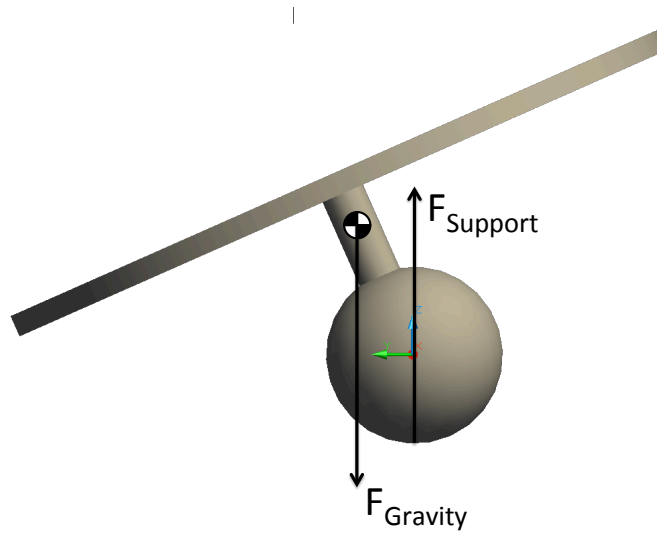
Figure 2.4:   Center of Mass - Center of Rotation Misalignment
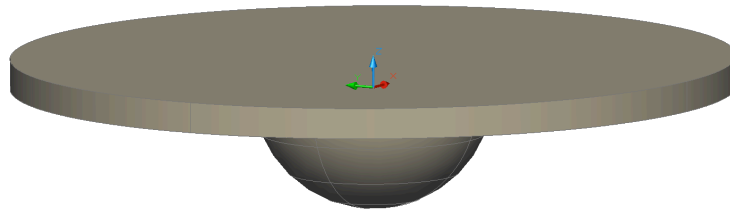
Figure 2.5:   Tabletop Satellite Simulator

Extending the tabletop above the sphere so that there is more freedom to pitch and roll results in the umbrella design, shown in Figure 2.7. In most cases, the umbrella design employs an umbrella shaped structure to support the experiment hardware, although a flat plate placed above the sphere also fits within this classification. Because the mass of the vehicle is offset from the sphere, this design can be difficult to balance. Balance is usually achieved using dense counterweights, as well as careful design of the umbrella structure such that the center of mass is close to the center of rotation. Although more of the sphere is available and the rotation restriction is less severe in the umbrella configuration when compared to the tabletop configuration, it shares the same restrictions as the tabletop configuration in that rotation is restricted about two of the axes.
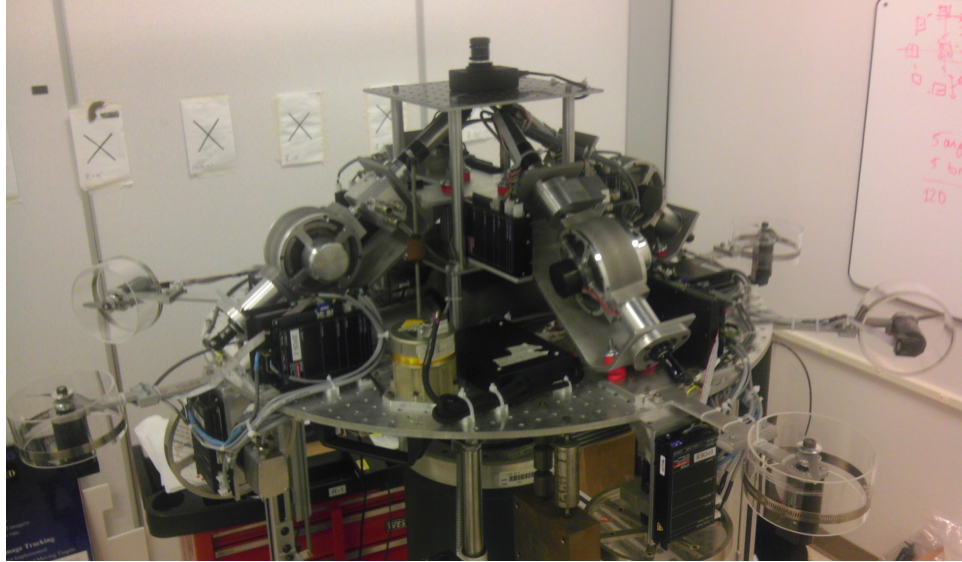
Figure 2.6:   SimSat II
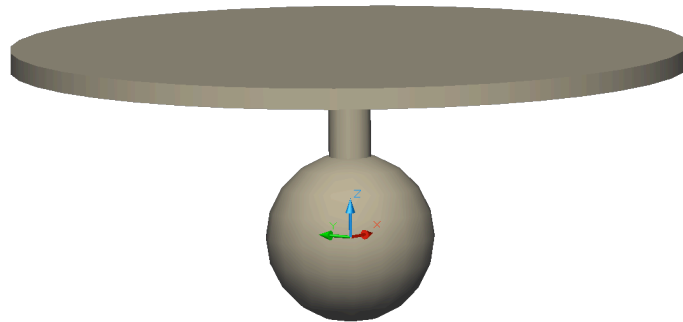
Figure 2.7:   Umbrella Satellite Simulator

2.2   The Attitude Control Subsystem Proving Ground

The Attitude Control Subsystem Proving Ground (ACSPG), shown in Figure 2.8 is AFRL's satellite simulator hardware testbed. It is an umbrella configuration, because the tabletop begins above the ball and extends around. Its primary purpose is to be a hardware testbed for novel control algorithms such as Hybrid Steering Logic (HSL). The ACSPG will also be used as a hardware testbed for spacecraft attitude and rate estimation techniques, including attitude estimation from non-ideal, streaked star camera images. Figure 2.9 shows a CAD version of the ACSPG for the sake of clarity. An

adjustable tilt limiter is attached to the undercarriage, as shown in Figure 2.9. When operational, the tilt limiter ring will be lined with foam to mitigate severe system shock caused by pedestal strikes. The tilt limiter guarantees that the tilt of the ACSPG is never greater than a nominal angle, currently designed to be 30°, although this value is adjustable. Figure 2.10 shows a CAD model of the ACSPG with the current design of the CMG ACS on the undercarriage of the ACSPG.
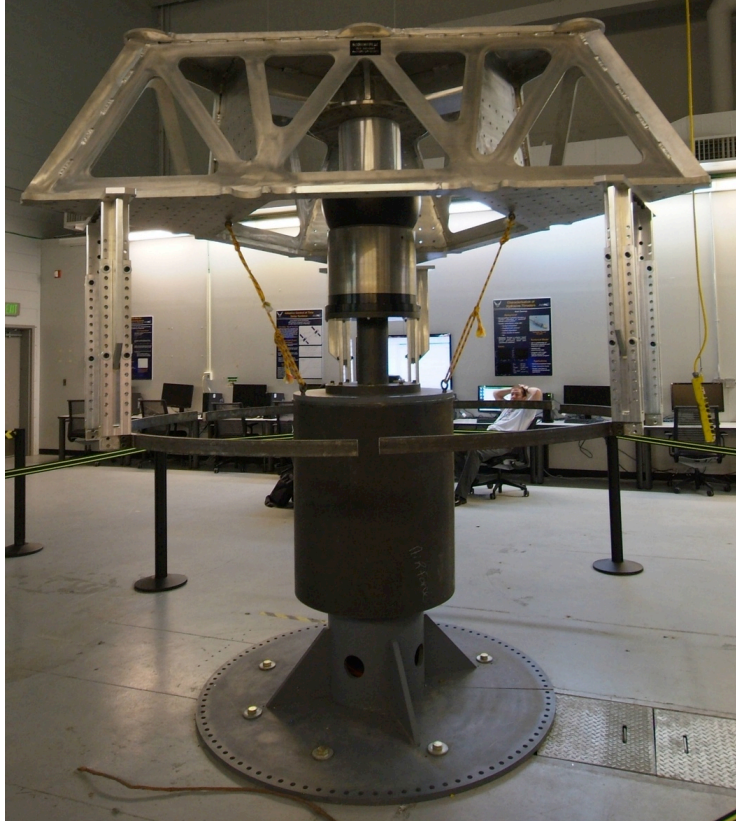
Figure 2.8:   AFRL's ACSPG

Using CAD software, the ACSPG's principal mass moment of inertia (MOI) values were estimated. Table 2.1 lists the mass properties of the ACSPG.

2.3   AFIT Satellite Simulators

Since 1999, AFIT has used satellite simulators to support AFIT's spacecraft dynamics courses, as well as research and development of spacecraft hardware, software, and attitude control steering laws. Table 2.2 lists the work conducted with SimSat. As

13
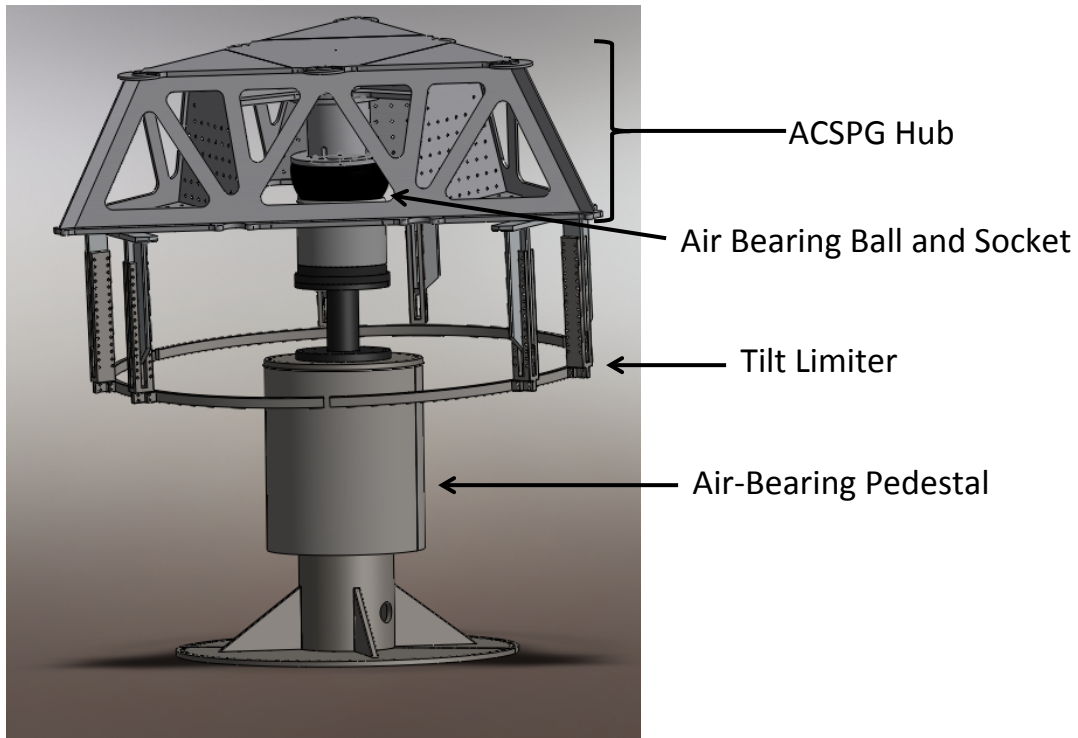
Figure 2.9:   CAD model of AFRL's ACSPG
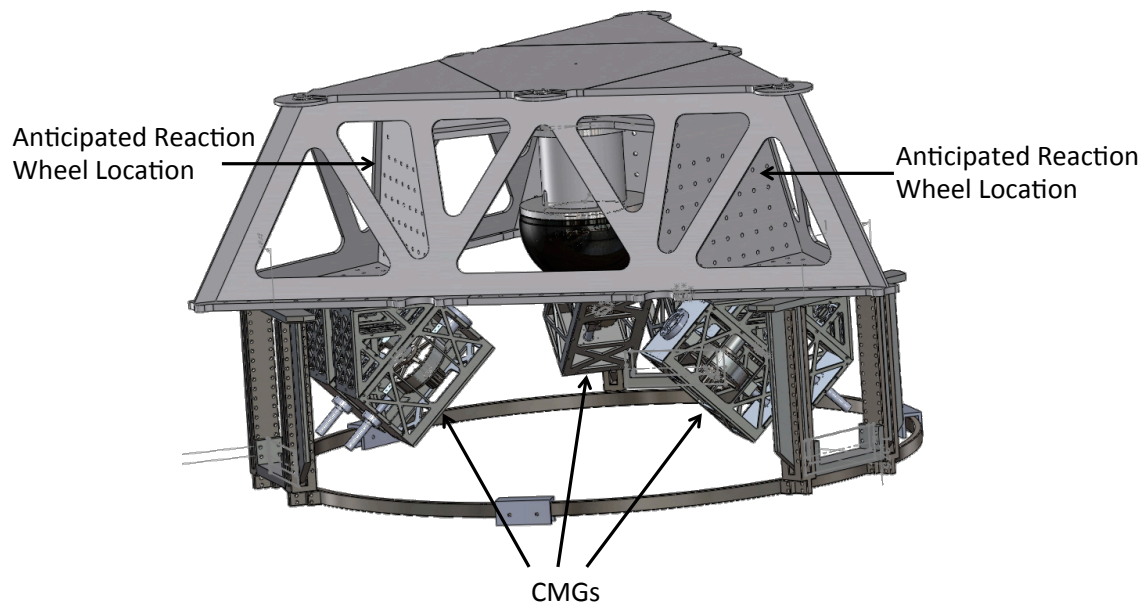
Figure 2.10:   CAD model of AFRL's ACSPG with CMG ACS and anticipated reaction wheel locations

Table 2.1:   AFRL's ACSPG Estimated Mass Properties

Configuration	Mass	I_{xx}	I_{yy}	I_{zz}
Hub Only	575 kg	164 kg-m^2	164kg-m^2	237 kg-m^2
Hub and Tilt Limiter	771 kg	537 kg-m^2	537 kg-m^2	519 kg-m^2
Hub and Tilt Limiter and CMGs	1005 kg	665 kg-m^2	634 kg-m^2	686 kg-m^2

the capstone element of their master's degree at AFIT, Colebank, Jones, Nagy, Pollak, and Mannebach designed SimSat I, the first generation satellite simulator used at AFIT.[10] SimSat I, shown in Figure 2.3 was a dumbbell style satellite simulator with reaction wheels. Improved reaction wheels and cold gas thrusters then were added by French to upgrade and update the design in 2003.[11] Through 2007, SimSat I supported research efforts including space situation awareness, autonomous tracking, and fuel estimation.[12, 13, 11, 14, 15, 16, 17] SimSat I also supported AFIT's spacecraft dynamics courses by providing hands-on demonstrations to students studying attitude dynamics and control.

Although SimSat I adequately achieved its mission, by 2007 it was time for an upgrade to a new system. The result was SimSat II, which is AFIT's current satellite simulator, shown in Figure 2.6. Roach *et al.*[18] designed and built the systems that would make up the basis of SimSat II, a satellite simulator of tabletop configuration with up-to-date electronics, a fan/thruster subsystem, and provisions for further expansion. For the remainder of the document, SimSat II will be referred simply as SimSat. In 2010, Snider upgraded SimSat by installing a set of three reaction wheels. In 2011, McChesney further upgraded the system, adding a single gimbal CMG array (4-CMG pyramid configuration) and exchanging the installed reaction wheels for larger reaction wheels to increase the available momentum storage.

A number of other satellite simulators on spherical air-bearings are also currently in use in academia and industry, including ones at the Naval Postgraduate School, Korea Advanced Institute of Science, Georgia Tech, Virginia Tech, the University of Michigan, Utah State University, Stanford, Honeywell, Boeing, and likely many more.[6, 23] For a

15

Table 2.2:   AFIT Satellite Simulator Research

Student(s)	Year	Style	Advisor	Research Topic	Ref
Colebank *et al.*	1999	Dumbbell	Kramer	Satellite Simulator Design and Assembly	[10]
Fulton	2000	Dumbbell	Agnes	Attitude Control and Multimedia Representation	[12]
Dabrowski	2003	Dumbbell	Cobb	Detection of Parasitic Satellite	[13]
French	2003	Dumbbell	Cobb	Control Strategies for Rapid, Large-Angle Maneuvers	[11]
Kimsal	2004	Dumbbell	Cobb	Autonomous Infrared Tracking	[14]
Smith	2005	Dumbbell	Cobb	Attitude Control using Reaction Wheels and Thrusters	[15]
Geitgey	2006	Dumbbell	Cobb	Measuring Remaining Propellant using Measured MOI	[16]
Hines	2007	Dumbbell	Titus	Fuel Estimation Using Dynamic Response	[17]
Roach *et al.*	2008	Tabletop	Black	Satellite Simulator Design and Assembly	[18]
McFarland	2009	Tabletop	Swenson	Optimal Control of Spacecraft Reorientation Maneuvers	[19]
Snider	2010	Tabletop	Swenson	Attitude Control of a Satellite Simulator Using Reaction Wheels	[20]
McChesney	2011	Tabletop	Swenson	Design of Attitude Control Actuators for a Simulated Spacecraft	[3]
Padro	2012	Tabletop	Swenson	Development of a Star Tracker-Based Reference System for Accurate Attitude Determination of a Simulated Spacecraft	[21]
Wright	2012	Tabletop	Swenson	Hardware Testing of Hybrid Steering Logic for Single-Gimbal Control Moment Gyroscopes	[22]

more in-depth history of air-bearing spacecraft simulators, please see "Historical Review of Air-Bearing Spacecraft Simulators," by Schwartz, Peck, and Hall.[6]

2.4   Spacecraft Dynamics

The purpose of any ACS is to orient the vehicle to the desired attitude relative to another object. Examples include orienting weather satellites toward Earth to observe regions of interest, orienting space telescopes toward an interesting section of the star field, or ensuring solar arrays are at the optimal orientation to receive solar power. The ACS typically is able to control the three rotational degrees of freedom of the vehicle relative to external references, such as the Earth, sun, or stars. To develop an ACS, it is first necessary to derive the vehicle's equations of motion, starting with the kinematic relationships between reference frames.

2.4.1   Kinematics.   In order to relate the orientation to other states and controls, it is first necessary to mathematically define the orientation. A way to represent the orientation of spacecraft is with Euler Parameters, also known as quaternions because of their numerical stability.[24] Leonhard Euler's 1776 theorem states:

In three-dimensional space, any displacement of a rigid body such that a point on the rigid body remains fixed, is equivalent to a single rotation about a fixed axis that runs through the fixed point.[25]

16
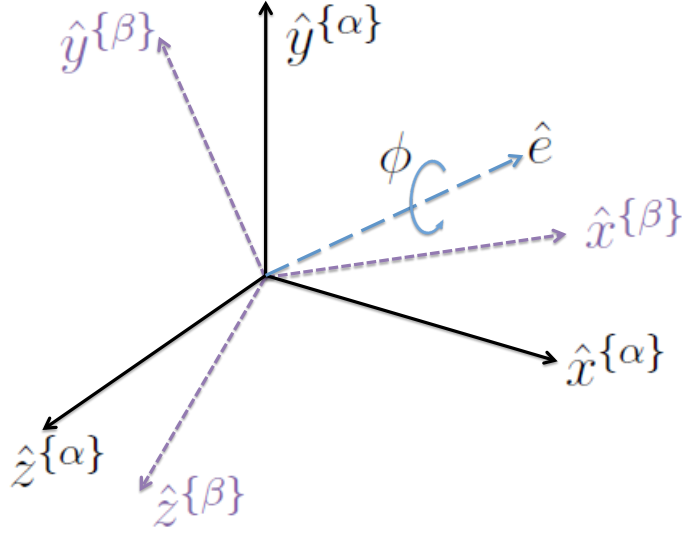
Figure 2.11:   Euler Axis $\hat{e}$ - Euler Angle ϕ Relating Frame $\{\alpha\}$ and Frame $\{\beta\}$

Since reference frames are independent of position, Euler's theorem implies that a unit vector, which defines the rotation axis and an angle, can relate any two reference frames. The rotation axis, denoted by the unit vector $\hat{e}$, is also known as the Euler axis, and the rotation angle about $\hat{e}$ makes to the reference frame is known as the Euler angle ϕ (see Figure 2.11).

However, this method of relating reference frames has a clear singularity; when ϕ is zero the Euler axis is undefined. To avoid computational problems, it is desirable to use a system which has no singularities. Thus, an extension of Euler's theorem is used, commonly known as quaternions. Quaternions are defined as

$$
\begin{bmatrix} q_1 \\ q_2 \\ q_3 \\ q_4 \end{bmatrix} = \begin{bmatrix} e_1\sin\left(\frac{\phi}{2}\right) \\ e_2\sin\left(\frac{\phi}{2}\right) \\ e_3\sin\left(\frac{\phi}{2}\right) \\ \cos\left(\frac{\phi}{2}\right) \end{bmatrix},
\tag{2.1}
$$

where e_1 is the component of $\hat{e}$ along the x-axis, e_2 along the y-axis, and e_3 along the z-axis. The terms q_1, q_2, and q_3 are referred to as the quaternion vector $\bar{q}$. Using the quaternion system, the difference between reference frame orientations can be described with no singularity, regardless of orientation. The difference between two orientations, $\bar{a}$

17

and $\underline{b}$, as defined in the quaternion system is

$$\bar{b}^{\{a\}} = \begin{bmatrix} a_4 & a_3 & -a_2 & -a_1 \\ -a_3 & a_4 & a_1 & -a_2 \\ a_2 & -a_1 & a_4 & -a_3 \\ a_1 & a_2 & a_3 & a_4 \end{bmatrix}^T \begin{bmatrix} b_1 \\ b_2 \\ b_3 \\ b_4 \end{bmatrix}. \tag{2.2}$$

The control algorithm uses Eq. (2.2) to compute the orientation error, which is defined as the difference between the vehicle's desired and current orientation. The orientation error is a quaternion itself, which is nonlinear with respect to ϕ. This nonlinearity is a potential problem for a linear controller. Linearizing the quaternion about $\phi = 0$ gives

$$\begin{bmatrix} e_1 \sin\left(\frac{\phi}{2}\right) \\ e_2 \sin\left(\frac{\phi}{2}\right) \\ e_3 \sin\left(\frac{\phi}{2}\right) \\ \cos\left(\frac{\phi}{2}\right) \end{bmatrix} \approx \begin{bmatrix} e_1 \left(\frac{\phi}{2}\right) \\ e_2 \left(\frac{\phi}{2}\right) \\ e_3 \left(\frac{\phi}{2}\right) \\ 1 \end{bmatrix}. \tag{2.3}$$

Equation (2.3) is valid for a range of approximately -0.6 to 0.6 radians, as shown in Figure 2.12. Because the linear approximation is valid for errors less than ± 0.6 rads, or $\pm 35°$, and orientation error is calculated relative to the current orientation, the linear approximation is sufficient for the tests that will be conducted on the ACSPG. For tests involving changes in orientation larger than $35°$, the researcher should evaluate whether this assumption can be used, or if a higher quality model must be implemented. To align the spacecraft to the desired orientation, the quaternions are manipulated to match the desired orientation. Manipulating the quaternions requires a relationship between the spacecraft's rate of change of orientation $\dot{q}$ and instantaneous angular velocity $\vec{\omega}$. This kinematic relationship is given as

$$\begin{bmatrix} \dot{q}_1 \\ \dot{q}_2 \\ \dot{q}_3 \\ \dot{q}_4 \end{bmatrix} = \frac{1}{2} \begin{bmatrix} q_4 & q_3 & -q_2 \\ -q_3 & q_4 & q_1 \\ q_2 & -q_1 & q_4 \\ -q_1 & -q_2 & -q_3 \end{bmatrix} \begin{bmatrix} \omega_1 \\ \omega_2 \\ \omega_3 \end{bmatrix}. \tag{2.4}$$

18
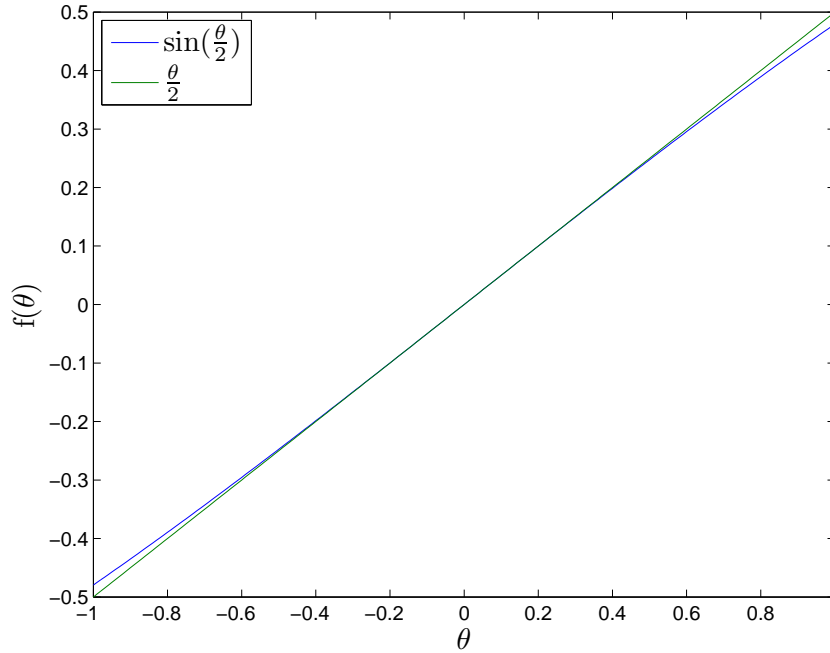
Figure 2.12:   Sin $\left(\frac{\phi}{2}\right)$ v. $\left(\frac{\phi}{2}\right)$

The problem of controlling the vehicle's orientation then becomes a matter of manipulating the vehicle's angular rates by controlling its angular momentum and applied external torques. It is therefore necessary to derive a relationship between angular rates and the satellite's actuators.

2.4.2   Rigid Body Dynamics.   Understanding the concept of angular momentum is key to any discussion of changing angular rates. Angular momentum $\vec{H}$ is defined as

$$\vec{H} = \mathbf{I}\,\vec{\omega}, \tag{2.5}$$

where $\mathbf{I}$ is the object's MOI in matrix form, and $\vec{\omega}$ is the object's angular velocity. An object's MOI is a measure of that object's resistance to a change in angular velocity. An object with larger MOI will require more torque to induce the same change in angular velocity as an object with a smaller MOI. The MOI of an object is determined by the mass distribution of the object relative to the axis of rotation. In Cartesian coordinates,

19

an object's MOI is defined as

$$\mathbf{I} = \begin{bmatrix} I_{xx} & -I_{xy} & -I_{xz} \\ -I_{yx} & I_{yy} & -I_{yz} \\ -I_{zx} & -I_{zy} & I_{zz} \end{bmatrix} \tag{2.6}$$

where I_{xx}, I_{yy}, and I_{zz}, are the scalar moments of inertia, defined as

$$I_{xx} \overset{\text{def}}{=} \int_M \left(y^2 + z^2 \right) dm \tag{2.7a}$$

$$I_{yy} \overset{\text{def}}{=} \int_M \left(x^2 + z^2 \right) dm \tag{2.7b}$$

$$I_{zz} \overset{\text{def}}{=} \int_M \left(x^2 + y^2 \right) dm. \tag{2.7c}$$

The remaining terms, known as products of inertia, are

$$I_{xy} = I_{yx} \overset{\text{def}}{=} \int_M \left(xy \right) dm \tag{2.8a}$$

$$I_{xz} = I_{zx} \overset{\text{def}}{=} \int_M \left(xz \right) dm \tag{2.8b}$$

$$I_{yz} = I_{zy} \overset{\text{def}}{=} \int_M \left(yz \right) dm \tag{2.8c}$$

where x, y, and z are the distance of the differential mass dm from the center of rotation, along an arbitrary orthogonal set. From Eqns. (2.7) and (2.8), it is clear that an object's MOI is dependent on the reference frame and the point of rotation. It is generally useful to choose the origin of the reference frame to be coincident with the center of mass and the directions of the orthogonal set such that the products of inertia reduce to zero, or

$$I_{xy} = I_{xz} = I_{yz} = 0. \tag{2.9}$$

Choosing a coordinate frame in this manner will maximize the moments of inertia. When the products of inertia are zero, the moments of inertia are the principal moments of inertia, and the axes are referred to as principal axes. The principal axes define the body

20

reference frame $\{b\}$. Expressed in the body frame, the MOI of a rigid body is

$$\mathbf{I}_b = \begin{bmatrix} I_1 & 0 & 0 \\ 0 & I_2 & 0 \\ 0 & 0 & I_3 \end{bmatrix} \tag{2.10}$$

and is constant for a rigid body. If an object is symmetric, the axis of symmetry will be a principal axis. Because $\mathbf{I}_b$ is diagonal, $\mathbf{I}_b^{-1}$ is easy to compute, being

$$\mathbf{I}_b^{-1} = \begin{bmatrix} I_1^{-1} & 0 & 0 \\ 0 & I_2^{-1} & 0 \\ 0 & 0 & I_3^{-1} \end{bmatrix}. \tag{2.11}$$

Having defined angular momentum, the next step is understanding how to manipulate angular momentum. Newton's Second Law states

The time rate of change of linear momentum of a body is equal to the sum of the forces acting on that body.[4]

The rotational analog to Newton's Second Law states that the time rate of change of angular momentum about a body's centroid in inertial space is equal to the sum of the moments acting on the body, or

$$\vec{M} = \dot{\vec{H}} = \frac{d}{dt}^{\{i\}} \vec{H} \tag{2.12}$$

where $\dot{\vec{H}}$ represents time rate of change of centroidal angular momentum with respect to an inertial reference frame $\{i\}$, and $\vec{M}$ represents the external moments. As an extension of Newton's Second Law, Eq. (2.12) is only valid if the derivative is taken in an inertial reference frame. In the inertial frame, both the MOI tensor, $\mathbf{I}$, and $\vec{M}$ may change with respect to time as the body rotates, requiring the use of the chain rule during differentiation. Differentiating Eq. (2.5) using the chain rule results yields

$$\frac{d}{dt}^{\{i\}} \vec{H} = \left(\frac{d}{dt}^{\{i\}} \mathbf{I} \right) \vec{\omega} + \mathbf{I} \left(\frac{d}{dt}^{\{i\}} \vec{\omega} \right). \tag{2.13}$$

21

Eq. (2.13) requires that $\mathbf{I}$ be differentiated in the inertial frame. Because the mass distribution changes with respect to the intertia frame as the object changes due to body rotation in the inertial reference frame, differentiating an object's MOI is very undesirable. In the body frame $\{b\}$ the MOI of a rigid body is constant. It is therefore convenient to differentiate in the body frame $\{b\}$ and use the Transport Theorem to account for the relative motion between the body frame $\{b\}$ and the inertial reference frame $\{i\}$.[26] The Transport Theorem is mathematically expressed as

$$\frac{d}{dt}^{\{i\}} \vec{f} = \frac{d}{dt}^{\{r\}} \vec{f} + \vec{\omega}_{ri} \times \vec{f} \tag{2.14}$$

where $\vec{f}$ is an arbitrary vector, $\{r\}$ is an arbitrary reference frame, and $\vec{\omega}_{ri}$ is the angular velocity of the $\{r\}$ frame with respect to the $\{i\}$ frame. The Transport Theorem allows differentiation in either frame, all the while maintaining the relative motion between the two reference frames. Applying the Transport Theorem to Eq. (2.12) and selecting the body frame $\{b\}$ yields

$$\frac{d}{dt}^{\{i\}} \vec{H} = \mathbf{I}_b \frac{d}{dt}^{\{b\}} \vec{\omega}_{bi} + \vec{\omega}_{bi} \times \mathbf{I}_b \, \vec{\omega}_{bi}, \tag{2.15}$$

where $\mathbf{I}_b$ is the MOI expressed in the $\{b\}$ frame about the center of mass and $\vec{\omega}_{bi}$ is the angular rate of both the body and body frame relative to an inertial frame. Eq. (2.15) can now be substituted into Eq. (2.12), yielding

$$\vec{M} = \mathbf{I}_b \frac{d}{dt}^{\{b\}} \vec{\omega}_{bi} + \vec{\omega}_{bi} \times \mathbf{I}_b \, \vec{\omega}_{bi}. \tag{2.16}$$

Eq. (2.16) is commonly referred to as Euler's equation for rotational bodies, written in vector form. Written in Newtonian notation, Eq. (2.16) becomes

$$\vec{M} = \mathbf{I}_b \, \dot{\vec{\omega}}_{bi} + \vec{\omega}_{bi} \times \mathbf{I}_b \, \vec{\omega}_{bi}, \tag{2.17}$$

where all vectors are expressed in the $\{b\}$ frame. This equation allows analysis of spacecraft dynamics while operating primarily in the body frame. Equations in the remainder of Section 2.4 are expressed in the body frame $\{b\}$ except where otherwise noted.

22

2.4.3 Angular Momentum Exchange. So far, it has been assumed that the spacecraft is a single rigid body; however, a spacecraft containing movable actuators cannot be treated as a single rigid body. Therefore, application of the equations developed in Section 2.4.2, require that the spacecraft's angular momentum be broken up as

$$\vec{H}_{net} = \vec{h}_{body} + \vec{h}_{act} \tag{2.18}$$

where $\vec{h}_{act}$ is the angular momentum of the actuator defined at the actuator's center of mass and $\vec{h}_{body}$ represents the angular momentum of the vehicle body. So long as the movement of the movable actuators does not change the vehicle's MOI, Eq. (2.18) can be expressed as

$$\vec{H}_{net} = \mathbf{I}_b \, \vec{\omega}_{bi} + \vec{h}_{act} \tag{2.19}$$

where $\mathbf{I}_b$ is the MOI of the vehicle, including the actuators and any instruments or payload mounted to the body. The actuators are included because they rotate with the body of the vehicle. The term $\vec{h}_{act}$ contains only the dynamic angular momentum of the actuators. The moving components of the actuators should be symmetric to ensure that changing the orientation of the actuator does not change the MOI of the spacecraft. The requirement of symmetry implies an actuator design constraint. Movement of asymmetric actuators will alter the MOI of the spacecraft; in practice, a vehicle's actuators are much smaller than the vehicle, which significantly reduces the requirement of the actuator to not being perfectly symmetric. The main requirement then becomes one of ensuring the center of mass of the moving parts of the control moment gyroscope (CMG) be along the gimbal axis and along the rotor axis for reaction wheels. Substituting Eq. (2.19) into Eq. (2.17) yields

$$\vec{M} = \mathbf{I}_b \, \dot{\vec{\omega}}_{bi} + \dot{\vec{h}}_{act} + \vec{\omega}_{bi} \times \left(\mathbf{I}_b \, \vec{\omega}_{bi} + \vec{h}_{act} \right). \tag{2.20}$$

Assuming the net external moment $\vec{M}$ is negligible, which is a valid assumption for most spacecraft over short time spans, Eq. (2.20) can be recast such that

$$\mathbf{I}_b \, \dot{\vec{\omega}}_{bi} = -\dot{\vec{h}}_{act} - \vec{\omega}_{bi} \times \left(\mathbf{I}_b \, \vec{\omega}_{bi} + \vec{h}_{act} \right). \tag{2.21}$$

23

Equation (2.21) clearly shows that changing $\dot{\vec{h}}_{act}$ in magnitude or direction will change $\dot{\vec{\omega}}_{bi}$. Essentially, angular momentum is exchanged between the spacecraft's actuators and the body of the spacecraft, and total angular momentum is conserved. Reaction wheels and CMGs are aptly described as 'Momentum Exchange Devices.' Because the total angular momentum of the spacecraft and actuators is conserved, the exchange of momentum between actuator and vehicle results in a torque on the vehicle. This exchange can be nonlinear, as shown in the term $-\vec{\omega}_{bi} \times \left(\mathbf{I}_b\, \vec{\omega}_{bi} + \vec{h}_{act} \right)$. Often, these nonlinear terms are ignored because the spacecraft's body rates $\vec{\omega}_{bi}$ are assumed small. Higher fidelity systems may use a nonlinear feedback controller to directly address the nonlinear coupling. The two primary momentum exchange devices used in modern spacecraft are reaction wheels and CMGs. To assist in the buildup of the equations of motion, reaction wheels will be covered first, followed by CMGs.

2.4.4 Reaction Wheels. A reaction wheel is generally made up of a flywheel, electric motor, and supporting electronics. The flywheel has a fixed axis of rotation in the body frame, as the motor is directly mounted to the spacecraft. The angular momentum of a single reaction wheel is

$$\vec{h}_i = I_{rw}\vec{\Psi}_i \tag{2.22}$$

where I_{rw} is the reaction wheel's scalar moment of inertia along its axis of rotation and $\vec{\Psi}_i$ is the angular rate vector of the ith reaction wheel defined in the body frame of the spacecraft. Full three-axis control of a spacecraft requires a minimum of three non-coplanar reaction wheels. For discussion purposes, it is assumed there are only three orthogonal reaction wheels, each aligned with the spacecraft principal axes, x, y, and z. The angular momentum vectors $\vec{\Psi}_1$, $\vec{\Psi}_2$, and $\vec{\Psi}_3$ are aligned with the body x, y, and z axes, respectively. Fixing the position of the reaction wheels in the body frame constrains the direction of $\vec{\Psi}_i$, and the value of I_{rw} is constant as well. The only value that can be changed is the magnitude of the angular rate $\vec{\Psi}_i$. The angular momentum

of the reaction wheel array with three orthogonal reaction wheels is

$$\vec{h}_{rwa} = \begin{bmatrix} I_{rw}\Psi_1 \\ I_{rw}\Psi_2 \\ I_{rw}\Psi_3 \end{bmatrix}. \tag{2.23}$$

Eq. (2.23) can then be substituted into Eqns. (2.19) and (2.20), where $\vec{h}_{rwa}$ in for $\vec{h}_{act}$, giving

$$\vec{H}_{net} = \mathbf{I}_b\vec{\omega}_{bi} + \begin{bmatrix} I_{rw}\Psi_1 \\ I_{rw}\Psi_2 \\ I_{rw}\Psi_3 \end{bmatrix}, \tag{2.24}$$

and

$$\vec{M} = \mathbf{I}_b\dot{\vec{\omega}}_{bi} + \begin{bmatrix} I_{rw}\dot{\Psi}_1 \\ I_{rw}\dot{\Psi}_2 \\ I_{rw}\dot{\Psi}_3 \end{bmatrix} + \vec{\omega}_{bi} \times \left(\mathbf{I}_b\vec{\omega}_{bi} + \begin{bmatrix} I_{rw}\Psi_1 \\ I_{rw}\Psi_2 \\ I_{rw}\Psi_3 \end{bmatrix} \right), \tag{2.25}$$

respectively, where $\dot{\Psi}_i$ is each reaction wheel's acceleration. At this point, we can define

$$M_{rw} = I_{rw}\dot{\Psi}_{rw}, \tag{2.26}$$

where M_{rw} is the internal torque applied by the reaction wheel motor and $\dot{\Psi}_{rw}$ is the reaction wheel acceleration. Therefore, the applied torque to the vehicle by the reaction wheel system is equal and opposite of the torque applied to the reaction wheels. Assuming again that the external moments can be neglected, Eq. (2.25) can be recast as

$$\mathbf{I}_b \, \dot{\vec{\omega}}_{bi} = - \begin{bmatrix} I_{rw}\dot{\Psi}_1 \\ I_{rw}\dot{\Psi}_2 \\ I_{rw}\dot{\Psi}_3 \end{bmatrix} - \vec{\omega}_{bi} \times \left(\mathbf{I}_b \, \vec{\omega}_{bi} + \begin{bmatrix} I_{rw}\Psi_1 \\ I_{rw}\Psi_2 \\ I_{rw}\Psi_3 \end{bmatrix} \right). \tag{2.27}$$

Control is specified by adjusting the angular acceleration of the reaction wheels $\dot{\Psi}_i$ in order to change the vehicle's corresponding angular rotational acceleration $\dot{\omega}_i$. The cross product in Eq. (2.27) results in a nonlinear effect, which is addressed in Section 2.6.2.

25

As previously mentioned, reaction wheels have some significant limitations. A reaction wheel's maximum available torque is directly governed by the torque generated by the motor, as shown in Eq. (2.26). If more torque is desired, the only way to achieve an increase in torque is to use a larger motor, which is most likely both heavier and requires larger electrical power requirements. The power consumed by an electric motor is

$$P = \eta_{motor}\tau\Psi \tag{2.28}$$

where η_{motor} is the motor's efficiency, which is a function of angular rate Ψ, and τ is the applied torque. Eq. (2.28) shows that the power required by a reaction wheel increases with the amount of stored angular momentum.

For discussion purposes, it was assumed that the reaction wheel array contained three reaction wheels in an orthogonal alignment. In practice, most spacecraft use four reaction wheels in a pyramidal arrangement for redundancy, as full, three-axis control is still available even if one reaction wheel fails, which is not uncommon.[27]

2.4.5 *Control Moment Gyroscopes.* The second type of momentum exchange device is the control moment gyroscope (CMG). Typically, a CMG contains a flywheel that is typically spun at a constant rate. The flywheel is mounted onto a gimbaled platform. Because the rotor spin rate is constant, the magnitude of the angular momentum vector is typically fixed. Control is achieved by changing the direction of the angular momentum vector with respect to the spacecraft body by gimballing the flywheel. There are two main categories of CMGs: single gimbal, shown in Figure 2.13, and dual gimbal CMGs. Dual gimbal CMGs work in a manner similar to single gimbal CMGs, but with the ability to rapidly change their inclination angle, also denoted as beta angle β. For single gimbal CMGs, the flywheel is mounted on a gimbal, which, when rotated, changes the direction of the angular momentum vector. Because angular momentum for the entire system is conserved, changing the direction of the actuator angular momentum vector imparts a torque or a change in angular momentum to the spacecraft, and momentum exchange occurs. Since the flywheel can only rotate around its gimbal axis, a single gimbal CMG can only produce torque perpendicular to its gimbal axis. Dual

26
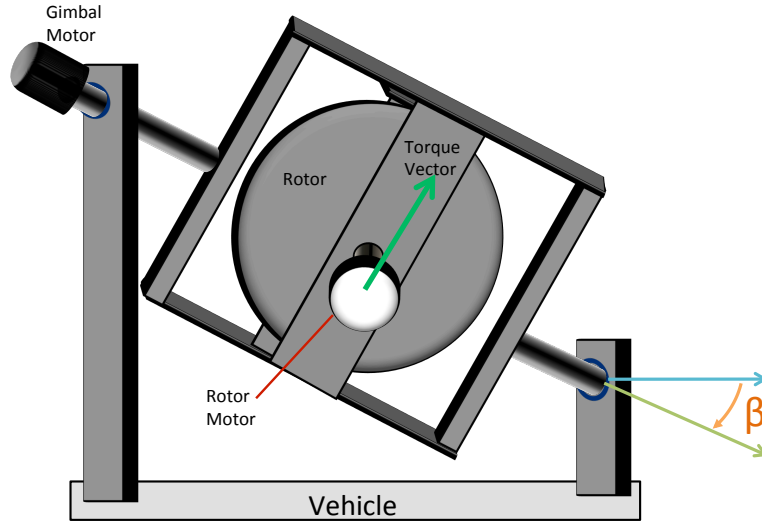
Figure 2.13:   Single Gimbal Control Moment Gyroscope

gimbal CMGs, however, can produce torque along two axes. In either case, the direction of the applied torque is dependent on the current gimbal angle. Since AFRL's ACSPG is designed to test single gimbal CMGs, further analysis will concentrate on their dynamics. Dual gimbal CMGs are noted only for completeness. Additionally, further use of the term CMG in this document specifically refers to single gimbal CMGs.

Figure 2.13 shows that the torque generated by the CMG is orthogonal to both the angular momentum vector and the gimbal axis. Neglecting gimbal inertia, the torque produced by the CMG can be written simply as

$$\vec{\tau} = \dot{\vec{h}} = \vec{\omega}_g \times \vec{h}_0 \tag{2.29}$$

where $\vec{\omega}_g$ is the gimbal rate and $\vec{h}_0$ is the angular momentum of the CMG flywheel. In theory, only a small torque is required to gimbal the flywheel; however, changing the direction of the angular momentum stored in the rotor results in a significantly larger torque on the spacecraft. This concept is referred to as torque amplification.

Where reaction wheels become impractical due to size, weight, or power limitations, CMG arrays are often a practical solution for the problem of attitude control. Large spacecraft, such as the International Space Station, Skylab, and Mir, as well as agile

spacecraft, such as Worldview II, use CMG arrays for this problem. [28, 29] While CMG arrays provide a significantly larger torque envelope than reaction wheel arrays, their dynamics are much more complicated in comparison to reaction wheels, requiring equally complicated control algorithms.

CMGs produce torque by changing the orientation of the gimbal; the implication of this is that the direction of the torque is dependent on the gimbal position, leading to complicated dynamics, especially in comparison to reaction wheels where the torque vector's direction remains constant with respect to the body frame. Three-axis control using CMGs is achieved by arranging multiple CMGs in an array. There are several factors which must be considered when designing a CMG and CMG array, including system dynamics, mass, load carrying capacity, structural stiffness, physical space constraints, cost, redundancy, design complexity, and singularity concerns. Although three-axis control can be achieved using a three-unit CMG array, the need for redundancy results in four-unit CMG arrays being the minimum number of CMGs typically used on spacecraft. The system dynamics are dependent on the orientation of each CMG and how the rotors and gimbals rotate relative to the body frame; therefore, control laws developed for one CMG array design may not apply to other designs. The final CMG array configuration for the ACSPG is a changeable skewed six-unit hybrid rooftop/pyramid design. This design was chosen by the program sponsor. In this hybrid configuration, there is essentially a 4-unit pyramid configuration, where two of the sides of the pyramid are used with 2 additional CMGs to form a 4-unit rooftop. The sponsor expects to only use the 4-unit pyramid configuration or the 4-unit rooftop configuration independently, therefore, these configurations will be discussed separately. While future testing may involve testing all six CMGs in the array, that is beyond the scope of this document.

The system dynamics can now be derived for both the pyramid and rooftop arrays. As done previously, the angular momentum of the spacecraft is separated from the angular momentum of the actuators, per Eqns. (2.19) and (2.20), restated for convenience as

$$\vec{H}_{net} = \mathbf{I}_b \, \vec{\omega}_{bi} + \vec{h}_{act} \tag{2.30}$$

28
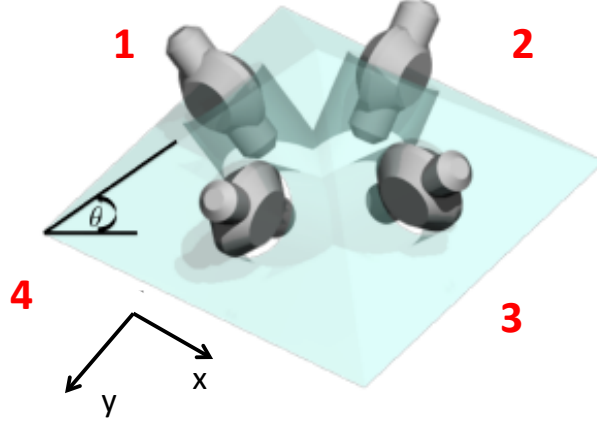
Figure 2.14: Four CMG Pyramid Configuration

and

$$\vec{M} = \mathbf{I}_b \; \dot{\vec{\omega}}_{bi} + \dot{\vec{h}}_{act} + \vec{\omega}_{bi} \times \left(\mathbf{I}_b \; \vec{\omega}_{bi} + \vec{h}_{act} \right) \tag{2.31}$$

where $\vec{h}_{act}$ represents the total angular momentum of the CMG array. Eqns. (2.30) and (2.31) require that $\vec{h}_{act}$ and $\dot{\vec{h}}_{act}$ be expressed in the body frame. First, $\vec{h}_{act}$ is defined with respect to a reference frame defined by the gimbal assembly, then $\vec{h}_{act}$ is passed through three coodinate rotations to the body frame. The rotor and gimbal axes define the first reference frame of the jth CMG, as shown in Figure 2.15. This frame of reference is referred to as the rotor reference frame $\{R_j\}$. Defined in the $\{R_j\}$ frame, the angular momentum of the rotor and gimbal structure is

$$\vec{h}_j^{\{R_j\}} = \begin{bmatrix} I_G \dot{\delta}_j \\ 0 \\ I_R \Omega_j \end{bmatrix} \tag{2.32}$$

where I_G represents the scalar moment of inertia of the gimbal assembly about the gimbal axis, δ_j is the instantaneous gimbal angle, $\dot{\delta}_j$ is the time rate of change of δ_j, I_R is the scalar moment inertia of the rotor about the rotor axis, and Ω_j is the fixed rotational rate of the rotor. The CMGs are designed to be, but are not actually identical; therefore, I_G, I_R, and Ω_j are similar in value for each CMG, respectively. Although these parameters

29

are designed to be identical, they are not truly identical due to material imperfections and imperfect machining tolerances.

Application of Eqns. (2.29)-(2.32) requires that the rotor and gimbal angular momentum $\vec{h}_j$ be expressed in the body frame $\{b\}$. A sequence of rotations then transforms the angular momentum vector $\vec{h}_j$ from each individual rotor frame $\{R_j\}$ to the vehicle's body frame $\{b\}$. The sequence is outlined in Figs. 2.16 through 2.18. In these figures, the side and top plates around the rotor and gimbal are hidden for the sake of clarity. The angular momentum of the jth rotor and gimbal can be expressed in the body frame as

$$\vec{h}_j^{\{b\}} = \mathbf{R}_3(\theta_j)^T \mathbf{R}_2(\beta)^T \mathbf{R}_1(\delta_j)^T \begin{bmatrix} I_G \dot{\delta}_j \\ 0 \\ I_R \Omega \end{bmatrix}. \tag{2.33}$$

The angle θ_j is the mounting angle of each CMG frame with respect to the vehicle about the body frame z-axis $\{b_3\}$, where each CMG has its own value for θ_j (see Figure 2.18). The angle β is defined as the angle from the body XY-plane $\{b_1 - b_2\}$ to the gimbal axis of the CMG, as shown in Figure 2.17. The β angle is the same for all CMGs at -45.00°. The mounting angles θ_j and β were chosen by the program sponsor. Incorporating these angle restrictions, Eq. (2.33) simplifies to

$$\vec{h}_j^{\{b\}} = \mathbf{R}_3(\theta_j)^T \begin{bmatrix} I_G\cos(\beta)\dot{\delta}_j + I_R\Omega_j\sin(\beta)\cos(\delta_j) \\ -I_R\Omega_j\sin(\delta_j) \\ -I_G\sin(\beta)\dot{\delta}_j + I_R\Omega_j\cos(\beta)\cos(\delta_j) \end{bmatrix}. \tag{2.34}$$

The angular momentum of the CMG array is the sum of the six individual CMGs, expressed as

$$\vec{h}_{cmga} = \sum_{j=1}^{6} \left(\mathbf{R}_3(\theta_j)^T \begin{bmatrix} I_G\cos(\beta)\dot{\delta}_j + I_R\Omega_j\sin(\beta)\cos(\delta_j) \\ -I_R\Omega_j\sin(\delta_j) \\ -I_G\sin(\beta)\dot{\delta}_j + I_R\Omega_j\cos(\beta)\cos(\delta_j) \end{bmatrix} \right). \tag{2.35}$$

Because it is expected that only four of the six CMGs will be running during AFRL control algorithm testing, Ω_j is the nominal rotation rate of the rotor for the active
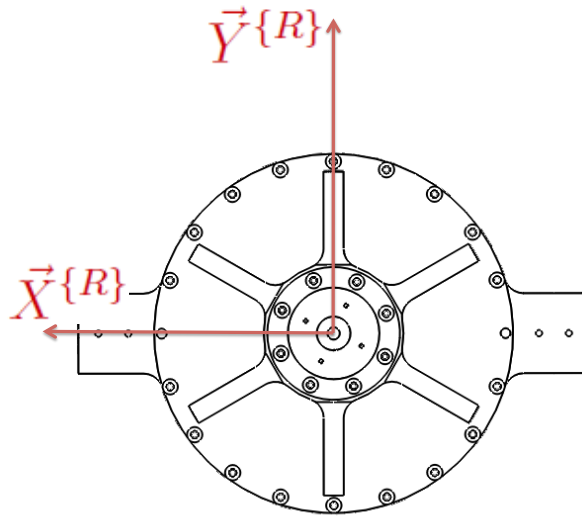
Figure 2.15:   j$^{\text{th}}$ Rotor Frame $\{R_j\}$
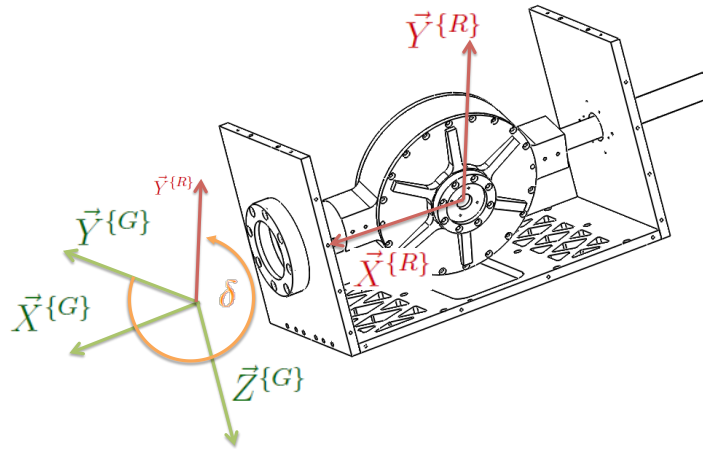
Figure 2.16:   j$^{\text{th}}$ Gimbal Frame $\{G_j\}$

CMGs, or zero for the inactive CMGs. As done previously with the reaction wheel array, $\vec{h}_{cmga}$ is substituted for $\vec{h}_{act}$ in the simplified model Eq. (2.19), resulting in

$$\vec{H}_{net} = \mathbf{I}_b \vec{\omega}_{bi} + \sum_{j=1}^{6} \left(\mathbf{R}_3(\theta_j)^T \begin{bmatrix} I_G \cos(\beta)\dot{\delta}_j + I_R \Omega_j \sin(\beta)\cos(\delta_j) \\ -I_R \Omega_j \sin(\delta_j) \\ -I_G \sin(\beta)\dot{\delta}_j + I_R \Omega_j \cos(\beta)\cos(\delta_j) \end{bmatrix} \right). \tag{2.36}$$

31

$\vec{X}^{\{C\}}$

$\beta = -45°$ $\vec{Z}^{\{G\}}$

$\vec{Y}^{\{b\}}$ $\vec{Y}^{\{C\}}$ $\vec{X}^{\{b\}}$

$\theta_1 = \theta_5 = 0°$

$\vec{X}^{\{b\}}$ $\vec{X}^{\{C\}}$

$\vec{Y}^{\{C\}}$ $\theta_2 = 90°$ $\vec{X}^{\{C\}}$

$\vec{X}^{\{C\}}$ $\theta_3 = \theta_6 = 180°$

$\vec{X}^{\{b\}}$ $\vec{Y}^{\{C\}}$

$\vec{X}^{\{C\}}$ $\vec{X}^{\{b\}}$

$\theta_4 = 270°$ $\vec{X}^{\{b\}}$

$\vec{Y}^{\{b\}}$
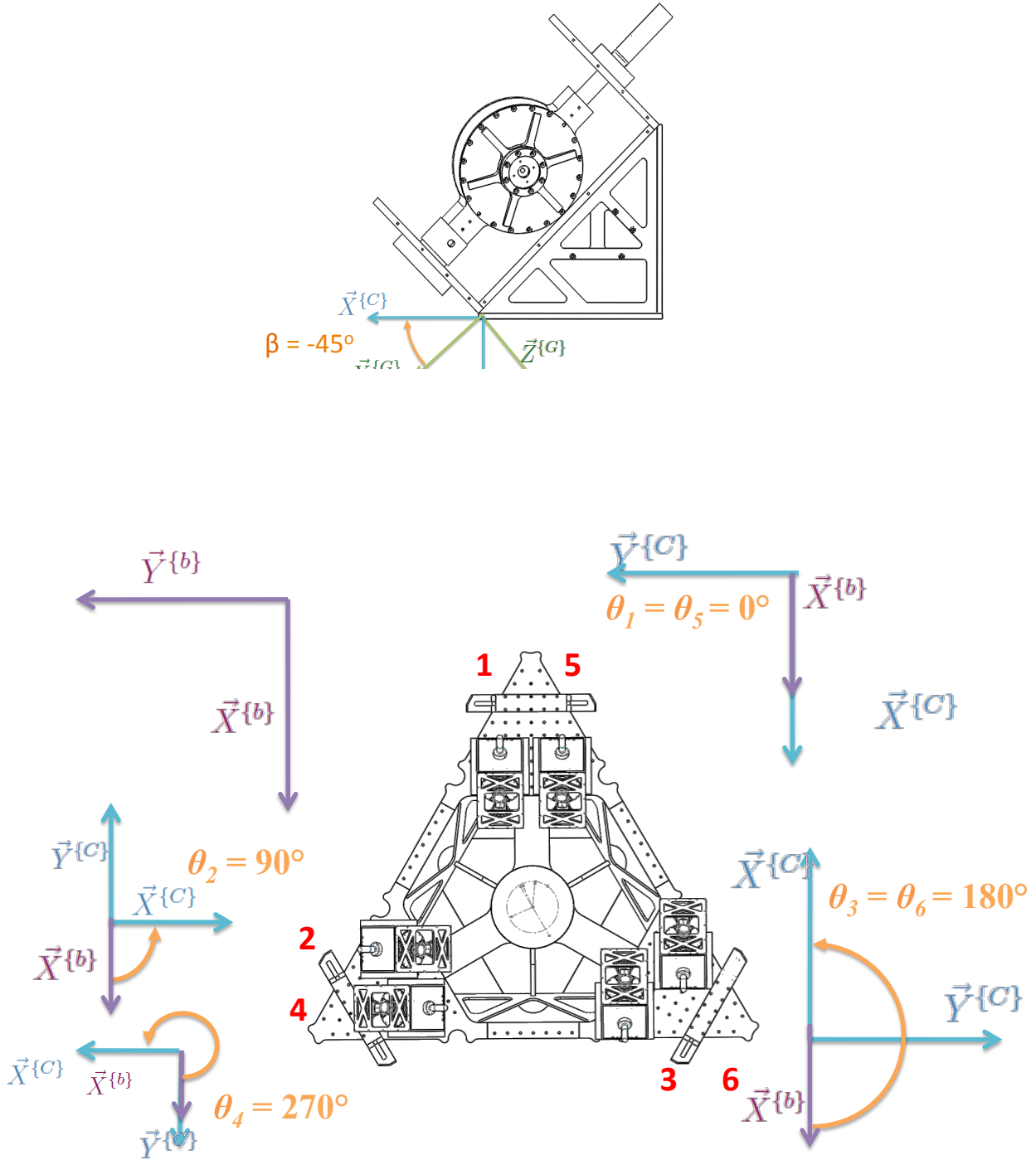
Figure 2.18:   The bottom of the ACSPG and its Body Frame $\{b\}$

Differentiating Eq. (2.19) with respect to an inertial frame results in

$$\dot{\vec{H}}_{net} = \mathbf{I}_b \, \dot{\vec{\omega}}_{bi} + \sum_{j=1}^{6} \left(\mathbf{R}_3(\theta_j)^T \begin{bmatrix} I_G\cos(\beta)\ddot{\delta}_j - I_R\Omega_j\sin(\beta)\sin(\delta_j)\dot{\delta}_j \\ -I_R\Omega_j\cos(\delta_j)\dot{\delta}_j \\ -I_G\sin(\beta)\ddot{\delta}_j - I_R\Omega_j\cos(\beta)\sin(\delta_j)\dot{\delta}_j \end{bmatrix} \right) + \qquad (2.37)$$

$$\vec{\omega}_{bi} \times \mathbf{I}_b \, \vec{\omega}_{bi} + \vec{\omega}_{bi} \times \sum^{6} \left(\mathbf{R}_3(\theta_j)^T \begin{bmatrix} I_G\cos(\beta)\dot{\delta}_j + I_R\Omega_j\sin(\beta)\cos(\delta_j) \\ -I_R\Omega_j\sin(\delta_j) \end{bmatrix} \right)$$

Eq. (2.37) can be simplified if it can be assumed that

$$\dot{\delta}_j \ll \Omega \tag{2.38}$$

$$\ddot{\delta}_j \ll \Omega\dot{\delta}_j. \tag{2.39}$$

Because the typical rotor rate Ω for a CMG is hundreds radians per second (3000+ rpm), while gimbal rates $\dot{\delta}$ and accelerations $\ddot{\delta}$ are maximum a few radians per second and radians per second per second, expected assumptions are valid for CMGs. All CMGs installed on the ACSPG have a nominal rotor rate Ω of 628 rad/sec when operating, while $\dot{\delta}_j$ is restricted to 2.5 rad/sec, validating Eq. (2.38) which further implies that Eq. (2.39) is predominantly true for except when $\dot{\delta}_j$ is zero. Applying these assumptions simplifies Eq. (2.37) to

$$
\begin{aligned}
\dot{\vec{H}}_{net} = \mathbf{I}_b \, \dot{\vec{\omega}}_{bi} + \sum_{j=1}^{6} \left(\mathbf{R}_3(\theta_j)^T \begin{bmatrix} -I_R\Omega_j\sin(\beta)\sin(\delta_j)\dot{\delta}_j \\ -I_R\Omega_j\cos(\delta_j)\dot{\delta}_j \\ -I_R\Omega_j\cos(\beta)\sin(\delta_j)\dot{\delta}_j \end{bmatrix} \right) + \\
\vec{\omega}_{bi} \times \mathbf{I}_b \, \vec{\omega}_{bi} + \vec{\omega}_{bi} \times \sum_{j=1}^{6} \left(\mathbf{R}_3(\theta_j)^T \begin{bmatrix} I_R\Omega_j\sin(\beta)\cos(\delta_j) \\ -I_R\Omega_j\sin(\delta_j) \\ I_R\Omega_j\cos(\beta)\cos(\delta_j) \end{bmatrix} \right).
\end{aligned}
\tag{2.40}
$$

Eq. (2.40) can be further simplified by factoring out like terms, removing the summations, converting to matrix form, and simplifying the array from the hybrid pyramid/rooftop into the 4-unit pyramid and 4-unit rooftop configurations, where CMG numbers 1, 2, 3, and 4 are used in the pyramid configuration, and CMG numbers 1, 2, 5, and 6 are used in the rooftop configuration. The net change in angular momentum for the pyramid configuration $\dot{\vec{H}}_{net_p}$ (subscript p denotes pyramid configuration) is

$$
\dot{\vec{H}}_{net_p} = \mathbf{I}_b \, \dot{\vec{\omega}}_{bi} + I_R\Omega \, \mathbf{A}_p \begin{bmatrix} \dot{\delta}_1 \\ \dot{\delta}_2 \\ \dot{\delta}_3 \\ \dot{\delta}_4 \end{bmatrix} + \vec{\omega}_{bi} \times \mathbf{I}_b \, \vec{\omega}_{bi} + \vec{\omega}_{bi} \times I_R\Omega\bar{h}_{cmga_p}
\tag{2.41}
$$

33

where

$$\mathbf{A}_p = \begin{bmatrix} -\sin(\beta)\cos(\delta_1) & \sin(\delta_2) & \sin(\beta)\cos(\delta_3) & -\sin(\delta_4) \\ \sin(\delta_1) & \sin(\beta)\cos(\delta_2) & -\sin(\delta_3) & -\sin(\beta)\cos(\delta_4) \\ \cos(\beta)\cos(\delta_1) & \cos(\beta)\cos(\delta_2) & \cos(\beta)\cos(\delta_3) & \cos(\beta)\cos(\delta_4) \end{bmatrix} \qquad (2.42)$$

and

$$\bar{h}_{cmga_p} = \begin{bmatrix} -\sin(\beta)\sin(\delta_1) & -\cos(\delta_2) & \sin(\beta)\sin(\delta_3) & \cos(\delta_4) \\ -\cos(\delta_1) & \sin(\beta)\sin(\delta_2) & \cos(\delta_3) & -\sin(\beta)\sin(\delta_4) \\ \cos(\beta)\sin(\delta_1) & \cos(\beta)\sin(\delta_2) & \cos(\beta)\sin(\delta_3) & \cos(\beta)\sin(\delta_4) \end{bmatrix}. \qquad (2.43)$$

The vector $\bar{h}_{cmga}$ is made up of unit vectors denoting the direction of the angular momentum of each CMG, and $I_R\Omega$ is the scalar magnitude of the angular momentum of a single CMG; therefore, the product of the two gives the total angular momentum of the CMG array

$$\vec{H}_{cmga_p} = I_R\Omega \begin{bmatrix} -\sin(\beta)\sin(\delta_1) & -\cos(\delta_2) & \sin(\beta)\sin(\delta_3) & \cos(\delta_4) \\ -\cos(\delta_1) & \sin(\beta)\sin(\delta_2) & +\cos(\delta_3) & -\sin(\beta)\sin(\delta_4) \\ \cos(\beta)\sin(\delta_1) & \cos(\beta)\sin(\delta_2) & \cos(\beta)\sin(\delta_3) & \cos(\beta)\sin(\delta_4) \end{bmatrix}. \qquad (2.44)$$

Eqns. (2.41)-(2.44) are only valid for the system for the 4-unit pyramid configuration. Applied to the 4-unit rooftop configuration, where units 2 and 4 are turned off and 5 and 6 are turned on, Eqns. (2.41)-(2.44) become

$$\dot{\vec{H}}_{net_r} = \mathbf{I}_b\,\dot{\vec{\omega}}_{bi} + I_R\Omega\,\mathbf{A}_r \begin{bmatrix} \dot{\delta}_1 \\ \dot{\delta}_3 \\ \dot{\delta}_5 \\ \dot{\delta}_6 \end{bmatrix} + \vec{\omega}_{bi} \times \mathbf{I}_b\,\vec{\omega}_{bi} + \vec{\omega}_{bi} \times I_R\Omega\bar{h}_{cmga_r} \qquad (2.45)$$

where subscript r stands for rooftop and

$$\mathbf{A}_r = \begin{bmatrix} -\sin(\beta)\cos(\delta_1) & \sin(\beta)\cos(\delta_3) & -\sin(\beta)\cos(\delta_5) & \sin(\beta)\cos(\delta_6) \\ \sin(\delta_1) & -\sin(\delta_3) & \sin(\delta_5) & -\sin(\delta_6) \\ \cos(\beta)\cos(\delta_1) & \cos(\beta)\cos(\delta_3) & \cos(\beta)\cos(\delta_5) & \cos(\beta)\cos(\delta_6) \end{bmatrix} \quad (2.46)$$

and

$$\bar{h}_{cmga_r} = \begin{bmatrix} -\sin(\beta)\sin(\delta_1) & \sin(\beta)\sin(\delta_3) & -\sin(\beta)\sin(\delta_5) & \sin(\beta)\sin(\delta_6) \\ -\cos(\delta_1) & \cos(\delta_3) & -\cos(\delta_5) & \cos(\delta_6) \\ \cos(\beta)\sin(\delta_1) & \cos(\beta)\sin(\delta_3) & \cos(\beta)\sin(\delta_5) & \cos(\beta)\sin(\delta_6) \end{bmatrix} \quad (2.47)$$

$$\vec{H}_{cmga_r} = I_R\Omega \begin{bmatrix} -\sin(\beta)\sin(\delta_1) & \sin(\beta)\sin(\delta_3) & -\sin(\beta)\sin(\delta_5) & \sin(\beta)\sin(\delta_6) \\ -\cos(\delta_1) & \cos(\delta_3) & -\cos(\delta_5) & \cos(\delta_6) \\ \cos(\beta)\sin(\delta_1) & \cos(\beta)\sin(\delta_3) & \cos(\beta)\sin(\delta_5) & \cos(\beta)\sin(\delta_6) \end{bmatrix}.$$
$$(2.48)$$

The matrix $\mathbf{A}$ characterizes the relationship between the change in the angular momentum of the CMG array with respect to the gimbal rates. By inspection of $\mathbf{A}$ and $\vec{H}_{cmga}$, it can be shown that

$$I_R\Omega \ \mathbf{A}(1,1) = \frac{\partial H(1)}{\partial\delta(1)}$$
$$I_R\Omega \ \mathbf{A}(1,2) = \frac{\partial H(2)}{\partial\delta(1)}$$
$$\vdots \quad\quad\quad\quad\quad (2.49)$$
$$I_R\Omega \ \mathbf{A}(3,3) = \frac{\partial H(3)}{\partial\delta(3)}$$
$$I_R\Omega \ \mathbf{A}(3,4) = \frac{\partial H(4)}{\partial\delta(3)}$$

which is the definition of the Jacobian for $\vec{H}_{cmga}$ with respect to $\bar{\delta}$ or

$$\mathbf{J}_H = \mathbf{A} = \frac{\partial\vec{H}_{cmga}}{\partial\bar{\delta}} \quad (2.50)$$

and is a function of the gimbal angles. The relationship formed by the Jacobian $\mathbf{J}_H$ is then used to relate the change in the CMG array angular momentum to the control variables by

$$\dot{\vec{H}}_{cmga} = I_R \Omega \mathbf{J}_H \ \dot{\bar{\delta}} \tag{2.51}$$

where $\dot{\vec{H}}_{cmga}$ is the controller solution and must be solved for $\bar{\delta}$; however, the Jacobian $\mathbf{J}_H$ is not square, which means it is not directly invertible. When applied to the CMG arrays, solutions to Eq. (2.51) are known as steering laws.

2.5   CMG Momentum Envelope and Steering Laws

Before focusing on the development of the steering laws, let us first consider the momentum envelope of the CMG array. The MATLAB program used to generate these momentum envelopes was based on algorithms sourced from Leve.[30] Before examining the full pyramid and rooftop configurations, we will start by considering a single CMG. The momentum envelope of a single CMG is a ring perpendicular to its gimbal axis, as shown in Figure 2.19, where the ring represents the momentum envelope, and the line represents the gimbal axis.
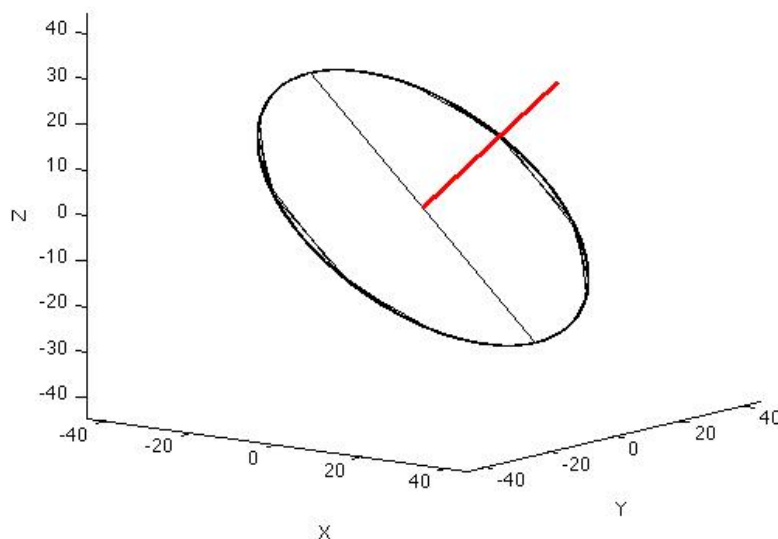
Figure 2.19:   Angular Momentum Envelope for a Single CMG.

Expanding from one to two CMGs, specifically CMG numbers 1 and 3 as shown in Figure 2.14, expands the momentum envelope to a three-dimensional surface, as shown

in Figures 2.20 and 2.21. Adding the momentum vectors from each CMG forms the external singular surface, also known as the saturation surface, as shown in Figure 2.20. Subtracting the momentum vectors from each other forms the internal singular surface, as shown in Figure 2.21. The combined angular momentum of the two CMGs is constrained to these surfaces.
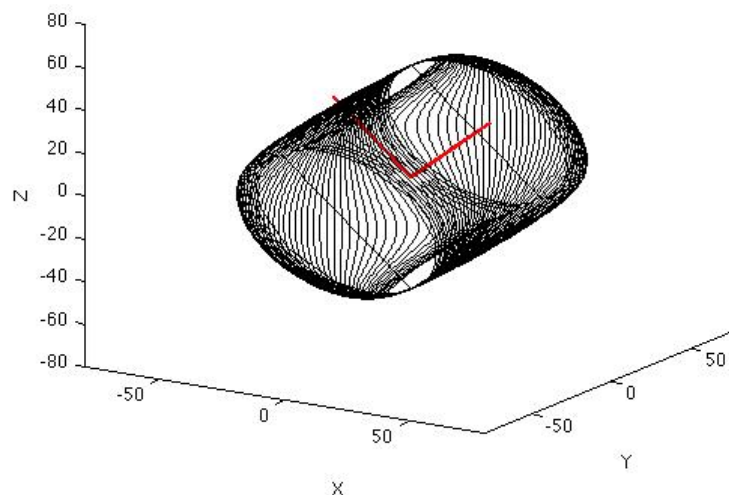
Figure 2.20:   External Singularity Surface for a 2-CMGs Array: CMGs 1 and 3
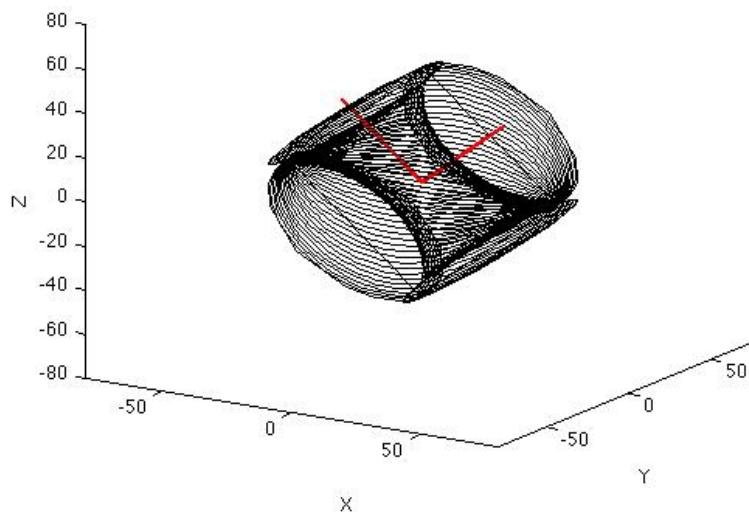
Figure 2.21:   Internal Singularity Surface for a 2-CMG Array: CMGs 1 and 3

37
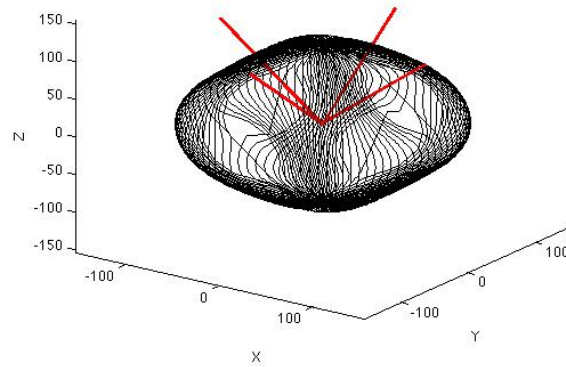
Figure 2.22:   External Singularity Surface for a 4-CMG Array
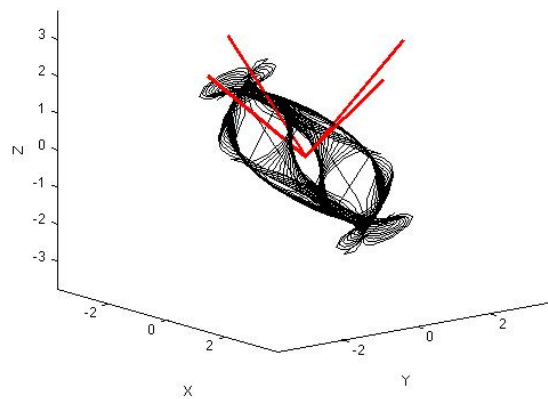
Figure 2.23:   Internal Singularity Surface for a 4-CMG Array

Figure 2.24 shows the achievable momentum envelope for the 4-CMG rooftop configuration. For a 4-unit rooftop CMG, all internal singularities are hyperbolic and passable (i.e., can be avoided by null motion).

Two steering laws were considered for testing on the ACSPG, the Moore-Penrose Pseudoinverse Steering Law (MPPSL) and the Generalized Inverse Steering Law (GISL). The behavior of these steering laws is well understood, and can therefore be used to validate the CMG subsystem performance. Additional verification of the behavior and performance of the CMG array was conducted using the null motion path technique.

38
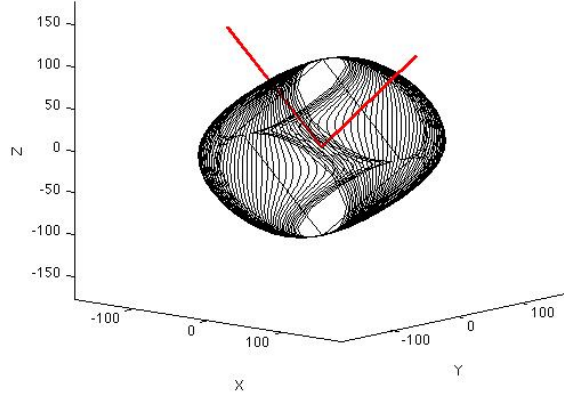
Figure 2.24:   External Singularity Surface for a 4-CMG Rooftop Array

2.5.1   Null Motion.   The Jacobian $\mathbf{J}_H$ has more columns than rows, guaranteeing the existence of a null space, such that

$$\dot{\vec{H}}_{cmga} = \vec{0} = \mathbf{J}_H \dot{\vec{\delta}}_N \tag{2.52}$$

for $\dot{\vec{\delta}}_N \neq 0$. The null space is the result of having more than three actuators controlling a three dimensional problem. Specifying the gimbal rates to be $\dot{\vec{\delta}}_N$ results in no change to the angular momentum of the CMG array, resulting in no net torque on the spacecraft. Ideally, the null space is one-dimensional; however, that is not always the case.[31]

2.5.2   Moore-Penrose Pseudoinverse Steering Law.   The first steering law presented in this research was the Moore-Penrose Pseudoinverse Steering Law (MPPSL) and is also known as the right-inverse. The MPPSL method solves the system

$$\mathbf{A}\bar{x} = \bar{b}, \tag{2.53}$$

where A has more columns than rows, by creating the Moore-Penrose Pseudoinverse matrix

$$\mathbf{A}^+ = \mathbf{A}^T \left(\mathbf{A}\mathbf{A}^T \right)^{-1} \tag{2.54}$$

and using $\mathbf{A}^+$ to solve

$$\bar{x} = \mathbf{A}^T \left(\mathbf{A}\mathbf{A}^T \right)^{-1} \bar{b} = \mathbf{A}^+ \bar{b}. \tag{2.55}$$

39

Applying the Moore-Penrose Pseudoinverse to the control problem presented in Eq. (2.51) gives

$$\dot{\vec{\delta}} = \mathbf{J}_H{}^T \left(\mathbf{J}_H \mathbf{J}_H{}^T \right)^{-1} \dot{\vec{H}}_{cmga} = \mathbf{J}_H{}^+ \dot{\vec{H}}_{cmga} \tag{2.56}$$

where $\dot{\vec{\delta}}$ is the commanded gimbal rates, $\mathbf{J}_H$ is the Jacobian of the CMG array, and $\dot{\vec{H}}_{cmga}$ is the desired rate of change in the angular momentum of the system. While the MPPSL has well-known and relatively simple dynamics, this method does not address internal singularities, and fails any time $\mathbf{J}_H \mathbf{J}_H{}^T$ is singular.

2.5.3 *Generalized Inverse Steering Law.*   The Generalized Inverse Steering Law (GISL) is an alternative method of inverting $\mathbf{J}_H$ in a method that avoids some of the singularity problems that could not be addressed by the MPPSL. Specifically, the GISL couples null motion into the gimbal movements to avoid non-degenerate singularities. While the GISL can avoid some singularities, it cannot avoid degenerate internal singularities, from which there is no escape path using the null motion technique. Generating the GISL is done by first defining a new coordinate system in $\bar{\Upsilon} \in \mathbb{R}^3$ such that

$$\dot{\vec{\delta}} = \mathbf{A}^T \dot{\Upsilon}. \tag{2.57}$$

Substituting Eq. (2.57) into Eq. (2.51) gives

$$\begin{aligned} \dot{\vec{H}}_{cmga} &= \mathbf{J}_H \dot{\vec{\delta}} \\ &= \mathbf{J}_H \mathbf{A}^T \dot{\Upsilon}. \end{aligned} \tag{2.58}$$

Assuming that $\mathbf{J}_H \mathbf{A}^T$ is non-singular, it is then implied that

$$\dot{\Upsilon} = \left(\mathbf{J}_H \mathbf{A}^T \right)^{-1} \dot{\vec{H}}_{cmga}. \tag{2.59}$$

Eq. (2.59) can now be substituted back into Eq. (2.57), providing the GISL as

$$\dot{\vec{\delta}} = \mathbf{A}^T \left(\mathbf{J}_H \mathbf{A}^T \right)^{-1} \dot{\vec{H}}_{cmga}. \tag{2.60}$$

If $\mathbf{J}_H$ is used for $\mathbf{A}$, then the GISL simplifies to the previously derived Moore-Penrose solution; however, it is possible to select a different $\mathbf{A}$ matrix to make the solution more robust. Asghar[32] and Leve[30] both propose that

$$\mathbf{A} = \mathbf{J}_H + \mathbf{D} \tag{2.61}$$

where the column vectors in the matrix $\mathbf{D}$ are orthogonal to the columns in $\mathbf{J}_H$. One option, specifically for the pyramid configuration, is to define $\mathbf{D}$ as

$$\mathbf{D} = I_R \Omega \begin{bmatrix} -\sin(\beta)\sin(\delta_1) & -\cos(\delta_2) & \sin(\beta)\sin(\delta_3) & \cos(\delta_4) \\ -\cos(\delta_1) & \sin(\beta)\sin(\delta_2) & \cos(\delta_3) & -\sin(\beta)\sin(\delta_4) \\ \cos(\beta)\sin(\delta_1) & \cos(\beta)\sin(\delta_2) & \cos(\beta)\sin(\delta_3) & \cos(\beta)\sin(\delta_4) \end{bmatrix} \tag{2.62}$$

which can be substituted into Eq. (2.60), providing the complete GISL as

$$\dot{\vec{\delta}} = (\mathbf{J}_H + \mathbf{D})^T \left(\mathbf{J}_H (\mathbf{J}_H + \mathbf{D})^T \right)^{-1} \dot{\vec{H}}_{cmga}. \tag{2.63}$$

This $\mathbf{D}$ is designed to force null motion behavior into the specified control solution, thereby avoiding or passing through non-degenerate internal singularities; however, it cannot avoid degenerate internal singularities or saturation. Non-degenerate internal singularities will occur any time $\mathbf{J}_H (\mathbf{J}_H + \mathbf{D})^T$ is singular.[32, 30]

2.6 Linearized Proportional-Integral-Derivative Attitude Control

2.6.1 PID Control. The proportional-integral-derivative (PID) controller is a widely used linear control algorithm, chosen for implementation on the ACSPG because of its simple implementation. Properly tuned, a PID controller can provide satisfactory, although not necessarily optimal, control for a range of inputs and disturbances. Furthermore, PID controllers work well in systems with poorly understood or poorly characterized plant dynamics. Because of these properties, more than half of modern industrial control is provided by PID or modified PID controllers.[33]

PID control operates on the error q_E to calculate the corrective action M_C, which is fed into the plant G_P, where the error q_E is defined as the difference between the desired state q_D and the actual state q_A. Figure 2.25 shows the standard block diagram for a PID controller. The PID controller is made up of separate proportional, integral, and derivative contollers. As indicated by its name, the proportional component produces a corrective control proportional to q_E, as dictated by the proportional gain K_P. Increasing K_P increases the output of the control for a given error, resulting in a quicker response, but also resulting in greater overshoot and a longer settling time. Choosing a K_P that is too large for the specific system application can also result in an unstable system.
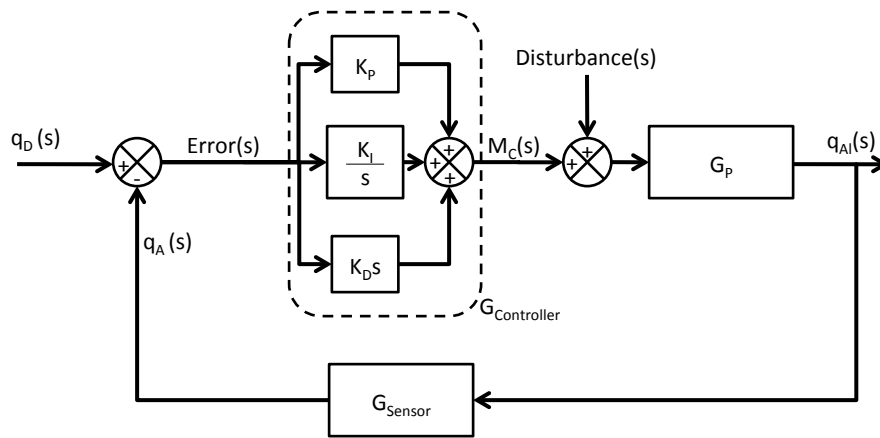
Figure 2.25:   PID Controller

The second component of the PID controller is the integral controller, which produces a response proportional to the error's magnitude and duration of the error as dictated by the integral gain K_I. Combined with the proportional component, the integral component further increases response speed. More importantly, adding integral control to a system eliminates steady-state error. The cost of adding integral control to a system is an increase in both overshoot and settling time, caused by integrator windup. Integrator windup is caused by large changes in error over short time periods, with finite control or limited control due to saturation, as produced when changing the desired state. While the error is being corrected, the integrator accumulates the error, or winds up. The integrator must then unwind, which forces the system past the desired state if the windup is great enough. Integral control poses problems for systems with

42

limited control, as large changes to the desired state can cause control saturation, further delaying system response.

The derivative control component rounds out the PID controller. The derivative component slows the system response by adding damping according to the term K_D, which decreases both the overshoot and settling time of the system. The primary use of derivative control is to reduce the overshoot caused by large values of K_P and K_I. The drawback of derivative control is that numerical differentiation amplifies any noise in the error signal, which is then proportionally increased by K_D. If the amplified noise is too great, the system can be overcome by it and become unstable. It is therefore considered good practice to use either an approximate derivative or a sensor that can measure the derivative directly, rather than numerically differentiating the error signal. In this manner, the noise can largely be avoided. As an example, for attitude control of spacecraft, rather than differentiate the change in measured orientation at each time step, a rate gyroscope directly measures the body rates.

2.6.2   Linearized Attitude Control.   Because the PID control algorithm is a linear controller, it is not guaranteed to be stable with a system that has nonlinear kinematics, as described by Euler's equation, Eq. (2.17). As detailed in Section 2.4.1, quaternions are approximately linear between ± 0.6 radians. Because the controller operates on the difference between the desired orientation and actual orientation, the error is usually within this range, and can therefore be assumed to be linear; however, the nonlinear dynamics cannot be ignored and are addressed via feedback linearization. In the feedback linearization technique, the nonlinear terms in the dynamics are calculated, then incorporated into the control signal to cancel out the nonlinearities, as shown in Figure 2.26.

Using Euler's equation, restated for convenience as

$$\vec{M} = \mathbf{I}\dot{\vec{\omega}}_{bi} + \vec{\omega}_{bi} \times \mathbf{I}\vec{\omega}_{bi}, \tag{2.64}$$

the control variable is the applied moment $\vec{M}$, and $\vec{\omega}_{bi} \times \mathbf{I}\vec{\omega}_{bi}$ is the nonlinear term which must be addressed, with the goal of $\dot{\vec{\omega}}_{bi}$ being linearly related to the control input $\vec{M}$.

43
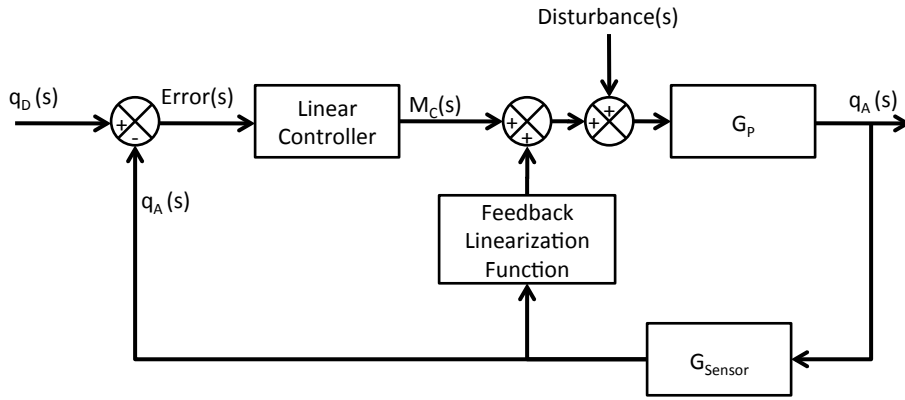
Figure 2.26:   Feedback Linearization

This nonlinearity is addressed by splitting the control term $\vec{M}$ into two components, as shown in Figure 2.26, or

$$\vec{M} = \vec{M}_{LC} + \vec{M}_{NLC} \tag{2.65}$$

where $\vec{M}_{LC}$ is the control signal from the linear controller and $\vec{M}_{NLC}$ is specified to cancel out the $\vec{\omega}_{bi} \times \mathbf{I}\vec{\omega}_{bi}$. Substituting Eq. (2.65) into Eq. (2.64) and setting $\vec{M}_{NLC} = \vec{\omega}_{bi} \times \mathbf{I}\vec{\omega}_{bi}$ yields

$$\vec{M}_{LC} + \vec{\omega}_{bi} \times \mathbf{I}\vec{\omega}_{bi} = \mathbf{I}\dot{\vec{\omega}}_{bi} + \vec{\omega}_{bi} \times \mathbf{I}\vec{\omega}_{bi} \tag{2.66}$$

which simplifies to

$$\vec{M}_{LC} = \mathbf{I}\dot{\vec{\omega}}_{bi}. \tag{2.67}$$

We now have the desired linear relationship between $\vec{M}_{LC}$ and $\dot{\vec{\omega}}_{bi}$, allowing the use of a linear controller. Furthermore, feedback linearization can decouple the equations of motion, which allows for the use of an individual PID controller for each axis to provide full three-axis control, as shown in Figure 2.27.[34]

2.7 Electric Motors

Electric motors are devices that turn electrical energy into kinetic energy. Motors are used on the satellite simulators to turn the gimbal axis on the CMGs, spin the CMG flywheels and the reaction wheels, and turn the fan blades for the ducted fan

44
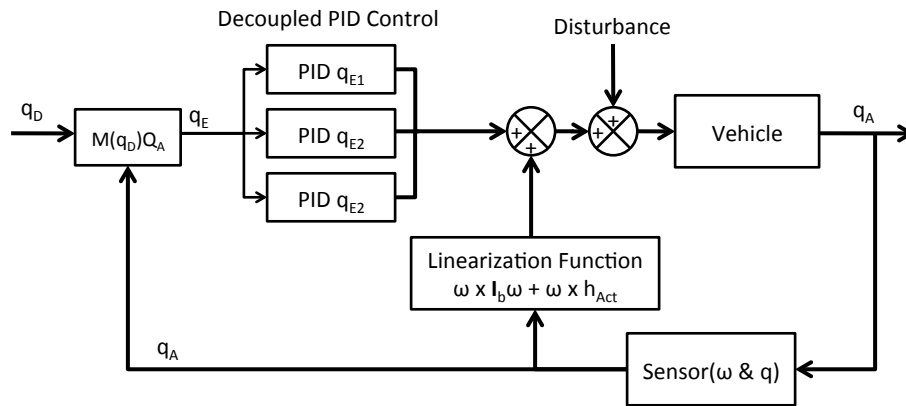
Figure 2.27:   Three-Axis Linearized PID Controller

subsystem. Electric motors produce force through the manipulation of the interaction between electric current and a magnetic field, as described by Faraday's law of induction. Faraday's law of induction states:

> *The induced electromotive force in any closed circuit is equal to the negative time rate of change of the magnetic flux through the circuit.[35]*

Electric motors can be powered using alternating current (AC), or direct current (DC). The ACSPG uses DC motors powered by lithium-polymer batteries.

The two most common types of DC motors are the brushed and brushless types. Although other types of DC motors exist, they are not as common. All brushed motors are made up of the same basic components: a stator, rotor, brushes and a commutator. The stationary magnetic field surrounding the rotor is generated by the stator. The stator generates this field either with permanent magnets or electromagnetic windings. The rotor is made up of one or more windings, which when energized, produce a second magnetic field. The magnetic poles of the rotor's magnetic field are attracted to the opposite poles of the stator's magnetic field, causing the rotor to turn. So that the magnetic poles generated by the rotor do not overrun the poles generated by the stator, the windings are constantly being energized in a different sequence as they turn, through a process called commutation. In brushed DC motors, the commutation of the windings is done mechanically with the brushes. As the motor turns, carbon brushes slide over the commutator, a segmented copper sleeve on the axle of the motor. Each segment of

45

the commutator is attached to a different rotor winding. As the brushes slide across the commutator, they dynamically change the orientation of the magnetic field. Because the brushes and commutator are sliding past one another, they are prone to wear and can produce unwanted debris, vibration, and electrical noise. For these reasons, brushed motors were not considered a viable option for use on the ACSPG's ACS.[36]

Brushless DC motors work using the same principles as brushed DC motors, but achieve commutation without brushes. Instead, commutation is achieved electronically. Compared to brushed DC motors, brushless DC motors require less maintenance, have longer lives, are more efficient, run smoother, offer a higher speed range, and offer a superior power-to-size ratio. These advantages come at the expense of a more complex control requirement and a more expensive motor requiring permanent magnets. Brushless DC motors are rotated by energizing the stator windings in sequence, resulting in the desired force between the stator winding and a permanent magnet inside the motor. A Hall effect sensor embedded in the stator senses the rotor position to ensure the correct stator energization for torque or speed control. A controller, usually manufactured by the same company as the motor, controls the commutation to ensure the motor runs at the correct speed. Brushless DC motor/controller systems are used in the ACSPG CMGs to spin the rotor and gimbal angle control. Details on rotor and gimbal motor and controller selection can be found in Sections 3.4.2 and 3.5.1, respectively.[37]

2.8 Bearings

Bearings are used to allow for relative freedom of movement in one or more degrees of freedom between two surfaces while constraining relative motion in all other directions. For example, spherical air-bearing allows for three degrees of freedom, roll, pitch, and yaw, while constraining all translational degrees of freedom, whereas a planar air-bearing allows for freedom in x, y, and yaw, while z, pitch, and roll are constrained. A ball bearing is a special type of bearing which allows one object to spin relative to another with low friction while keeping all other degrees of freedom constrained. A ball bearing is made up of three basic parts: the inner raceway, the outer raceway, and the balls. The balls are allowed to roll between the inner and outer raceways, allowing for freedom of motion

about the bearing's spin axis. Ball bearings were used on the CMG design to allow the rotor to spin freely relative to the motor and rotor housing support structure. Ball bearings were also used to allow the gimbal shaft to spin freely relative to the gimbal support housing and gimbal motor. Ball bearings come in many different types and sizes. Details on rotor and gimbal bearing selection can be found in Sections 3.4.3 and 3.5.2, respectively.

2.9   Unbalance

The most common source of vibration in machines with rotating parts is unbalance.[38] Unbalance is caused by an uneven distribution of mass in an object about its rotation axis. The interaction between the unbalanced mass component with the radial acceleration due to rotation generates a centrifugal force that rotates about the spin axis. Because this force continually changes direction with the rotating object, the result is a vibration. There are two types of unbalance: static unbalance and couple unbalance. Static unbalance is defined as the difference in location between a rotor's center of gravity and center of rotation. This difference is also called eccentricity. If a rotor has a diameter more than 7 times its width, it can be treated as a single-plane rotor, for which the only unbalance is static.[38] If the rotor has a diameter less than 7 times its width, it cannot be treated as a single-plane rotor, and a second type of unbalance, known as couple or moment unbalance, must also be considered. Couple unbalance is the result of a rotor's axis of rotation not being aligned to a principal axis. Dynamic unbalance is the combination of both types of unbalance. Dynamic unbalance is the most common type of unbalance. The rotor's balance, or "G" number, is the product of the rotor's eccentricity and the angular velocity of the rotor at maximum operating speed.[38]

$$G = e \times \omega, \tag{2.68}$$

where a lower value indicates a better level of balance. Balance quality grades have been established for various groups of representative rigid rotors based on the acceptable level of vibration. An acceptable level of balance for gyroscopes is G 0.4 or better. For comparison, crankshafts in modern automobile engines are G 100 or better.[38]

47

2.10 Summary

Chapter II provided the background information on satellite simulators as well as past work done by AFIT in the field of satellite simulation. Spacecraft dynamics were then discussed, primarily addressing momentum exchange and CMG dynamics in a way to supplement the development efforts that are presented in Chapter III. PID control was then introduced. The chapter concluded with a brief description of electric motors, bearings, and balance quality.

III. Methodology

3.1 Introduction

Chapter III covers the methodology behind the design, construction, and testing of the CMGs built for use on the ACSPG. Other CMG manufacturers, such as Honeywell and Ithaco, consider their design methodology proprietary. As such, it was necessary to develop our own process of designing, building, and testing CMGs for the ACSPG. Although this process was developed specifically for the design of the CMGs used on the ACSPG, this process can be applied to the design of most any CMG system. Therefore, there were two products developed in this research effort: the physical CMG system to be used on the ACSPG, and a CMG design, build, and test process and capability. Section 3.2 covers the design methodology that was developed for this effort.

Following Section 3.2, the rest of Chapter III details how the process outlined in Section 3.2 was applied to the CMGs designed for the ACSPG. Section 3.3 outlines the requirements that the CMG array must meet. Sections 3.4 and 3.5 cover the design of the rotor and gimbal subsystems on the CMG, respectively, with an emphasis on how the CMG was designed to meet the requirements listed in the Section 1.2. Section 3.6 discusses the simulations of the ACSPG's ACS. Finally, Section 3.7 covers the methods used to test the prototype CMG for the ACSPG.

3.2 Design Process

Prior to this research effort, AFIT had minimal experience developing CMG systems. Work by McChesney[3] on SimSat served as a starting point; however, that system has vibration levels higher than desired, making it audibly noisy. The SimSat CMGs are much smaller than the system for use on the ACSPG, which meant that designing CMGs for use on the ACSPG was not simply a matter of resizing the CMGs used on SimSat. Figure 3.1 outlines the design process that was developed and used for this research effort. Although it has only been applied successfully to the CMGs designed for the ACSPG; it is purposefully generalized in a manner that it can be applied to the design of any CMG system.

49
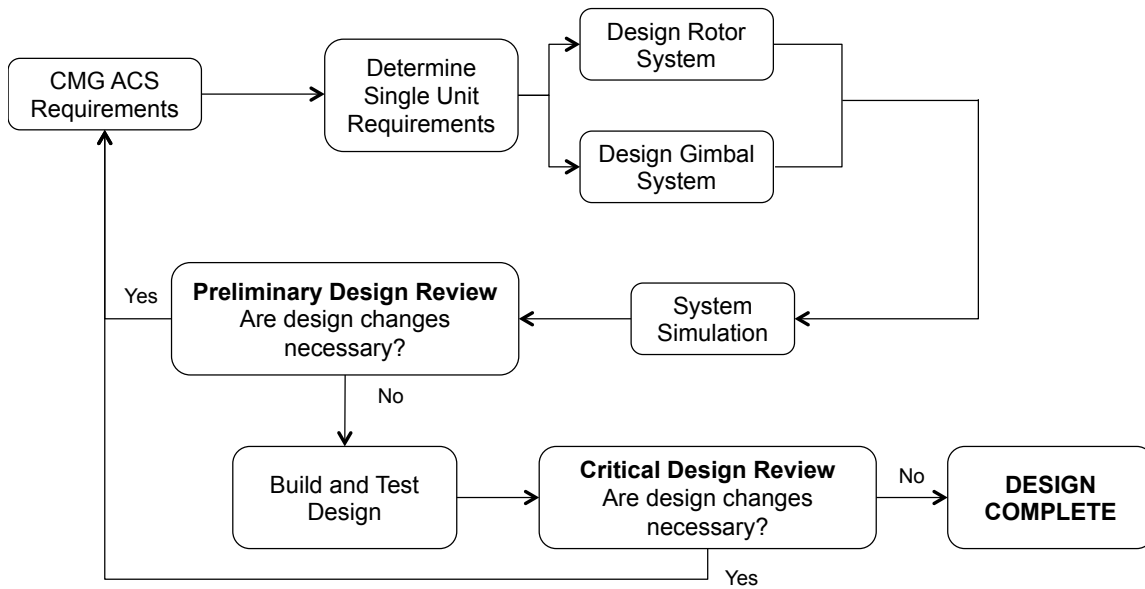
Figure 3.1:   CMG ACS Design Process

Figure 3.1 gives a broad, top-level view of the design process developed for this effort. Attempting to design a CMG using only this information would be like attempting to navigate a New York City neighborhood using a globe. Without some refinement and additional clarity, it is useless. Therefore, each box is broken down if possible, to give the user more specific direction.

First, the box labeled "CMG ACS Requirements" is expanded in Figure 3.2 to show all possible requirements for a CMG actuated ACS. Boxes that are highlighted indicate that the customer or sponsor should set these requirements. If possible, the designer should ask for sponsor input on all of the requirements listed here. These requirements should be driven by the mission; therefore, the spacecraft's mission must be established and clear before the requirements can be set.

The next step in the design process is to determine the requirements for each individual CMG. This box is similarly expanded in Figure 3.3. Sponsor input is recommended here as well, everywhere possible. Boxes shaded orange indicate a derived value. The angular momentum storage requirement is derived from the max angular velocity requirement, max principal MOI of the vehicle, beta angle, and the array configuration.

50
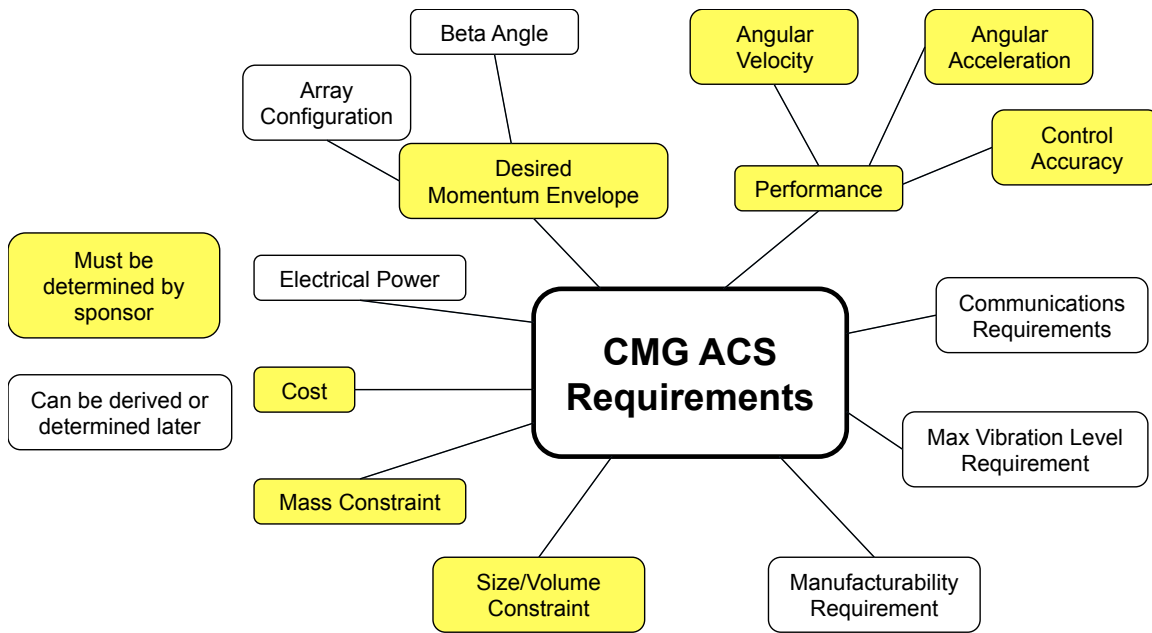
Figure 3.2:   CMG ACS Requirements

The torque requirement design factors are the same, with the max angular acceleration requirement replacing the max angular velocity requirement.
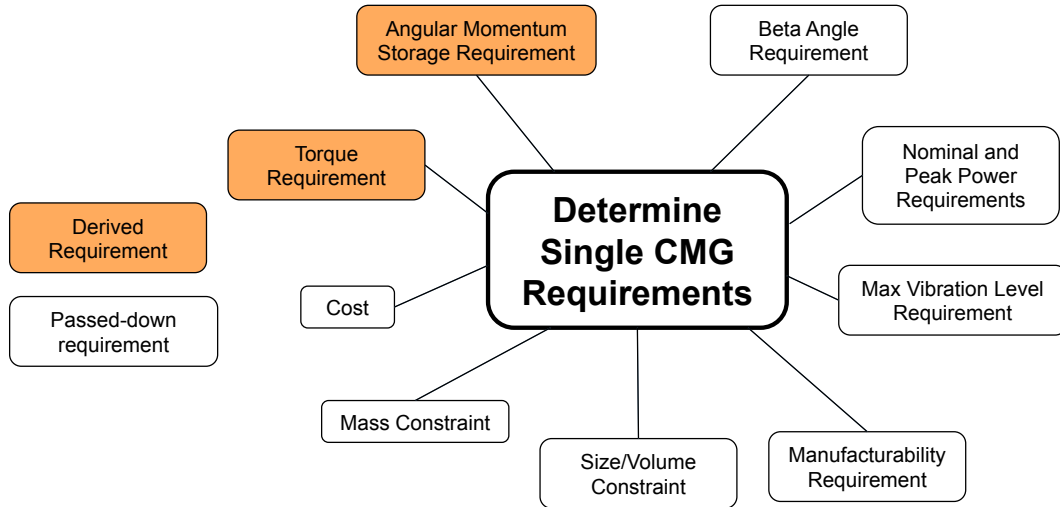
Figure 3.3:   Single CMG Requirements

Once the single CMG requirements have been determined, design can begin on the rotor and gimbal subsystems. Figure 3.4 shows the design webs for the rotor and gimbal subsystems for a CMG. Boxes connected to the large center box represent an aspect of that representative system. Arrows indicate the direction of design drivers:

51

For instance, the angular momentum storage requirement drives both the speed and the size and shape of the rotor. Some design aspects influence each other, either directly or indirectly: For example, the required angular momentum may be achieved by spinning a rather small rotor fast, or a larger rotor somewhat slower. These design aspects drive each other directly. If the rotor speed is limited by motor choice, the size and shape of the rotor are indirectly driven by the motor selection; therefore, the selection of the motor directly drives the design rotor speed, and indirectly drives the rotor shape and size.

The next step in the process is a system simulation. Simulation is necessary to determine if the system meets the performance requirements while ensuring the system does not saturate. Ideally, this simulation should accurately simulate the operation of the ACS and spacecraft in a manner similar to how it will operate as hardware. In this effort, a MATLAB model was created to simulate the dynamics of the ACSPG and CMG ACS. A second MATLAB script was used to determine the momentum envelope of the CMG array. To ensure hardware performance meets requirements, simulations should be conducted for operating conditions that are more difficult than those actually anticipated on the hardware, or performance margins should be designed into the system to account for inefficiencies or system growth. For the sake of simulating an ACS, the principal MOIs of the vehicle in the simulation should be larger than the expected values to ensure control or torque margin when the hardware is assembled. This technique will provide a performance margin, which is critical if the vehicle parameters change after the ACS has been designed. Further discussion of how simulation was used as a design tool, as it related to the design of the ACSPG CMGs, is discussed in Section 3.6.

Following simulation, the next step is the preliminary design review (PDR) of the CMG ACS. The designer should first determine if the CMG design is complete, and potentially ready to be built. Next, the designer must determine if the simulated performance of the ACS is satisfactory. If possible, the designer should also keep the customer or sponsor "in the loop," as the customer or sponsor may have design tweaks they would like included. The purpose of the PDR is to determine if there are CMG or ACS design changes necessary before the design is built and tested.
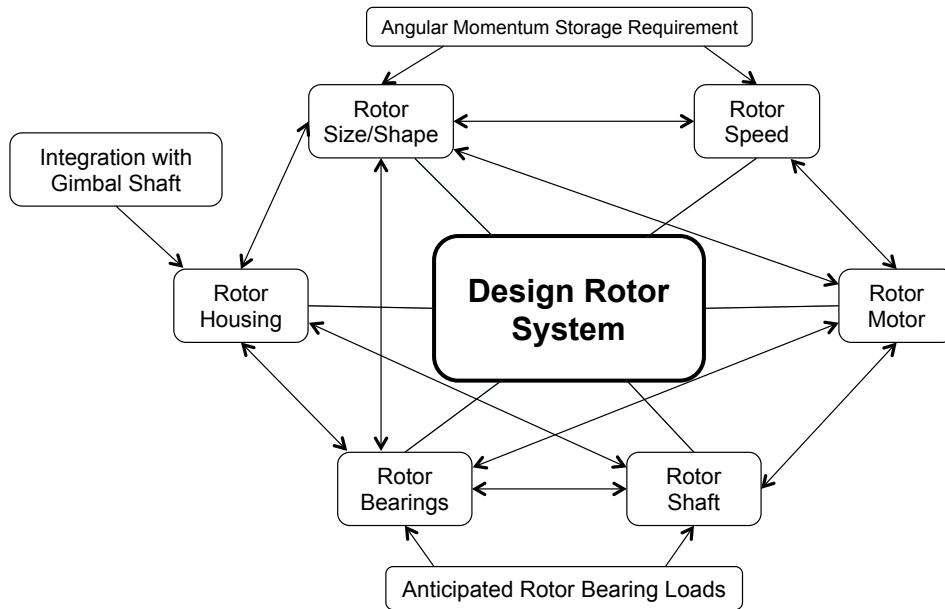
(a) Rotor System Design
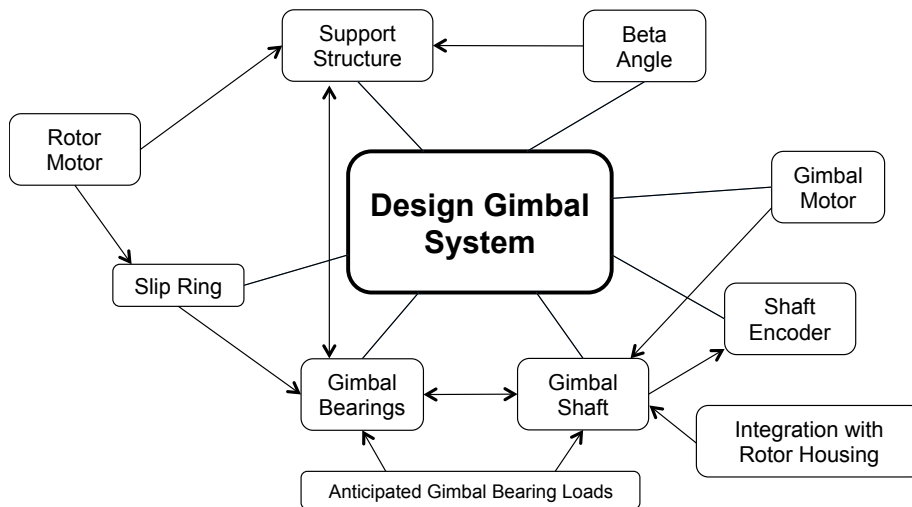
(b) Gimbal System Design

Figure 3.4:   Subsystem Design Webs

Once the PDR has been completed with the conclusion and all design changes have been made, the design should be built and tested. If possible, a prototype CMG should be built and tested before the entire system is built, as test results and manufacturing lessons learned may prompt design changes. Testing should be conducted to prove that the prototype CMG works satisfactorily as designed. These tests should include, at

53

minimum, a full system checkout and subsystem tests to ensure the hardware works as designed and meets its performance requirements.

Following hardware testing, a critical design review (CDR) should be conducted to determine if there are any final changes to the design necessary. If the CMG does not work satisfactorily as designed, changes to the design should be made. In some cases, design changes may mean a complete design overhaul; in other cases, design changes may be as simple as increasing the nominal CMG rotor speed to increase momentum storage capacity in the system. Sponsor or customer feedback should be incorporated at this stage as well. For example, if the design does not achieve performance goals, the sponsor may decide that the performance goals or ACS requirements may be changed to accommodate the design, or the sponsor may decide that design change is necessary. Once the design has undergone the CDR and after completing all final changes, the design can be considered complete.

The rest of Chapter III specifies how the design process detailed in this section was applied to the development of the CMG system for use on the ACSPG.

3.3   Requirements

3.3.1   CMG array requirements.   The requirements for the CMG array, as defined by AFRL Space Vehicles Directorate, are as follows: (restated from Section 1.2

- Max angular velocity of the ACSPG with a payload and under control of the CMG ACS must be not less than $10°/s$.

- Max angular acceleration of the ACSPG with a payload and under control of the CMG ACS must be not less than $10°/s^2$.

- The inclination angle of the gimbal on the CMGs will be a fixed $45°$.

- The CMG array should be configured such that a 4-CMG pyramid array, 4-CMG rooftop array, and 6-CMG rooftop array can be mounted on the underside of the ACSPG.

- The CMG system should be designed to have minimal acoustic noise and vibration.

54

- The CMG system must have a minimum lifetime of 15 years, with minimal to no maintenance requirements.

At $10°/s^2$ angular acceleration and $10°/s$ angular velocity, the ACSPG is designed to simulate the behavior of a particularly highly maneuverable satellite, as most CMG equipped satellites reach maximum design speeds of only 4-5°/s.

3.3.2 CMG Prototype Requirements. Working from the CMG array requirements in Section 3.3, the requirements of each individual CMG in the array can be deduced. Using computer-aided design (CAD) software, the principal moments of inertia of the ACSPG with a payload and the CMG array were estimated. The largest principal MOI is I_{zz}, estimated to be 686.1 kg-m^2. This estimate included the mass properties of the ACSPG with the tilt limiter and CMG array attached. A $10°/s$ rotation about the z-axis of the ACSPG results in an angular momentum of 119.75 N-m-s, which must be entirely transferred to the spacecraft from the CMG array. Because the maximum principal MOI of the ACSPG is about its z-axis, the absolute value of the difference between the maximum positive z-axis value and minimum negative z-axis value of the CMG array's momentum envelope must be greater than 119.75 N-m-s. To meet this requirement, the individual CMGs must have an angular momentum greater than or equal to 21.2 N-m-s. This value was determined using the MATLAB program that calculates the momentum envelope of CMG arrays, as discussed in Section 2.5.

To meet the angular acceleration requirement, the CMG array must be able to achieve 119.75 N-m of torque to produce an angular acceleration of $10°/s^2$ around the body frame z-axis. A CMG produces torque by changing the gimbal angle, where the rate of change of the gimbal angle required to produce the necessary torque is dependent on array configuration, inclination angle, gimbal angles, max gimbal rate, max gimbal acceleration, and rotor angular momentum. Knowing this requirement at this stage does not explicitly influence the design of the CMG because there are multiple variables that influence gimbal rate; however, analysis of the simulation results can ensure that this requirement is met.

3.4   Rotor System Design

This section covers the design of the rotor system. For ease of understanding, an annotated and exploded view of the rotor system is shown in Figure 3.5.
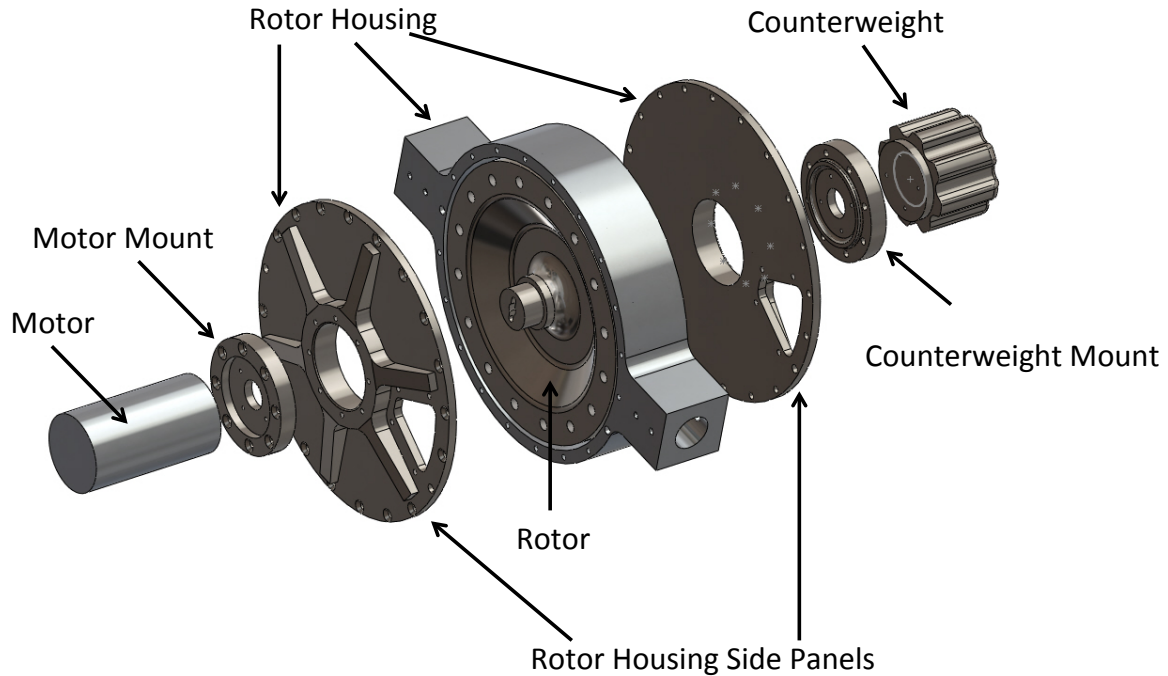
Figure 3.5:   Rotor System Components

3.4.1   Rotor Design.   Before starting this research effort, we had an approximate idea for the design of the rotor, shown in Figure 3.6.
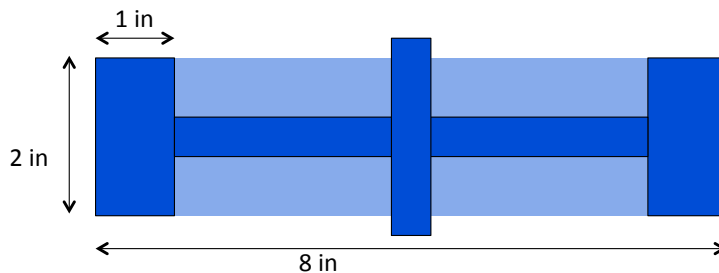
Figure 3.6:   Preliminary Rotor Design

Upon a PDR, the sponsor requested that the inner corners of the outer ring be rounded, as shown in Figure 3.7, to ensure that fluid and materials will not be caught on the rotor lip while the rotor is spinning, thereby creating unbalance.
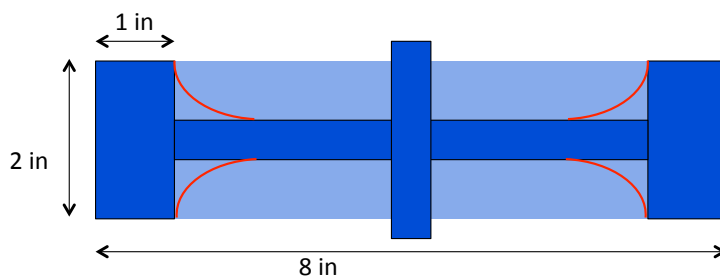
Figure 3.7:   Revised Rotor Design

A brainstorming session then led to the design of the rotor shown in Figure 3.8. This design meets the sponsor's intent of smoothly ejecting debris and fluid from the inside of the rotor, while being easier to grind and balance than a filleted design, shown in Figure 3.7. As an added benefit, adding the angled section increases the MOI about the spin axis, resulting in increased system angular momentum and performance for the same rotor speed.

To reduce vibrations caused by unbalance, a total of 16 3/8-inch plugs were added and evenly spaced on each side, as shown in Figure 3.9. Because the rotor diameter is less than 7 times its width, it cannot be treated as a single-plane rotor. To enable correction to moment unbalance, the plugs are phased by 11.25° from one side of the rotor to the other. Behind the plugs, there is space to add lead shot. By adding small amounts of material, the rotors can be fine tuned such that the center of mass is in line with the center of rotation. This design feature greatly improves the achievable balance quality of the rotor.

3.4.2 Rotor Motor Selection.   Power to spin the rotor is supplied via a brushless DC motor. We selected three candidates based on their catalog specifications, the Maxon EC 60 Flat (Maxon Part No 408057), the Maxon EC 45 (Maxon Part No 136202), and the Moog Silencer BN23-23CJ-04CH, shown in Figure 3.10. Accelerometers were placed on the top and side of each motor, as shown in Figure 3.11, and vibration measurements

57
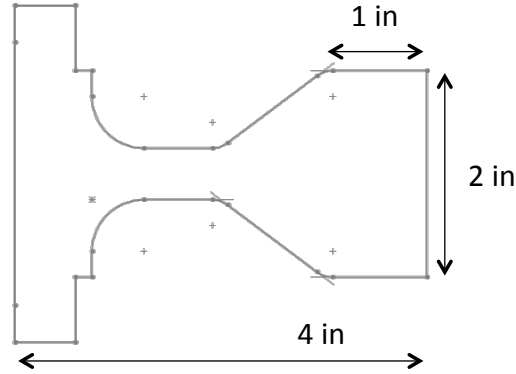
Figure 3.8:   Final Rotor Design

were recorded for a range of motor speeds, then plotted for comparison. Speed was measured using a strobe, then recorded along with the vibration measurements. At first, the accelerometers were attached to the motor with beeswax; however, after running the Moog BN 23 for only a few minutes, the motor casing was so hot that it melted the beeswax, and the accelerometers detached from the motor. Further tests were conducted using masking tape to attach the accelerometers to the motors, as shown in Figure 3.11. Although masking tape is a less ideal accelerometer attachment method than beeswax or superglue, the technique used was consistent, and the results were repeatable. Furthermore, the vibration measurements between the three motors were distinct enough that it is safe to say use of tape to attach the accelerometers to the motors and the boundary conditions (foam support) did not impact the motor selection.

Figure 3.12 shows the relative vibration levels for the Maxon EC 45 and Moog BN 23 at 6000 rpm, which is the design rotor speed, and the Maxon EC 60 Flat at 4000 rpm. The Maxon EC 60 Flat was run at 4000 rpm because it cannot reach 6000 rpm, and 4000 rpm would be the nominal rotor speed if the EC 60 Flat were selected. A number of runs were conducted at this speed and at varying rotor speeds. For all cases, the EC 45 had the lowest levels of vibration, and Figure 3.12 is representative of each comparison test. Note that in Figure 3.12 the vertical axis is in decibels.

During the motor tests, a laser temperature scanner was used to measure the temperature on various locations on the motor case during the tests. The Moog BN 23 had a max recorded case temperature of 59°C, while the Maxon EC 45 had a max case

58

Balance Plug Holes
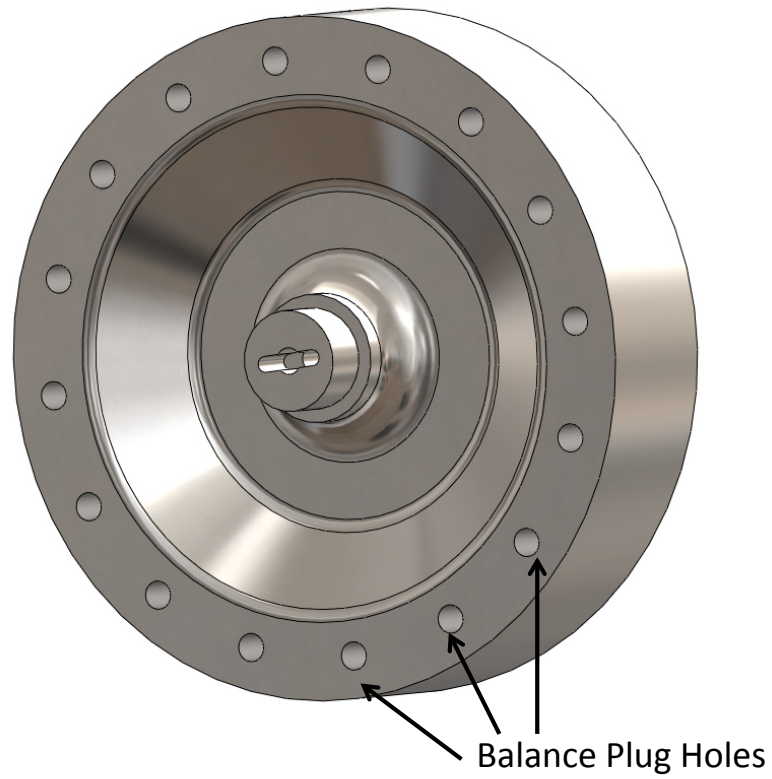
Figure 3.9:   CAD model of Rotor
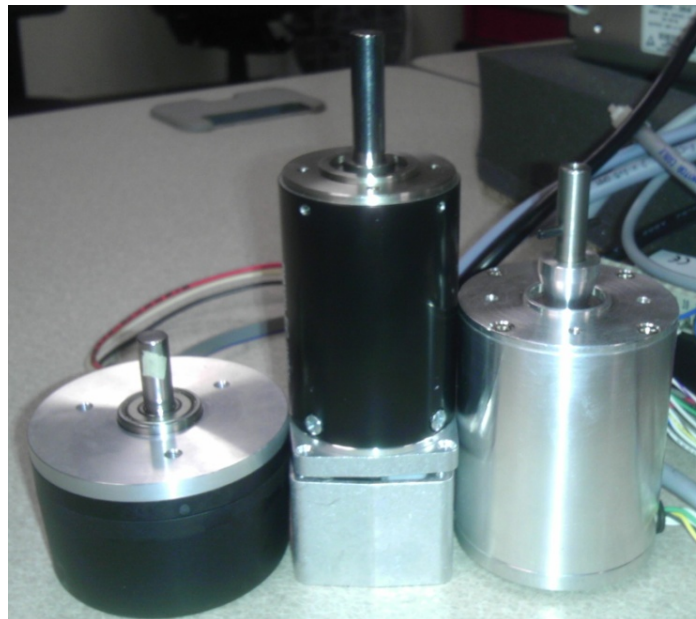
Figure 3.10:   Rotor Motor Candidates from left to right: Maxon EC 60 Flat, Maxon EC 45, Moog BN 23

59
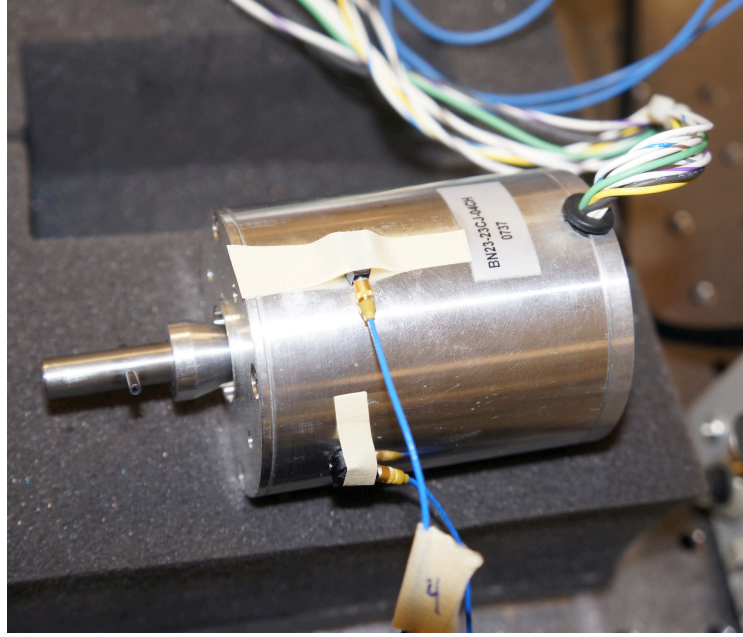
Figure 3.11:   Moog BN 23 Vibration Test Setup - Motor is resting on foam

temperature of 39°C, and the Maxon EC 60 Flat had a maximum recorded temperature of 38°C. Because minimizing vibration and audible noise was one of the sponsor's goals for the design of this CMG, the motor selected was the one with the least amount of vibration. Lower heat is expected to correlate to longer life and higher efficiency. The Maxon EC 45 was selected for use as the CMG rotor motor, as it had both the lowest levels of vibration and lowest case temperature for all speeds tested. Since Maxon motors have been used for several years by AFIT researchers, their use was already well understood, which was an additional benefit of selecting this motor. The motor is controlled with a Maxon EPOS 70/10 digital speed controller.

3.4.3 Rotor Bearing Selection.   Bearings between the rotor shaft and the rotor housing allow a degree of freedom about the rotor's spin axis while also constraining relative motion in all other dimensions and transferring any radial or axial loads to the rotor housing. To ensure proper bearing selection, it was first necessary to determine the rotor bearing radial and axial loads. First, we will discuss the calculation of the bearing radial loads.

60
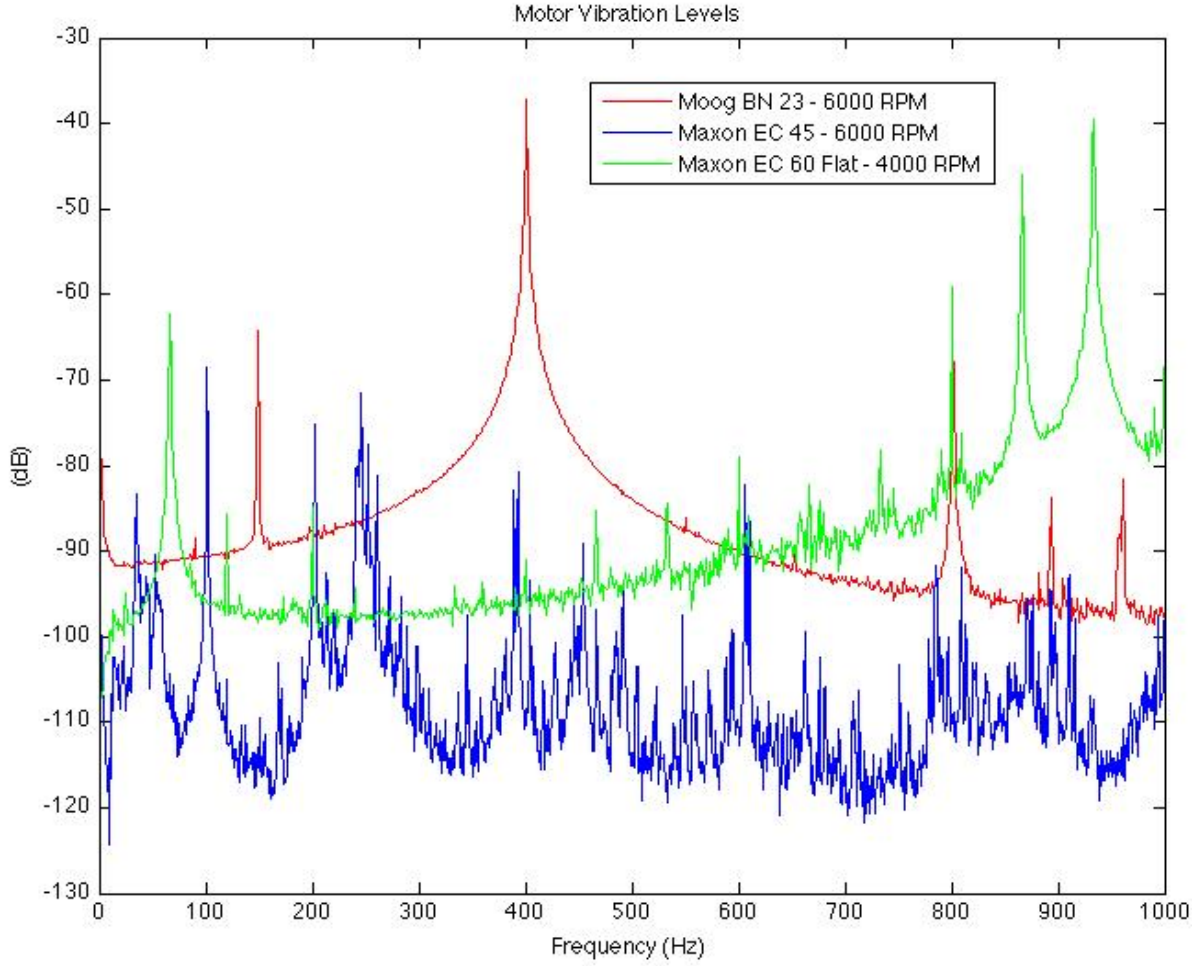
Figure 3.12:   Relative Motor Vibration Levels

Recalling Eq. 2.29 from Chapter II, torque produced by the CMG is

$$\vec{\tau}_{control} = \dot{\vec{h}}_{cmg} = \vec{\omega}_g \times \vec{h}_0 \tag{3.1}$$

where $\vec{\omega}_g$ is the gimbal rate and $\vec{h}_0$ is the angular momentum of the CMG rotor. The maximum gyroscopic torque on the rotor is

$$\vec{\tau}_{gyro} = \vec{\omega}_{s/c} \times \vec{h}_0 \tag{3.2}$$

where $\vec{\omega}_{s/c}$ is assumed to be the max angular rate of the spacecraft. According to the sponsor, the max desired angular rate is required to be not less than $10°/s$; however, it

61

could be more than that. Therefore, we determined that the max angular rate of the spacecraft would be when the CMG array is in a 6-unit rooftop configuration, and each CMG transfers as much angular momentum as possible into rotating the spacecraft about its smallest principal MOI, as reflected in Eq.(3.3). The value used in this equation represents a theoretical bound for the spacecraft's maximum angular rate achievable under CMG control; however, this maneuver is dangerous and definitely not encouraged in an unconstrained environment, as it could cause a pedestal strike and severe shock for the ACSPG.

$$\vec{\tau}_{gyro} = \vec{h}_{array}2/I_{min} \times \vec{h}_0 \tag{3.3}$$

Rotor weight must be included as well, as shown in Figure 3.13. Assuming a vertical orientation, a max of exactly half of the rotor's weight will exert radial force on each bearing.

Although the spacecraft's angular acceleration imparts a relative linear acceleration on the control moment gyro, at $10°/s$, the radial force on the bearings is still two orders of magnitude less than the gimbal and gyroscopic forces. This force is therefore neglected.

Figure 3.13 shows the free body diagram that was created for this maximum load case. Other loads, including system shock caused by spacecraft pedestal strike and rotor unbalance, were neglected for this case. System shock by pedestal strike should never happen; however, if it does, the ACSPG is equipped with a foam lined angle limiter, which should mitigate a potentially severe system shock. Loads caused by rotor unbalance were deemed to be insignificant in comparison to the larger radial loads caused by the control torque and gyroscopic forces.

From this diagram, the maximum radial loads on the bearing were determined to be

$$c_{r_{max}} = |\vec{\tau}_{control} + \vec{\tau}_{gyro}|/w_{rotor} + m_{rotor}g/2 \tag{3.4}$$

which can be expanded to become

$$c_{r_{max}} = |\vec{\omega}_g \times \vec{h}_0 + \vec{h}_{array} \times 2/I_{min} \times \vec{h}_0|/w_{rotor} + m_{rotor}g/2. \tag{3.5}$$
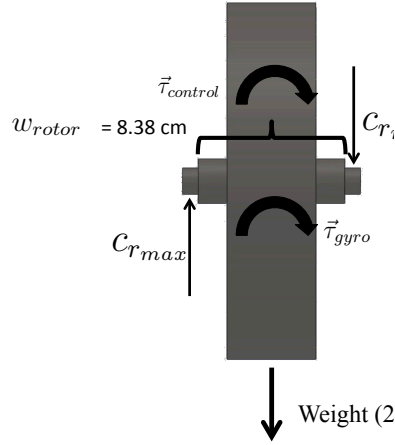
Figure 3.13:   Radial Rotor Bearing Loads

where w_{rotor} is the distance between each rotor bearing. The maximum torque on the rotor, determined by adding $\tau_{control}$ and τ_{gyro}, is 210.4 N-m. The maximum radial load on the rotor bearings $c_{r_{max}}$ was determined using Eq. 3.5 to be 575.5 lbf.

Axial loads were also considered. The only axial loads on the bearing are the preload and the weight of the rotor. If the spacecraft is oriented such that it is pitched perfectly to offset the gimbal angle on a CMG, the weight of the rotor will rest entirely on the bearing beneath it. Spacecraft angular acceleration was once again neglected. The maximum axial bearing load is therefore equal to the weight of the rotor plus any preload applied to the rotor bearings. For the current design, the weight of the rotor is 21.82 lbs. From the bearing manufacturers specifications, the required preload is estimated to be between 20 and 40 lbs. As previously discussed, spacecraft angular acceleration, system shock, and unbalance loads are very small, and therefore were neglected.

$$c_{x_{max}} = m_{rotor}g + c_{x_{preload}}. \tag{3.6}$$

With the maximum rotor bearing loads now estimated, it was possible to select a bearing. To ensure the bearing would have adequate running life, a factor of safety of at least five was chosen as a requirement. It was also decided that the bearings should meet all ABEC-7 standards as a minimum, to ensure adequate vibration and precision characteristics. Sealed or shielded deep groove ball bearings were deemed appropriate for

63

this application. Having a shielded or sealed inner raceway is desirable to ensure debris does not enter the bearing, which can cause bearing failure. The use of deep groove ball bearings were selected over angular contact bearings because angular contact bearings in CMG designs have failed when they lost preload.[39] The final selection criteria was that the bearings needed to be in stock, since prototype testing could not tolerate the addition of a four-month lead time to build bearings. The bearings chosen, with the help of engineers from the Barden Bearing Corporation, were Barden 206FFT3 deep groove spindle bearings.

Table 3.1:   Barden 206FFT3 Ball Bearing Specifications[1]

Specification	Value
Bore Diameter (d)	30.000 mm
Outside Diameter (D)	62.000 mm
Width (B)	16.000 mm
Static Radial Load Capacity (C_0)	2943 lbs.
Static Thrust Load Capacity (T_0)	2508 lbs.
Basic Dynamic Load Rating (C)	4288 lbs.
Shield Type	Flexeal
Lubricant	Grease
Attainable Speed	28,333 rpm
ABEC Rating	7

The bearings are press fit onto the rotor shaft and held in place with the rotor motor/counterweight mounts. The motor/counterweight mount also provides preload on the rotor bearings. The outer raceway of one bearing is pressed into the rotor housing while the other is slip fit to allow for preload adjustment.

3.4.4   Rotor Shaft Design.   Now that the general rotor design, rotor bearing selection, and rotor motor selection are all complete, finishing touches can be applied to the rotor shaft design. The selected bearings have very specific fit requirements, which drove the design of the shaft near the bearings. To ensure the strength of the shaft would be adequate, a fillet was added between the shaft and inner rotor face, as shown in Figure 3.14. finite element analysis (FEA) was then done to confirm that the rotor shaft would be able to easily handle all the anticipated loads while also providing a suitable factor

64

of safety. Figure 3.14 also shows the motor keyhole was added to the rotor shaft ensure the motor shaft will not slip inside the rotor.
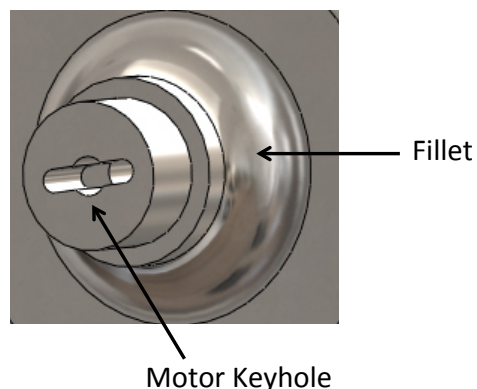
Figure 3.14:   Rotor Shaft Design

3.4.5 Rotor Housing Design.   The rotor housing transfers the torque supplied by the rotor to the CMG gimbal assembly; therefore, it must be adequately strong. To minimize air drag on the rapidly spinning rotor, it was decided that the rotor housing should be completely enclosed. A hermetically sealed and evacuated housing was considered; however, we found that this would add unnecessary complexity and cost to the system, and that a simple enclosed system was more suitable for the sponsor's needs. The rotor housing transfers the bearing loads to the gimbal shaft. To ensure that the housing would be able to handle these loads, FEA was done on the rotor housing. The first design for the rotor housing included simple discs for the sides of the housing, shown as parts 3 and 6 in Figure 3.5. We calculated that these discs had regions where the von Mises stress was 50% of the yield stress under the anticipated loads while maintaining a satisfactory factor of safety, so the housing sides were redesigned with ribs. We also changed the material on the housing sides to a hardened steel, which was suggested by the bearing manufacturer. The reason for CMG failure on the International Space Station was because the material in contact with the bearing's outer raceway was not suitably hard [39]; therefore, this aspect of the design is critical. FEA was then completed on the new design, proving it would sufficiently carry the anticipated loads while maintaining an adequate factor of safety.

65

3.5 Gimbal System Design

This section covers the design of the gimbal subsystem. For ease of understanding, an annotated and exploded view of the gimbal subsystem is shown in Figure 3.15.
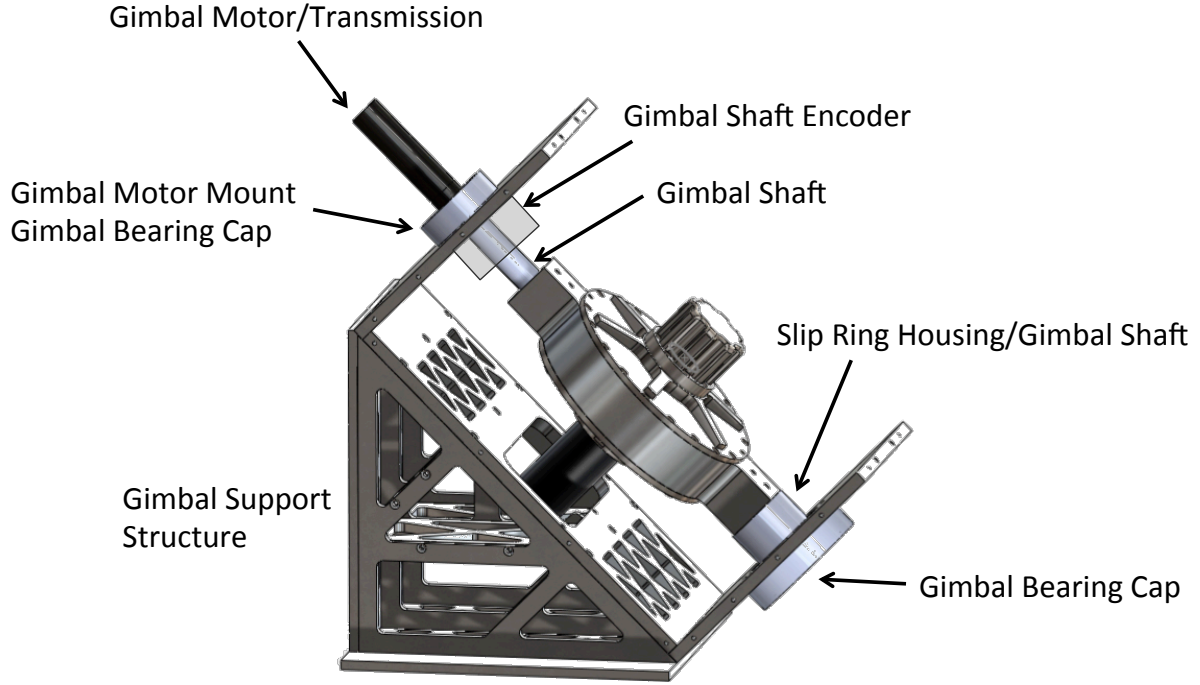
Figure 3.15:   Gimbal System Components

3.5.1 Gimbal Motor Selection.   SimSat's CMGs use a Maxon EC-Max 30 (Maxon Part No 272763) with a Maxon GP-32 159:1 transmission (Maxon Part No 326671). This motor and transmission is capable of 8 N-m of continuous torque, with 12 N-m peak intermittent torque. The torque required to turn the gimbal shaft and rotor is governed according to the following equation:

$$\tau_{r_g} = I_e \alpha_g + w_{s/c} h_{rotor} \tag{3.7}$$

where I_e is the effective gimbal inertia, as given by

$$I_e = I_g + h_{rotor}^2 / k, \tag{3.8}$$

where k is the torsional stiffness of the gimbal shaft. Solving for $\vec{\alpha}_{gimbal}$, and using the maximum values for each term, it can be determined if the motor torque is sufficient for control. If $\vec{\alpha}_{gimbal}$ is a positive value, some level of control can be achieved with the CMG.

$$\alpha_{gmax} = (\tau_{gmax} - w_{s/c}h_{rotor})/I_e > 0 \tag{3.9}$$

Equation (3.9) can be changed as necessary to reflect a desired amount of control greater than 0. Because the Maxon EC-Max 30 and GP-32 transmission were able to achieve a satisfactory level of control at all anticipated spacecraft rates, it was selected for use on the ACSPG CMGs. The selected motor transmission combination can theoretically achieve at least 10.4 rad/s^2 angular gimbal acceleration, although it will likely be governed to only 5 rad/s^2 angular gimbal acceleration.

3.5.2 Gimbal Bearing Selection. The gimbal bearings were selected in the same manner as the rotor bearings. First, a free body diagram was made to determine the maximum anticipated radial and axial loads on the gimbal bearings, shown in Figure 3.16. The figure shows the CMG in a 45° canted orientation, to represent a 45° spacecraft pitch angle. This configuration is used because it maximizes the radial force on the bearings due to gravity. The maximum radial load on the bearings was then determined to be
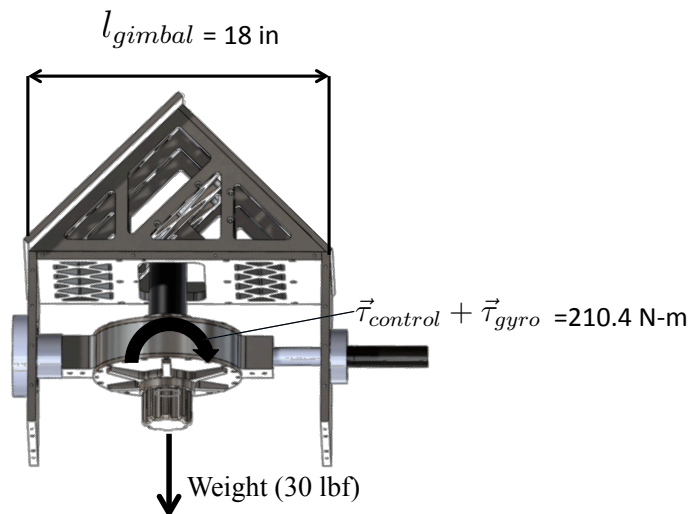
Figure 3.16: Calculation of the Radial Gimbal Bearing Loads

www.manaraa.com

$$c_{r_{max}} = |\vec{\tau}_{control} + \vec{\tau}_{gyro}|/l_{gimbal} + m_{rotor}g/2 \qquad (3.10)$$

where l_{gimbal} is the length between the two gimbal bearings. Because the length between the gimbal bearings is larger than the width between the rotor bearings, the load on the gimbal bearings is less than the load on the rotor bearings. The maximum radial load on the gimbal bearings, per the current CMG and ACSPG design is 114 lb. The same bearing selected for the rotors was selected for use as the gimbal bearing on the motor side of the gimbal shaft. On the slip ring side, the bearing must fit around the slip ring housing, so a Barden 112HCRRDUL angular contact bearing was chosen. The preload on the gimbal bearings is designed to be between 50 and 70 lbs. Preload is applied by tightening down the gimbal bearing caps on each end. Both gimbal bearings are press fit onto their shafts, and slip fit inside the gimbal bearing cap. A shoulder inside the bearing caps carries the preload and ensures that the outer raceway does not move inside the bearing caps. The endplates are made with clearance, so that the bearing outer raceway does not touch the endplate, forcing all the load to be transferred through the bearing caps first.

Table 3.2:   Barden 112HCRRDUL Ball Bearing Specifications[1]

Specification	Value
Contact Angle	15°
Bore Diameter (d)	60.000 mm
Outside Diameter (D)	95.000 mm
Width (B)	36.000 mm
Standard Preload	50
Static Radial Load Capacity (C_0)	7531 lbs.
Basic Dynamic Load Rating (C)	8,767 lbs.
Shield Type	Nitrile Rubber
Lubricant	Grease
Attainable Speed	14,000 rpm
ABEC Rating	7

3.5.3 Gimbal Shaft Design.   The gimbal shaft connects the rotor system to the gimbal support structure and gimbal motor, as shown in Figure 3.15. As such, all loads travel through the gimbal. The initial design for the gimbal shaft was based on the

68

shaft used for SimSat's CMGs, with the same diameter shaft and same basic shaft/rotor housing coupling. FEA results from a loaded gimbal shaft were completed to ensure adequate strength. The initial design, which used a 14 mm shaft to comply with the Baumer G0AMH encoder, was found to be insufficient in strength, with a factor of safety less than 1.5 based on FEA predictions. The shaft size was then increased to 27mm to comply with the Baumer ATD shaft encoder. The coupling was also changed to simplify the system and improve the strength and stiffness. This new size and structure has an estimated factor of safety of 7.9 for the worst loading case, which was deemed sufficient to transfer the load from the rotor to the gimbal structure. On the slip ring side, the shaft couples in the same manner to the rotor housing, but must fit over the slip ring. Because the shaft radius and thickness is larger on the slip ring side, the shaft strength is greater than on the encoder side.

3.5.4 Shaft Encoder Selection. Although the gimbal motor has Hall effect sensors that provide position and speed feedback to the motor controller, increased resolution of the gimbal angle is required. AFIT's SimSat CMG system used a Baumer G0AMH shaft encoder with great success; therefore, this shaft encoder was initially selected for use on the ACSPG CMGs. However, the shaft on the CMG needed to be considerably larger diameter as discussed in Section 3.5.3. than the one used on SimSat's CMGs, which resulted in the selection of a different shaft encoder. The new encoder selected is the Baumer ATD 4B A 4 Y11. This encoder provides 32,768 counts per turn, for an effective resolution of $0.011°$/count. It also communicates using the CANopen network, meaning it will work with the planned ACSPG hardware and software.

3.5.5 Slip Ring Selection. A slip ring on one end of the gimbal shaft allows for full freedom of motion while maintaining the electrical connections necessary to power and control the rotor motor. SimSat used a Mercotac four-conductor slip ring with good results. Because the motors used on the ACSPG CMGs have eight electrical connections to the speed controller, a Mercotac 830 eight-conductor slip ring was chosen.

69

3.5.6 Gimbal Support Structure Design.   The gimbal support structure supports the gimbal shaft and holds the motor while transferring load to the vehicle. SimSat's CMG support structure design served as a starting point for the ACSPG CMG gimbal support structure design; however, a number of significant modifications were made. Because the ACSPG CMGs are so much larger than SimSat's, the support structure was designed to be stronger. To increase the stiffness and load capacity of the support structure, a "cage" was designed to enclose the rotor and gimbal system to ensure bearing and alignment is maintained. The gimbal support structure is designed to rigidly support the gimbal shaft at an inclination angle of $45°$. To create a lightweight but stiff structure, 6061T6 aluminum was selected and lightweighted where possible by removing unnecessary material. Because the Maxon EC 45 motor is extend beyond the radius of the rotor housing, cutouts were strategically placed in the cage to allow for freedom of motion as the rotor changes orientation. Care was taken to ensure that the motor will not meet any obstructions as it passes outside the cage, as long as the ACS is installed as designed. Because the gimbal bearings require a sufficiently hard material to hold the outer raceways, bearing caps, to be made from hardened steel, were designed to hold the bearings. The bearing caps also serve to provide the preload on the gimbal bearings.

3.6 ACSPG ACS Simulation

Simulation was used as a tool to determine the performance of the CMG ACS on the ACSPG. Initially, a simulation was conducted to determine a nominal angular momentum for the CMG rotor, as discussed in Section 3.4.1, using the momentum envelope calculator. This momentum envelope calculator automates the sequence used in Section 2.5. Using this tool, we determined an approximate size for the CMG rotor. The momentum envelope was also calculated each time the design of the rotor was changed. The momentum envelope for the final design for the CMG ACS was then determined to estimate the ACS performance. These results are presented in Section 4.3.

A second simulation tool was used to determine the performance of the CMG ACS on the ACSPG. This MATLAB program simulated the dynamics of the spacecraft and CMGs, as discussed in Section 2.4.5. The simulation takes the ACSPG through a series

of target attitudes, where the spacecraft must align the z-axis of its body frame to target attitude, and hold at each attitude for a set amount of time (generally 10 seconds, but this value is selectable), before moving to the next target attitude. The target attitudes for simulating the ACSPG's ACS were chosen to simulate the full range of motion for the ACSPG, without violating the tilt-limit constraints caused by hardware interference between the tilt limiter and the air-bearing pedestal. The simulation is built to model only the ACS in the 4-CMG pyramid configuration.

There are nine variables that must be known or estimated to run this simulation: five vehicle parameters and four CMG parameters.

- Vehicle Parameters Needed for Simulation : I_{xx}, I_{yy}, I_{zz}, ω_{max}, and α_{max}

- CMG Parameters Needed for Simulation: H_{rotor}, β, ω_{gmax}, and α_{gmax}.

Each time step, the simulation determines the error between the current orientation of the spacecraft and the target orientation. The simulation then uses the MPPSL, discussed in Section 2.5.2, to calculate the ideal torque that should be applied to the ACSPG to achieve the target orientation. The simulation then limits the torque output to ensure that the vehicle's rate limit (ω_{max}) and acceleration limit (α_{max}) are not violated. This is the commanded torque sent to the ACS controller; however, the gimbal has its own rate limit (ω_{gmax}) and acceleration limit (α_{gmax}), which limit the amount of torque available and angular jerk available to control the vehicle. The torque applied to the vehicle, which may be different than the command torque due to the gimbal limits, is called the applied torque. The simulation then feeds the torque input into ODE45, which solves the equations of motion for the ACSPG and determines the new states (vehicle orientation and body rates, CMG gimbal angles) after the control has been applied. Of important note, the simulation uses MPPSL, as discussed in Section 2.5.2, so there is no singularity avoidance capabilities in the simulation. These simulations were used to determine design performance and inform potential design changes to the ACSPG or the CMGs. Results of the simulations were then analyzed to determine whether the design of the ACS met performance goals. Analysis of the results is discussed in Section 4.4.

3.7 CMG Prototype Testing

3.7.1 Rotor Moment of Inertia and Mass Measurement. To determine the angular momentum capability of the CMG, the rotor MOI was measured using AFIT's XR250 MOI measurement device. The MOI of both the spin axis and the gimbal axis were measured. The mass of the rotor was measured by setting the rotor onto two Scout Pro scales, and the measurement from each scale was added to give a total rotor mass. Two scales were used because the rotor's mass was beyond the measurable range of the scale, as the range of the Scout Pro is only 0 to 6 kg, and the mass of the rotor is designed to be 10.08 kg. Figure **??** and Figure 3.17 show the MOI test setup and mass measurement test setup, respectively. The mass of the rotor is 9.90 kg. The rotor's MOI about its spin axis is 0.05877 kg-m^2, while its MOI about its gimbal axis is 0.03089 kg-m^2.
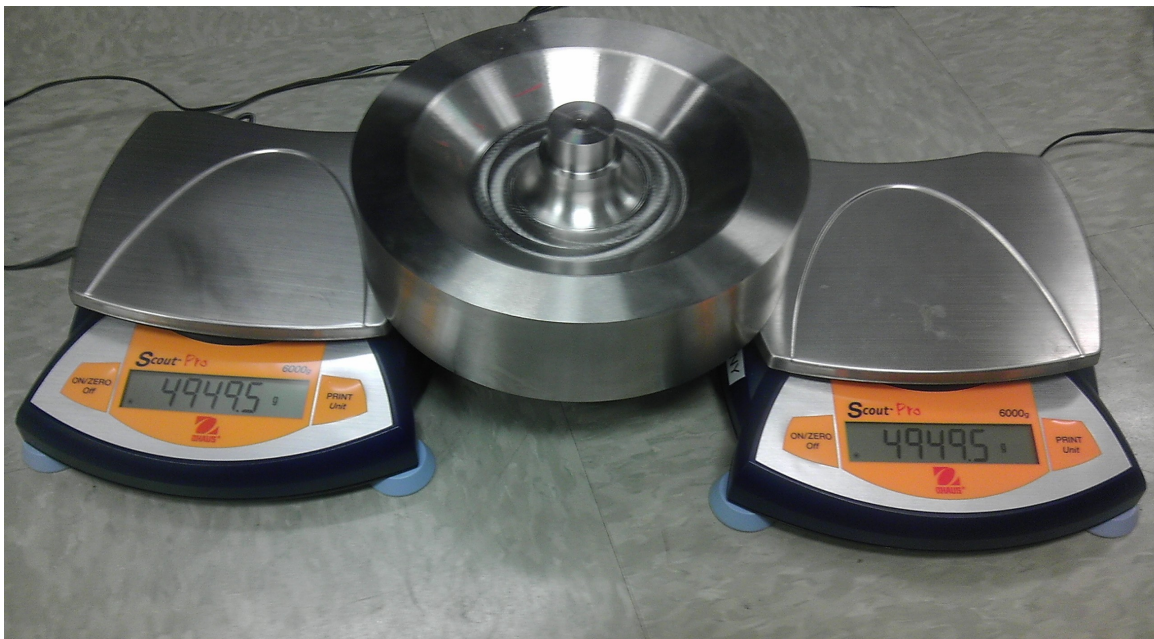

Figure 3.17:   Rotor Mass Test Setup

3.8 Summary

Chapter III detailed the framework that was developed for the design of CMGs and how it was applied to the design of the CMG ACS for the ACSPG. This chapter

72

also discussed simulation and test methods for CMGs, and how simulation and testing affect the design of the CMG ACS.

IV. Results and Analysis

4.1 Introduction

Chapter IV begins with a comparison of the ACSPG CMG design to the Honeywell M50 CMG in Section 4.2. The following sections present the results and accompanying analysis of simulation and testing of the design of the CMG ACS for the ACSPG. Additional figures and results are presented in Appendix B.

4.2 A Comparison of the Honeywell M50 CMG and the CMG designed for use on the ACSPG

Table 4.1 presents the design parameters of the Honeywell M50 CMG with the CMGs designed for the ACSPG. The ACSPG CMGs perform comparably or favorably to the Honeywell M50 by most metrics. Because the CMGs for the ACSPG are for lab use, they are an estimated 39 kg, versus 28 kg for the M50, which is designed for use on spacecraft.

Table 4.1: Performance comparison between Honeywell M50, ACSPG CMGs, and AFIT SimSat CMGs

Performance Item	Honeywell M50 [40]	ACSPG CMG	AFIT SimSat CMG [3]
Angular Momentum	25-75 N-m-s	18.5-52.3 (36.9 Nom) N-m-s	0.43 N-m-s
Rotor Speed	4500-6500 rpm	3000-8500 (6000 Nom) rpm	3000 rpm
Gimbal Rotation Range	360°	360°	360°
Gimbal Acceleration	3 rad/s^2	5 rad/s^2	Not Specified
Gimbal Indication Accuracy	±1°	±0.011°	±0.044°
Full Output Torque	75 N-m	92 N-m	0.06744 N-m
Mass	28 kg	39 kg	5 kg (approx)

4.3 Maximum Theoretical Performance Results

As mentioned earlier, the CMG ACS designed for the ACSPG can be configured in three variations: 4-unit pyramid, 4-unit rooftop, and 6-unit rooftop. The 4-unit pyramid configuration uses CMGs 1, 2, 3, and 4, whereas the 4-unit rooftop configuration uses CMGs 1, 3, 5, and 6, as shown in Figure 4.1. The 6-unit rooftop configuration uses CMGs 1, 3, 5, and 6 as shown in Figure 4.1, and CMGs 2 and 4 have to be removed and rotated 90° counterclockwise for this configuration. This rotation aligns CMG 2 to

74

be parallel with CMGs 3 and 6, and CMG 4 to be parallel to CMGs 1 and 5. Note that all configurations have six CMGs present on the underside of the ACSPG, the only difference between each configuration is which CMGs are active and their alignment. Each configuration's momentum envelope was calculated to determine the configuration's theoretical maximum angular rates to determine if the design meets performance goals. Figure 4.2 shows the external singularity surfaces for each configuration.
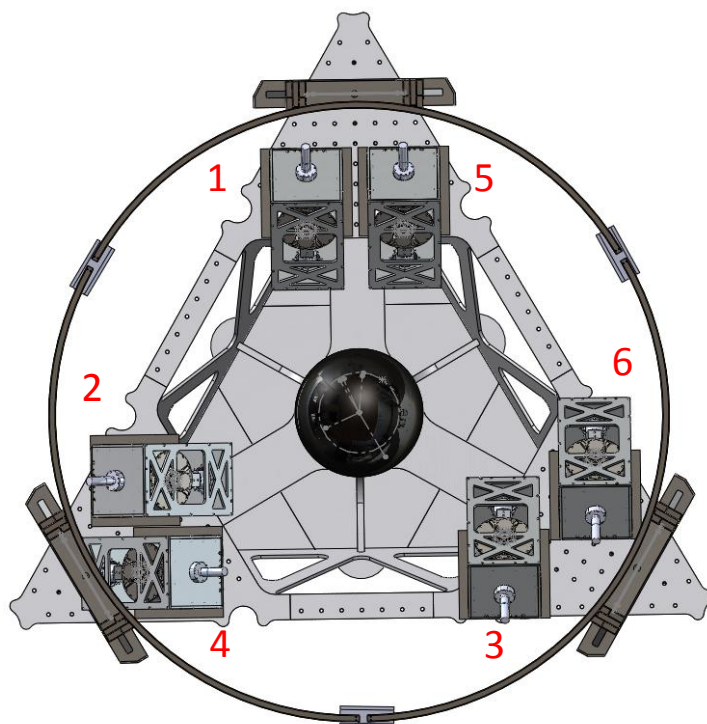
Figure 4.1:   Configuration of the CMGs on the ACSPG

Equation 4.1 determines the maximum achievable angular rates for a spacecraft based on its momentum envelope, where ϕ, θ, and ψ are the roll, pitch, and yaw rates, respectively.
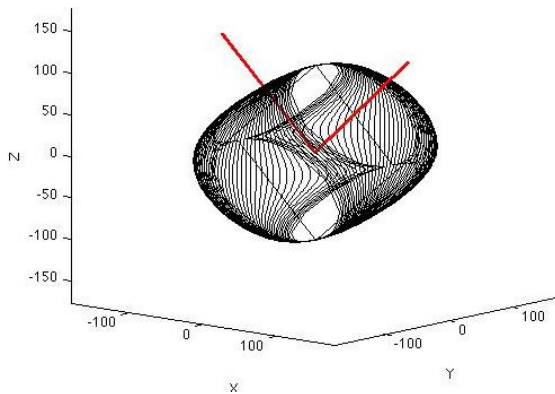
$$\phi_{max} = (h_{x_{max}} - h_{x_{min}})/I_{xx} \tag{4.1a}$$

$$\theta_{max} = (h_{y_{max}} - h_{y_{min}})/I_{yy} \tag{4.1b}$$
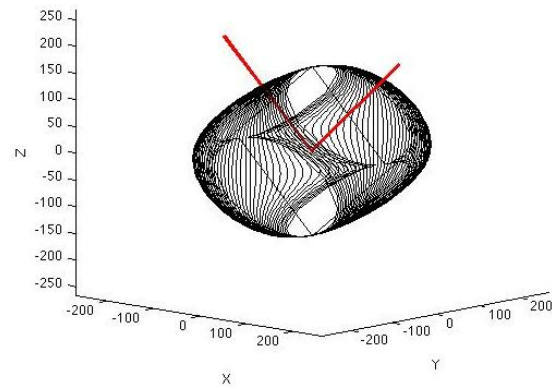
$$\psi_{max} = (h_{z_{max}} - h_{z_{min}})/I_{zz} \tag{4.1c}$$

75
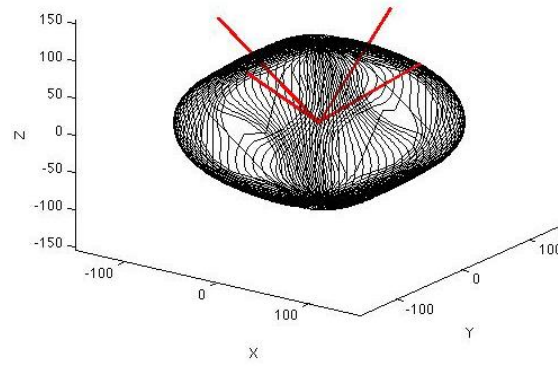
(a) 4-unit pyramid

(b) 4-unit rooftop

(c) 6-unit rooftop

Figure 4.2: Singularity Surfaces for the ACSPG's ACS when operating in varying configurations

Estimating the principal MOIs of the ACSPG as [664.5, 634.1, 686.1], as discussed in Section 2.2, given the correct gimbal alignment, the ACSPGs could theoretically start from rest and reach ϕ_{max}, θ_{max}, or ψ_{max} under CMG control. Table 4.2 details the max theoretical achievable angular rates each configuration can achieve when operational.

Table 4.2: Momentum envelope and angular rate bounds for varying configurations of the ACS on the ACSPG

Configuration	h_x	h_y	h_z	ϕ_{max}	θ_{max}	ψ_{max}
4-Unit Pyramid	±126 N-m-s	±126 N-m-s	±104 N-m-s	21.7°/s	22.8°/s	17.4°/s
4-Unit Rooftop	±104 N-m-s	±148 N-m-s	±104 N-m-s	18.1°/s	26.8°/s	17.5°/s
6-Unit Rooftop	±157 N-m-s	±221 N-m-s	±157 N-m-s	27.0°/s	40.0°/s	26.1°/s

76

The max theoretical acceleration that can be achieved using the ACS is a function of the CMG configuration and β angle of the CMGs. Recall that the torque produced by a CMG is

$$\vec{\tau} = \dot{\vec{h}} = \vec{\omega}_{gimbal} \times \vec{h}_{rotor}. \tag{4.2}$$

This torque can only be applied in the rotor's y-z-plane, as shown in Figure 2.15. The implication of this fact is that, given the correct gimbal alignment, CMGs 1, 3, 5, and 6, can provide their maximum torque to the y-axis of the ACSPG's body frame, or $1/\sqrt{2}$ of their maximum torque to the x-axis and z-axis of the ACSPG's body frame. CMGs 2 and 4 can provide their maximum torque to the x-axis of the body frame, or $1/\sqrt{2}$ of their maximum torque to the y-axis and z-axis of the ACSPG's body frame. Estimating the principal MOIs of the ACSPG as [664.5, 634.1, 686.1], given the correct gimbal alignment, the ACSPGs could theoretically reach $\alpha_{x_{max}}$, $\alpha_{y_{max}}$, or $\alpha_{z_{max}}$. Table 4.3 details the max theoretical achievable angular rates each configuration can achieve when operational. All values are in Table 4.3 are calculated with a max gimbal rate of 2.5 rad/s. If the max gimbal rate is changed, the values in Table 4.3 scale linearly.

Table 4.3:   Available torque and angular acceleration bounds for varying configurations of the ACS on the ACSPG

Configuration	τ_x	τ_y	τ_z	$\alpha_{x_{max}}$	$\alpha_{y_{max}}$	$\alpha_{z_{max}}$
4-Unit Pyramid	±315 N-m	±315 N-m	±261 N-m	$27.2°/\text{s}$	$28.5°/\text{s}^2$	$21.8°/\text{s}^2$
4-Unit Rooftop	±261 N-m	±369 N-m	±261 N-m	$22.5°/\text{s}$	$33.36°/\text{s}^2$	$21.8°/\text{s}^2$
6-Unit Rooftop	±392 N-m	±222 N-m	±392 N-m	$33.7°/\text{s}$	$50.0°/\text{s}^2$	$32.7°/\text{s}^2$

4.4   ACS Simulation Results

The design of the CMG ACS was simulated using MATLAB to determine if the design would meet performance goals in a practical application. The simulation ran the ACSPG through a series of target attitudes, where the ACSPG's z-axis in its body frame must be aligned to a target vector for 10 seconds before moving to the next target attitude. The target vectors are listed in Table 4.4. Figure 4.3 shows the ACSPG in these target orientations.

77

Table 4.4: Simulation Target Vectors

Target	x	y	z
1	1	1	3
2	1	−1	3
3	−1	−1	3
4	−1	1	3
5	1	−1	3
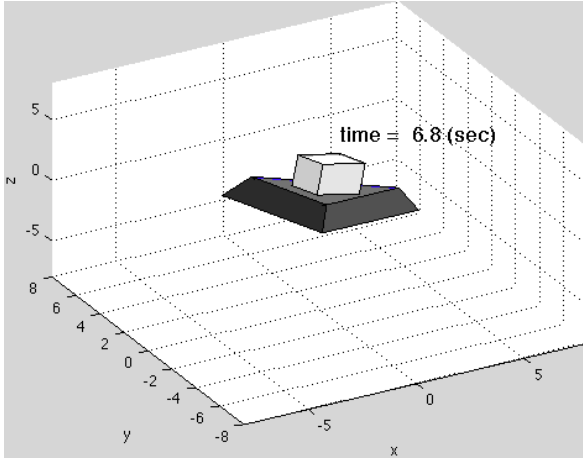
(a) Target 1 Orientation
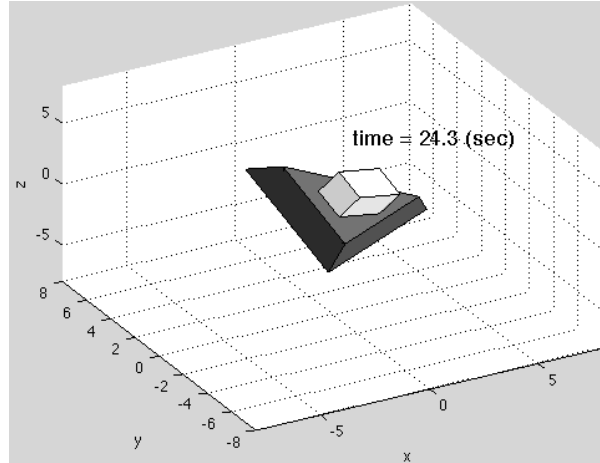
(b) Target 2 and 5 Orientation
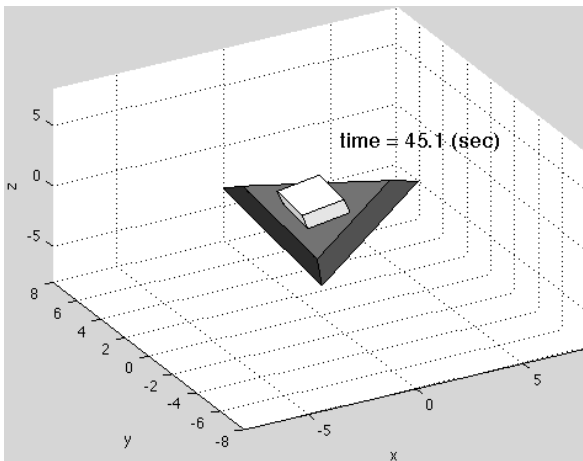
(c) Target 3 Orientation
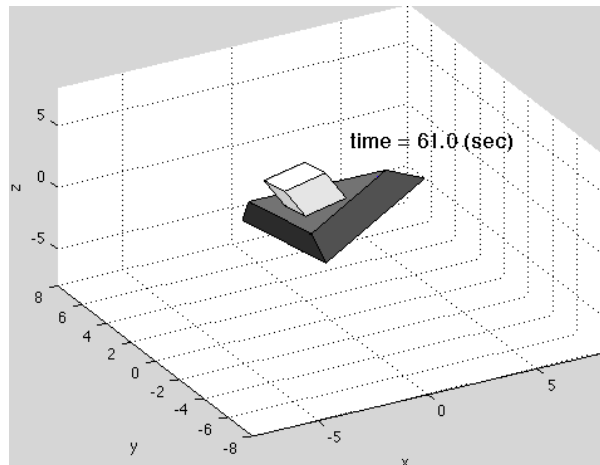
(d) Target 4 Orientation

Figure 4.3: ACSPG in Target Orientations

The configuration for all simulations presented in this discussion is the 4-unit pyramid CMG ACS, with all 6 CMGs present, but two not operating. This configuration was chosen for simulation because the pyramid configuration has a lower level of performance

78

than either the 4 or 6-CMG rooftop configurations. If satisfactory performance could be achieved using the pyramid configuration, it would also be achieved using the rooftop configurations. Table 5 lists the relevent variables used in this simulation. Figure 4.4 presents the values of the quaternions of the spacecraft during the simulation. Figure 4.5 shows the angular rates for the ACSPG during the simulation. This figure shows that the ACS can meet the performance requirement of $10°/s$ about the vehicle's roll and pitch axes.

Table 4.5:   Simulation Parameters

Vehicle Parameters	I_{xx}	I_{yy}	I_{zz}	ω_{max}	α_{max}
Value	664.5 kg-m^2	634.1 kg-m^2	686.1 kg-m^2	$10°/s$	$10°/s^2$

CMG Parameters	H_{rotor}	β	ω_{gmax}	α_{gmax}
Value	36.93 N-m-s	$45°$	2.5 rad/s	5 rad/s^2

Figure 4.6 gives the gimbal orientation throughout the simulation. Note that when the vehicle transfers from target attitude 1 to target attitude 2 at approximately the 14-second point, gimbal number 1 goes through a large change in orientation in a short period. This behavior signals that the ACS is at or approaching a singularity. Because the simulation uses MPPSL, there is no singularity avoidance in the simulation. This information was brought up to the sponsor, and because they plan on testing primarily using steering laws that implement singularity avoidance techniques, such as a modified GISL known as Hybrid Steering Logic (HSL), they were not concerned by this result.
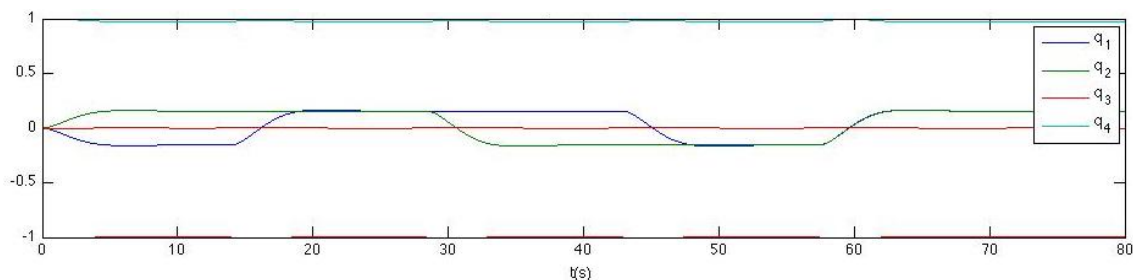

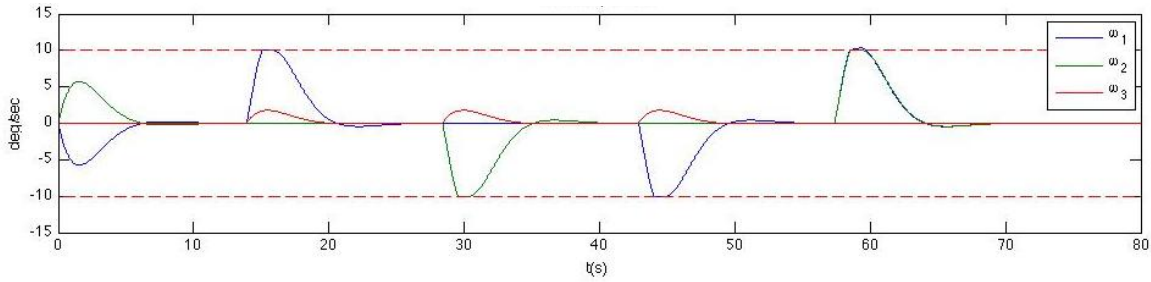Figure 4.4:   Quaternions v. Time

79

Figure 4.5:   Vehicle Angular Rates v. Time - Dashed line depicts max s/c slew rate
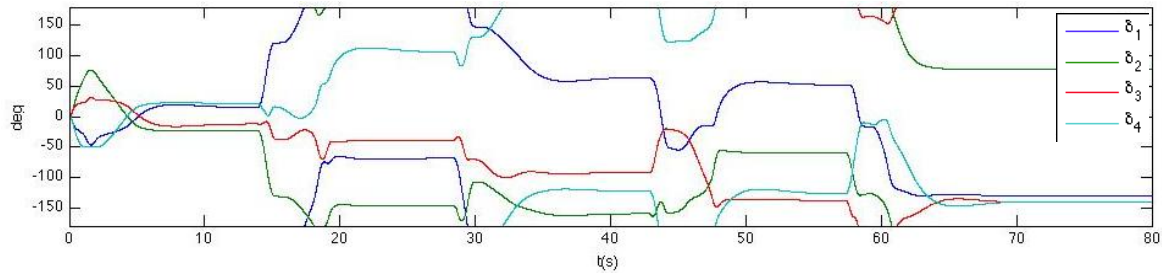

Figure 4.6:   Gimbal Angle v. Time

Figure 4.7 shows the commanded and actual gimbal rates throughout the simulation. The large spikes in the commanded gimbal rates show that the ACS is near a singularity. Near a singularity, the controller wants to divide by very small numbers, resulting in large spikes in the commanded gimbal rates. Figure 4.8 shows the activity of gimbal 1 near the 15-second mark. At 13.9 seconds, the target attitude is changed to align to the second target vector. The controller then determines the required torque and gimbal rates to make this happen. In the simulation, the controller requests rates that cannot be achieved by the actuators, therefore the actual rate is limited. The actual gimbal rate between 13.9 seconds and 14.4 seconds is shown in Figure 4.8. At 14.4 seconds, the gimbal reaches its maximum angular rate, and maintains that rate until the 14.7-second mark, when the controller begins commanding a lower gimbal rate. This happens a number of times throughout the simulation; Figure 4.8 is just one example.

The implication of limiting the gimbal rates and accelerations is that there will be a difference between the commanded torque and applied torque, as shown in Figure 4.9. In essence, limiting the gimbal acceleration limits the rate of change of torque, or
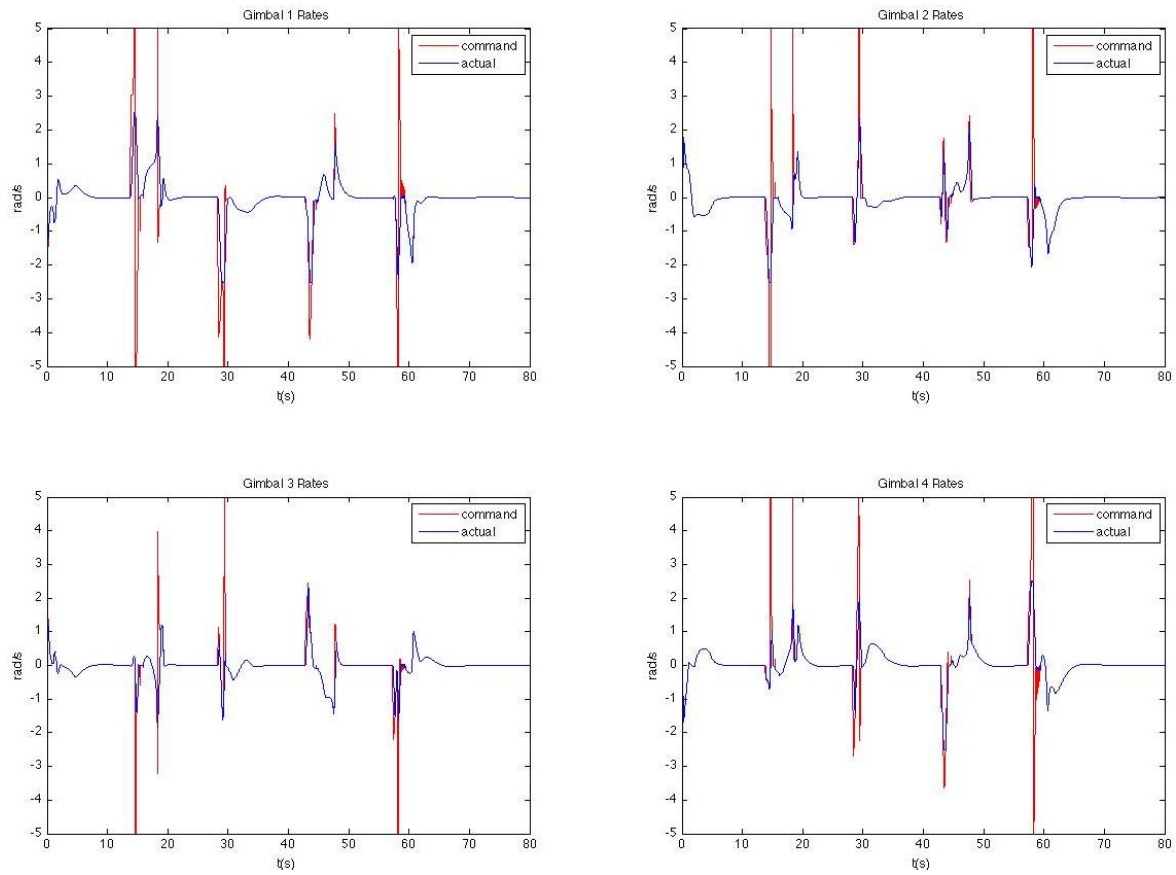
80

Figure 4.7:   Gimbal Rate v. Time
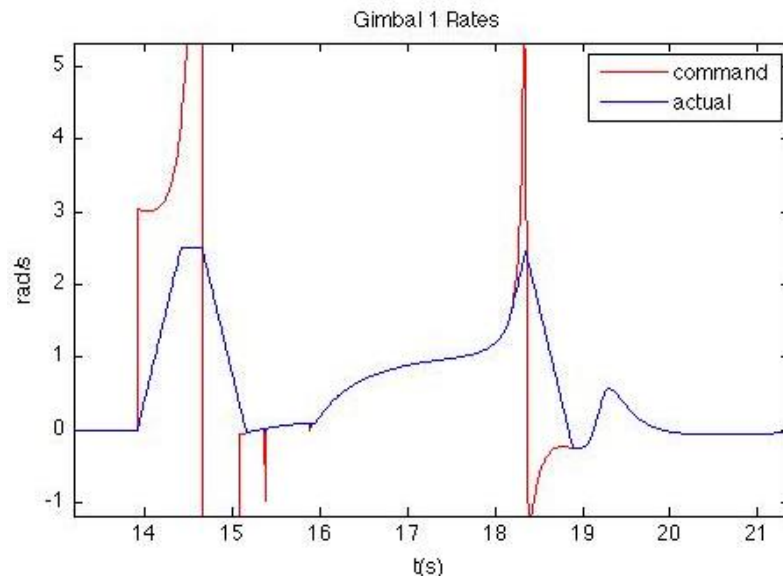
Figure 4.8:   Gimbal Angle v. Time

81

angular jerk, available to the ACS. This behavior is most pronounced when we look at the x-axis torque at approximately the 14-second mark, shown in Figure 4.10. At the 13.9-second mark, the target attitude is changed from the first to the second target vector. The controller then calculates an ideal torque, shown in blue, to align itself to the new target orientation. The commanded torque, shown in green, is limited to ensure that the vehicle's max acceleration rate is not exceeded. The applied torque, shown in red, significantly lags behind the commanded torque due to the gimbal acceleration and rate limits. The ACS likely approaches a singularity near the 14.4-second mark, evidenced by the reversal in direction of the applied torque and the large change in gimbal angle in CMG 1, shown in blue in Figure 4.6. At approximately the 15.1-second mark in the simulation, the vehicle achieves a maximum angular rate, the rate limiter is exercised, and the commanded torque is zero.

Figure 4.9:   Torque v. Time

Figure 4.10:   Torque v. Time

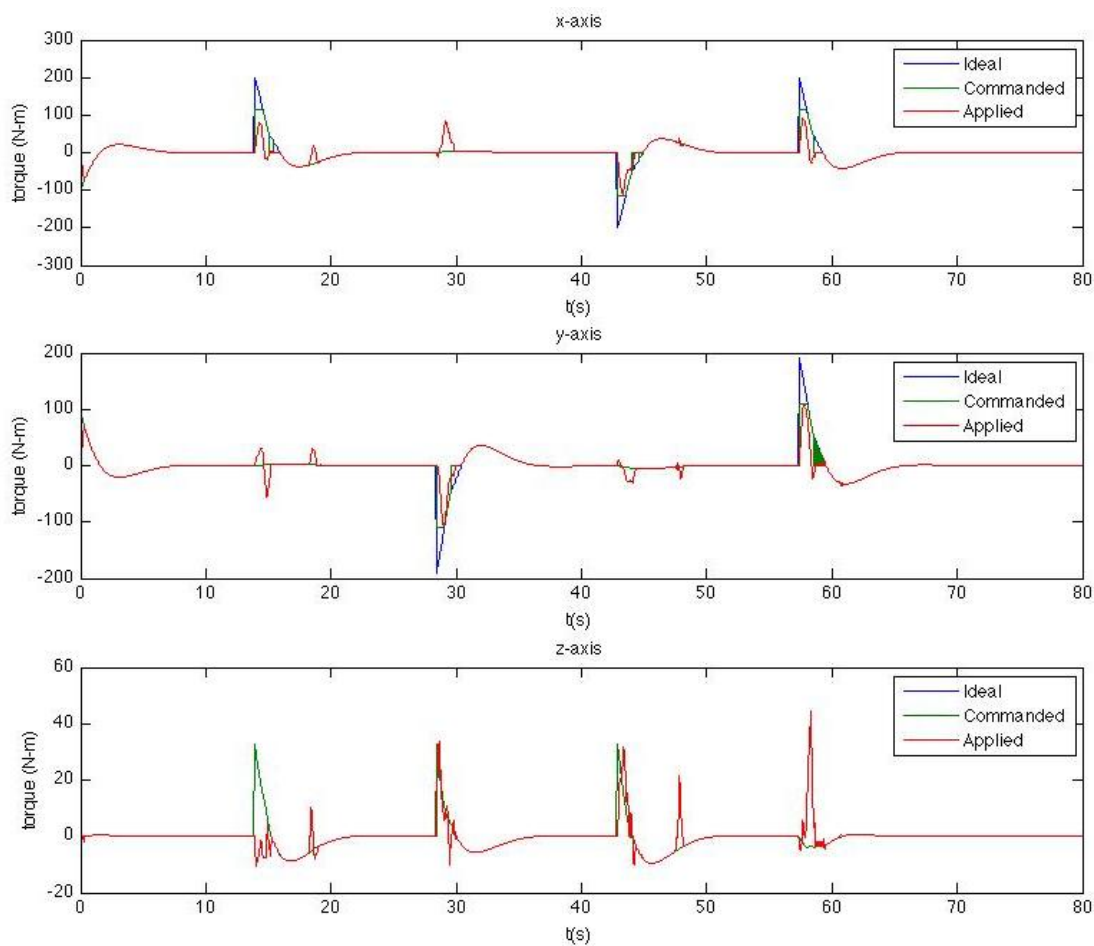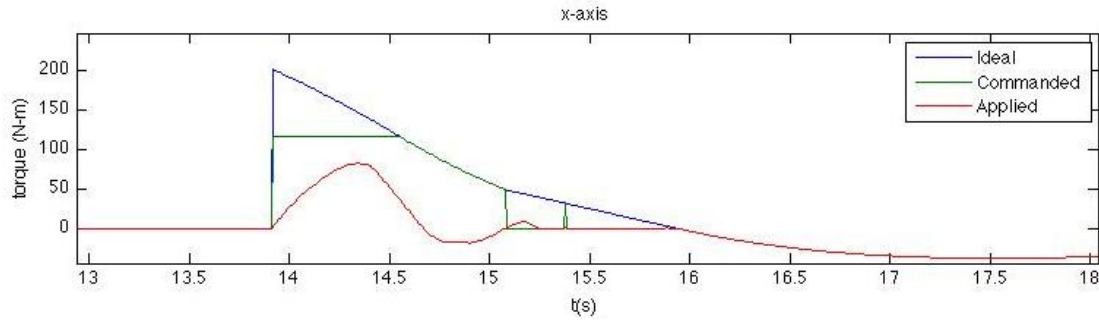A number of simulations were conducted for different configurations. These results are presented in Appendix B. With the simulation data, we were able to make a number of conclusions. First, the design of the CMG ACS meets or exceeds the performance requirements that were provided by the sponsor: The ACS will be able to provide the required amount of torque to meet the acceleration requirement of $10°/s^2$ about any axis, and the ACS will be able to transfer the required amount of momentum to the vehicle to meet the angular rate requirement of $10°/s$ about any axis. However, we must qualify these statements: in practical application, external torque may cause ACS to build up or store angular momentum, which will reduce its performance, because the ACS will near saturation. External torque devices like fans, cold gas thrusters, or another form of providing external torque for angular momentum dumping will be necessary for the CMG ACS to continuously maintain high performance over long periods of time or many maneuvers. Second, the simulation shows that the ACS may be prone to singularities if the MPPSL is used, especially if the vehicle angular rate is to achieve $10°/s$. Figures 4.11 and 4.12 shows the results of the simulation if ACSPG's max angular rate and acceleration requirements are changed to $5°/s$ and $5°/s^2$. Note that the gimbal behavior is much less erratic when the performance requirements are reduced in this way. Five degrees per second is still more agile than most current satellites.

4.5   Evaluation of the CMG ACS Design Process

In this research effort, the hardware for a CMG ACS was designed, simulated, built, and tested. The results of the simulation and testing show that the design, once

83
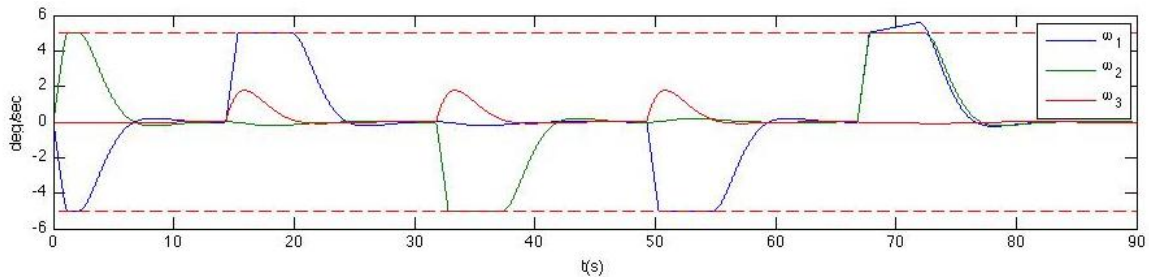
Figure 4.11:   Vehicle Angular Rates v. Time, Lowered Performance Requirements from $10 \rightarrow 5°/\text{s}$ and $10 \rightarrow 5°/\text{s}^2$
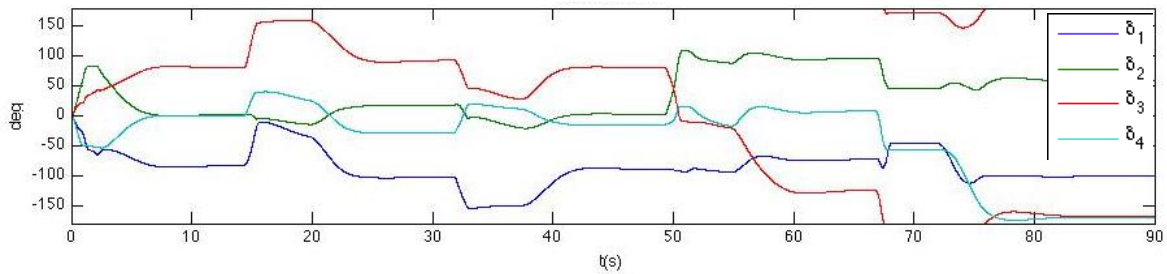
Figure 4.12:   Gimbal Angles v. Time, Lowered Performance Requirements from $10 \rightarrow 5°/\text{s}$ and $10 \rightarrow 5°/\text{s}^2$

operational, will meet or exceed the sponsor's listed performance requirements. Since we were able to successfully develop the CMG ACS for the ACSPG, there is at least a basic level of usefulness in the design process that was developed in this effort. Although an attempt was made to be as thorough as possible when developing the CMG and CMG-based ACS design process, the design method can still be improved. Instead, this design process should be considered a first attempt, as there is likely considerable room to improve its robustness and depth.

4.6   Summary

The data presented in Chapter IV show that the design of the CMG ACS for the ACSPG will meet the performance requirements listed by the program sponsor. Furthermore, the successful development of the CMG design and test of the CMG prototype validates the design method developed in Section 3.2.

84

V.   Conclusions and Recommendations

5.1   Conclusions

The primary research objectives of this effort were to develop a methodology for the design, development, and testing of control moment gyroscope (CMG) attitude control subsystems (ACSs). This methodology was then used to design a CMG ACS for the Attitude Control Subsystem Proving Ground (ACSPG), as discussed in Chapter III. The secondary objectives were to build and test a prototype CMG. The final result of this research is a much improved methodology for the design of CMG CMGs with a correlated increase in the capability to design CMGs at AFIT, a design for the CMG portion of the ACS for the ACSPG, and a prototype CMG that can be installed or modified to be installed for use on the ACSPG. Actually building the CMG prototype was fundamental to the design, build, test process, because the experience of building a high-quality CMG has turned into the capability of designing and building high-quality CMGs, and building the prototype CMG also greatly influenced the design methodology that was developed for this research effort.

The thesis also addressed the system dynamics and estimated the performance characteristics for the ACSPG and CMGs. The design of the CMG ACS for the ACSPG meets the performance requirements provided by the sponsor, and listed in Section 1.2.

Throughout this research effort, we also developed some very useful capabilities, including rotor balancing capabilities, bearing fitting capabilities, and general machining capabilities.

Finally, a list of best practices was produced, which can be found in Appendix A.

5.2   Recommendations for Future Development

5.2.1   Design Methodology Improvements.   The design methodology for the design and development of CMGs that was developed for this research effort was the first attempt at developing this type of design methodology at AFIT. While an attempt was made to make the design methodology as robust as possible, it is not intended to be the definitive roadmap for CMG design; instead, it is intended to point the CMG designer in the correct direction. There is undoubtedly room to improve this design methodology,

as other CMG designers may encounter problems that we did not encounter, and may need to add or adjust to the methodology accordingly.

5.2.2 *Further CMG Tests.* Due to time constraints, only a very limited number of hardware tests were conducted with the prototype CMG. The design of the CMG can be tested further in a number of ways. Vibration tests on the gimbal support structure should be conducted to ensure that the structure does not vibrate at a frequency that is resonant with the induced rotor vibrations. Tuning of the rotor speed and rotor motor while measuring their induced vibrations should be done to characterize the vibrations of the motor and rotor. Characterizing the vibrations of the rotor and motor together will allow a future researcher to pick the precise rotor speed to minimize vibrations.

Once assembled, a checkout of each of the subsystems should be completed to ensure the CMG works as designed. This testing should include freedom of motion testing, gimbal rate and acceleration testing, shaft encoder testing, assembly structural soundness testing (a simple test to make sure the assembly shouldn't fall apart when handled), and rotor speed control testing. All of these tests should be performed separate from one another. A second round of balancing should also be conducted after the CMG is assembled if possible.

5.2.3 *ACSPG CMG Design Improvements.* One possible way to improve the design of the CMG would be to move the optical encoder to the other side of the end cap. This would shorten the gimbal shaft on this end, significantly improving the stiffness of the gimbal support structure. Other possible ways to improve the gimbal support structure include placing support triangles near the end to decrease the gimbal support structure's propensity to vibrate at low frequencies.

One aspect of the design that requires additional work is the adapter between the ACSPG and the CMGs. An adapter was designed for this purpose, but the design of the CMG was continually changing, and the adapter as designed did not match the revised design of the CMGs. Now that the design of the CMG is more or less finalized, the adapter design can be revised to match the design of the CMGs and ACSPG. The design of the adapter should also include a vibration isolation system. The vibration

86

isolation system may go between the CMG and adapter, or between the adapter and the ACSPG, with a preference for the latter for the sake of simplicity.

If desired, the performance of the CMG ACS can be improved a number of ways. The angular momentum storage of the CMG can be increased by increasing the rotor speed or increasing the rotor's MOI. The rotor speed can be increased to from 6000 rpm to 8500 rpm, which would increase the angular momentum storage by 41.6%. The rotor design could also be adjusted to a denser material, such as carbide or tungsten-copper alloy. Tungsten-copper alloys offer up to twice the density of stainless steel, are machinable, and should be able to tolerate the stress caused by high angular rates. A drawback of using a denser rotor material is that the denser material would make the rotor twice as heavy and the CMG approximately 20% heavier.

The performance of the ACSPG can also be improved by adjusting its design. Removing the tilt limiter from the ACSPG reduces its mass by 144 kg and its principle MOI by [373, 373, 282] kg-m^2 about its x, y, and z axes, respectively. To maintain safety, a new tilt limiter can be designed that would attach to the air-bearing's pedestal. This redesign would also free up more room along the underside of the ACSPG to place the CMGs. The CMGs could then be placed slightly farther from the center of the ACSPG, which would increase the rotational freedom in the ACSPG's pitch and roll axes.

5.2.4   Future CMG development for the ACSPG.   The next step is the development at least five CMGs to complete the set of 6, including mounting adapters, for the ACSPG's ACS. Now that one CMG has been completed, this process should be considerably less difficult.

5.2.5   Research Areas.   Once the CMGs are installed on the ACSPG, they can be used to test novel steering algorithms, such as hybrid steering logic, or other modified generalized inverse steering laws.

Appendices

Appendix A. Lessons Learned and Best Practices

This section presents a list of thoughts, lessons learned, and best practices.

1. Develop an organization system for file naming and organizing early, especially if multiple people are allowed access to the same files. Once your organization system is in place, write a readme to document your file organization and naming systems.

2. Precise pieces require very tight tolerances. High quality bearings are worthless if they are not fitted properly. To get an interference fit on our bearings, we cooled the rotor by placing it outside on a winter morning, heated the bearings, then slid the bearing right on. We then left both outside until their temperatures equalized. Once the temperature equalized, we had an interference fit. Meanwhile, the rotor housing side panels had been heating. These were then fit over the outer raceway of the now cold rotor bearings. One side panel is an interference fit, while the other is a push fit. This was recommended by the Barden bearing engineers.

3. The gimbal bearings were interference fit onto the gimbal shafts in the same manner (chilling and heating). Because the dynamic load on the gimbal bearings is so much less, their outer raceways are supported only by a slip fit in the bearing caps. They are then held firmly in place by applying the preload to the bearings by tightening down the bearing caps. The bearing caps contain a lip that contacts the outer raceway of the bearing and holds the bearing in place. This lip extends a few thousandths farther than the outside of the bearing cap. When the caps are tightened down, the extra length on the lip forces the entire gimbal assembly in compression and holds the bearing in place. This technique was also used with the motor mount and counterweight mount to apply preload to the rotor bearings.

4. In practice, every sharp corner is going to be filleted to some amount. In some cases, it makes sense to include the fillet in the CAD, as this may influence what tool a machinist uses; however, fillets can be hard to deal with when modeling using FEA. To make it easier to model in FEA, extremely small fillets should be taken out of the CAD model. If possible, all fillets should be included in the as-built model.

5. A designer is a generalist. Going into the design, I understood the equations of motion of CMGs and that was about it. I knew next to nothing about electric motors, ball bearings, tolerancing and fitting, materials, or balancing. For help in these areas, where I had only general knowledge, we looked to experts. Receiving expert help made all the difference and made the design much, much better.

Appendix B. Supplemental Results Figures

Appendix B contains supplemental results from the tests presented in Chapter IV.

2.1 Supplemental Simulation Results

Table 1: Simulation 1 Parameters

Vehicle Parameters	I_{xx}	I_{yy}	I_{zz}	ω_{max}	α_{max}
Value	664.5 kg-m^2	634.1 kg-m^2	686.1 kg-m^2	10°/s	10°/s^2

CMG Parameters	H_{rotor}	β	ω_{gmax}	α_{gmax}
Value	36.93 N-m-s	45°	2.5 rad/s	5 rad/s^2

Table 2: Simulation 2 Parameters

Vehicle Parameters	I_{xx}	I_{yy}	I_{zz}	ω_{max}	α_{max}
Value	664.5 kg-m^2	634.1 kg-m^2	686.1 kg-m^2	10°/s	10°/s^2

CMG Parameters	H_{rotor}	β	ω_{gmax}	α_{gmax}
Value	36.93 N-m-s	45°	5 rad/s	10 rad/s^2

Table 3: Simulation 3 Parameters

Vehicle Parameters	I_{xx}	I_{yy}	I_{zz}	ω_{max}	α_{max}
Value	664.5 kg-m^2	634.1 kg-m^2	686.1 kg-m^2	5°/s	5°/s^2

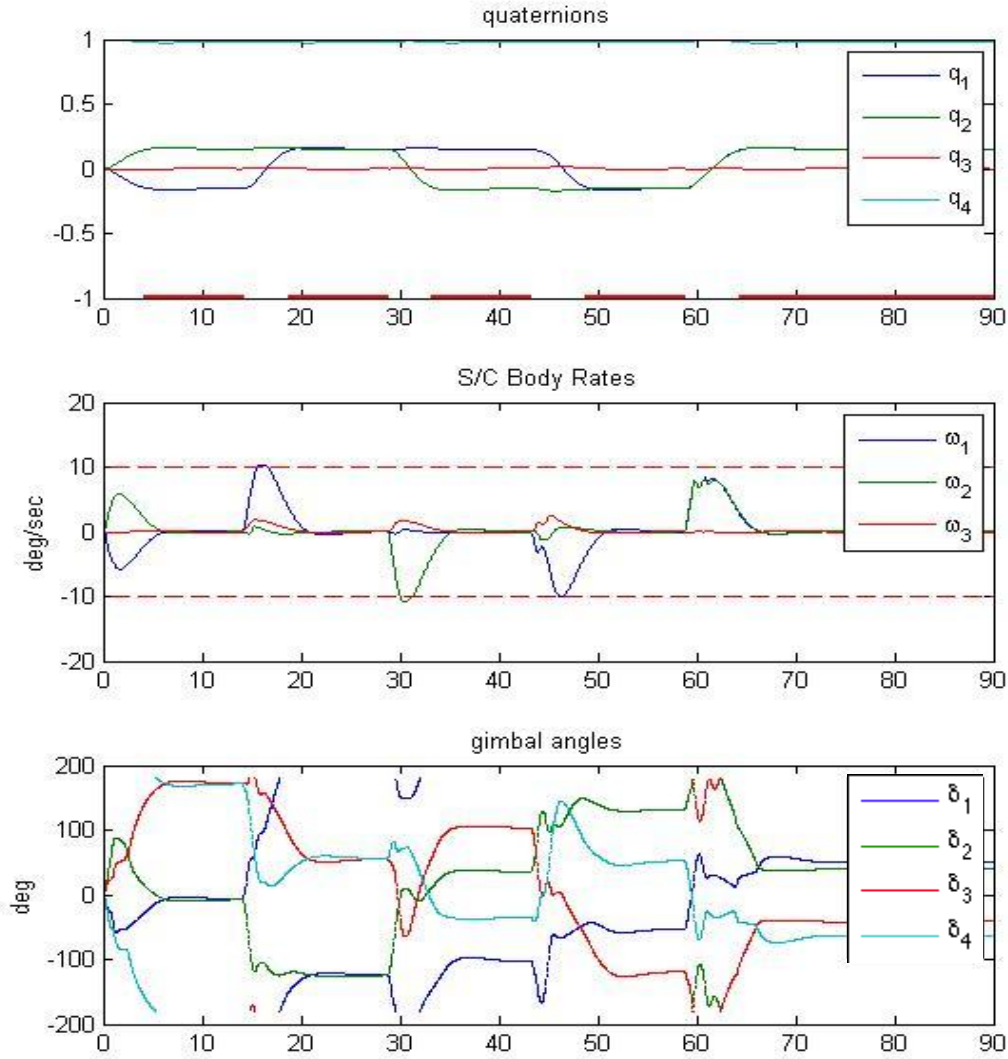| CMG Parameters	H_{rotor}	β	ω_{gmax}	α_{gmax}
Value	36.93 N-m-s	45°	2.5 rad/s	5 rad/s^2

Figure 1:   Simulation 1 Orientation, Rates, and Gimbal Positions

Table 4:   Simulation 4 Parameters

Vehicle Parameters	I_{xx}	I_{yy}	I_{zz}	ω_{max}	α_{max}
Value	450 kg-m^2	450 kg-m^2	750 kg-m^2	5°/s	5°/s^2

CMG Parameters	H_{rotor}	β	ω_{gmax}	α_{gmax}
Value	36.93 N-m-s	45°	2.5 rad/s	5 rad/s^2

92
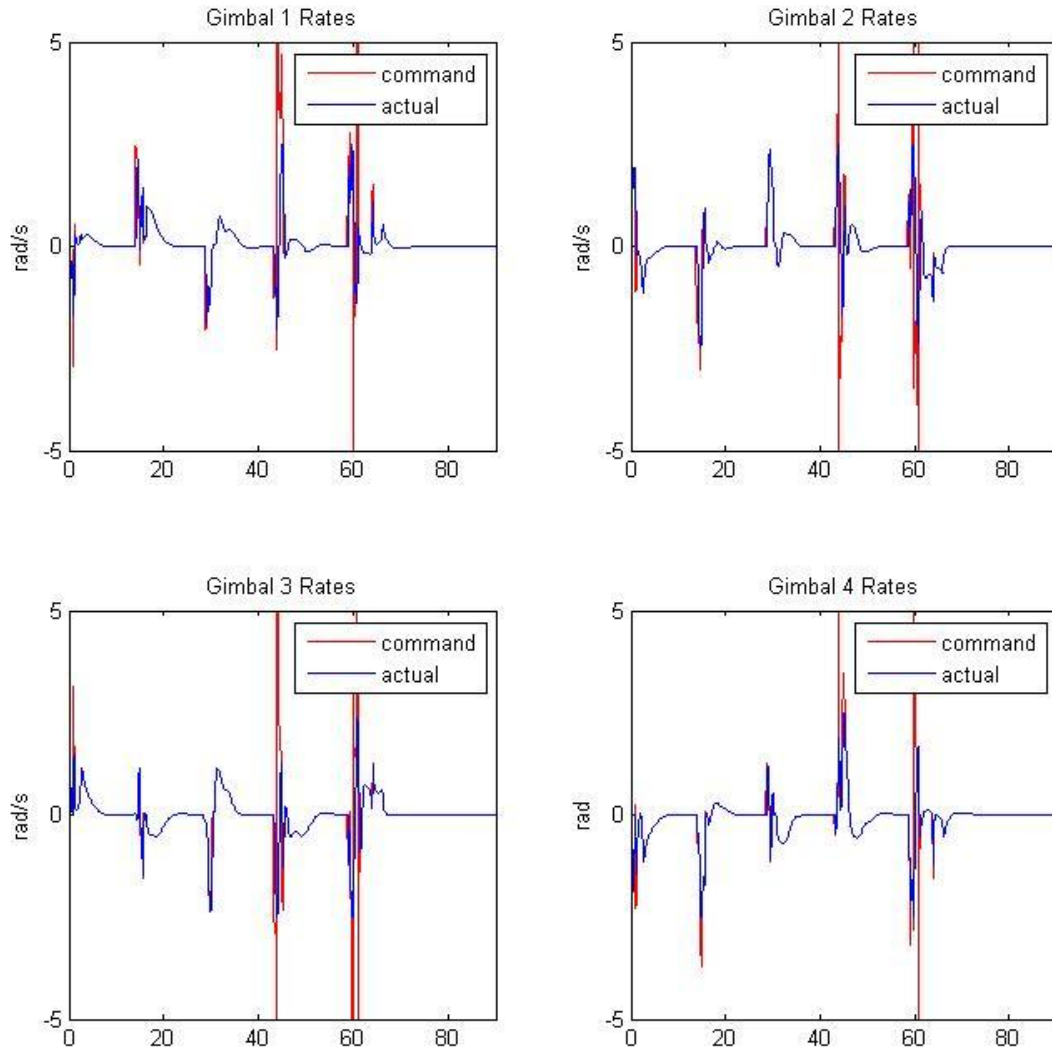
Figure 2:   Simulation 1 Gimbal Rates

Table 5:   Simulation 5 Parameters

Vehicle Parameters	I_{xx}	I_{yy}	I_{zz}	ω_{max}	α_{max}
Value	450 kg-m^2	450 kg-m^2	750 kg-m^2	$10°/\text{s}$	$10°/\text{s}^2$

CMG Parameters	H_{rotor}	β	ω_{gmax}	α_{gmax}	
Value	36.93 N-m-s	$45°$	2.5 rad/s	5 rad/s^2	

93
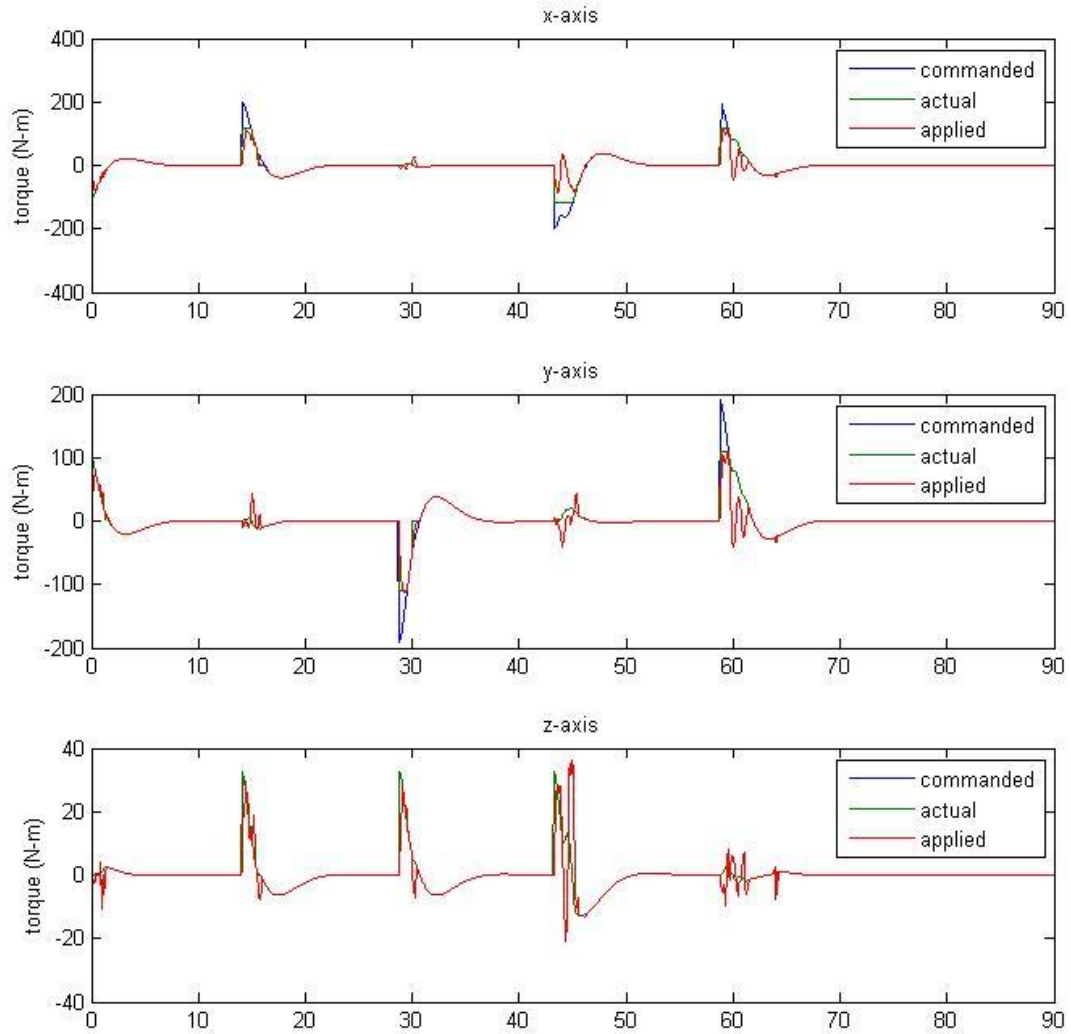
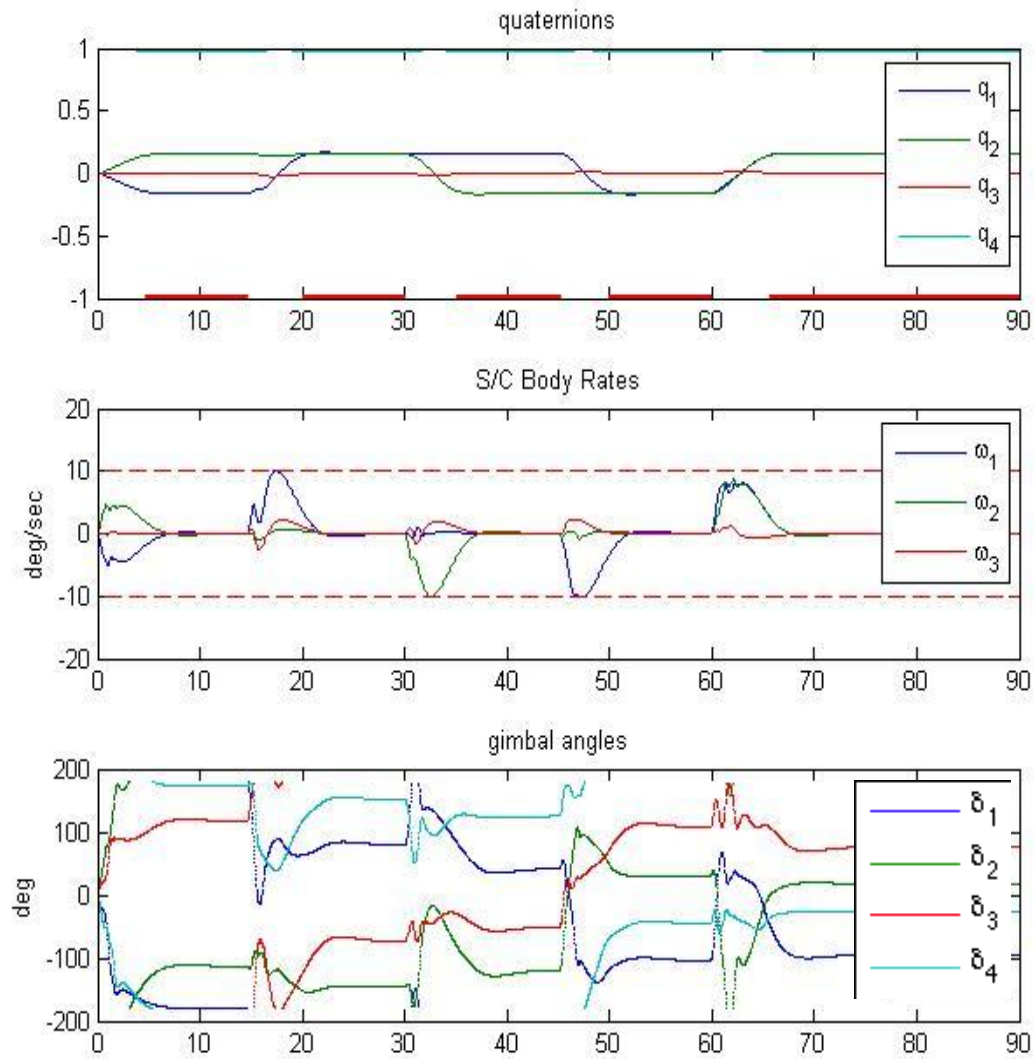Figure 3:   Simulation 1 Torque

94

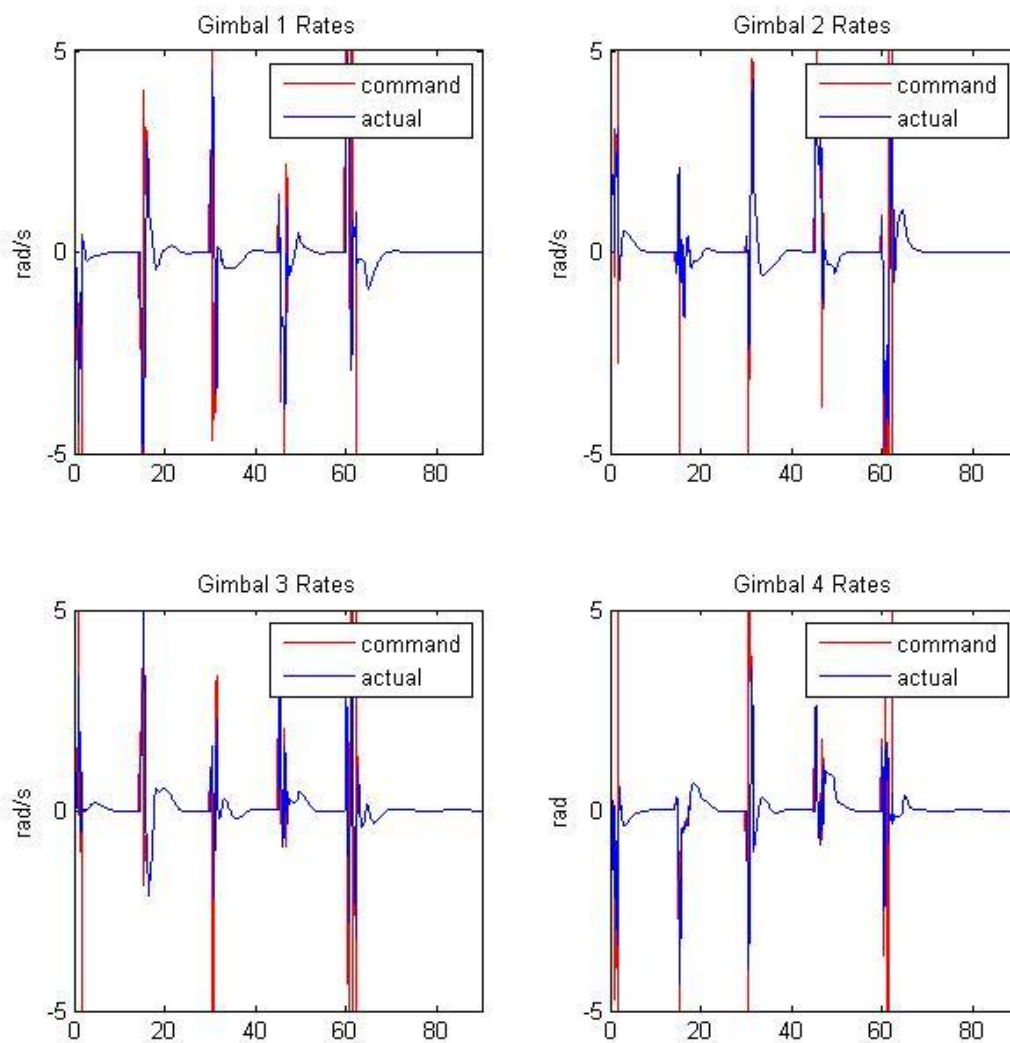Figure 4:   Simulation 2 Orientation, Rates, and Gimbal Positions

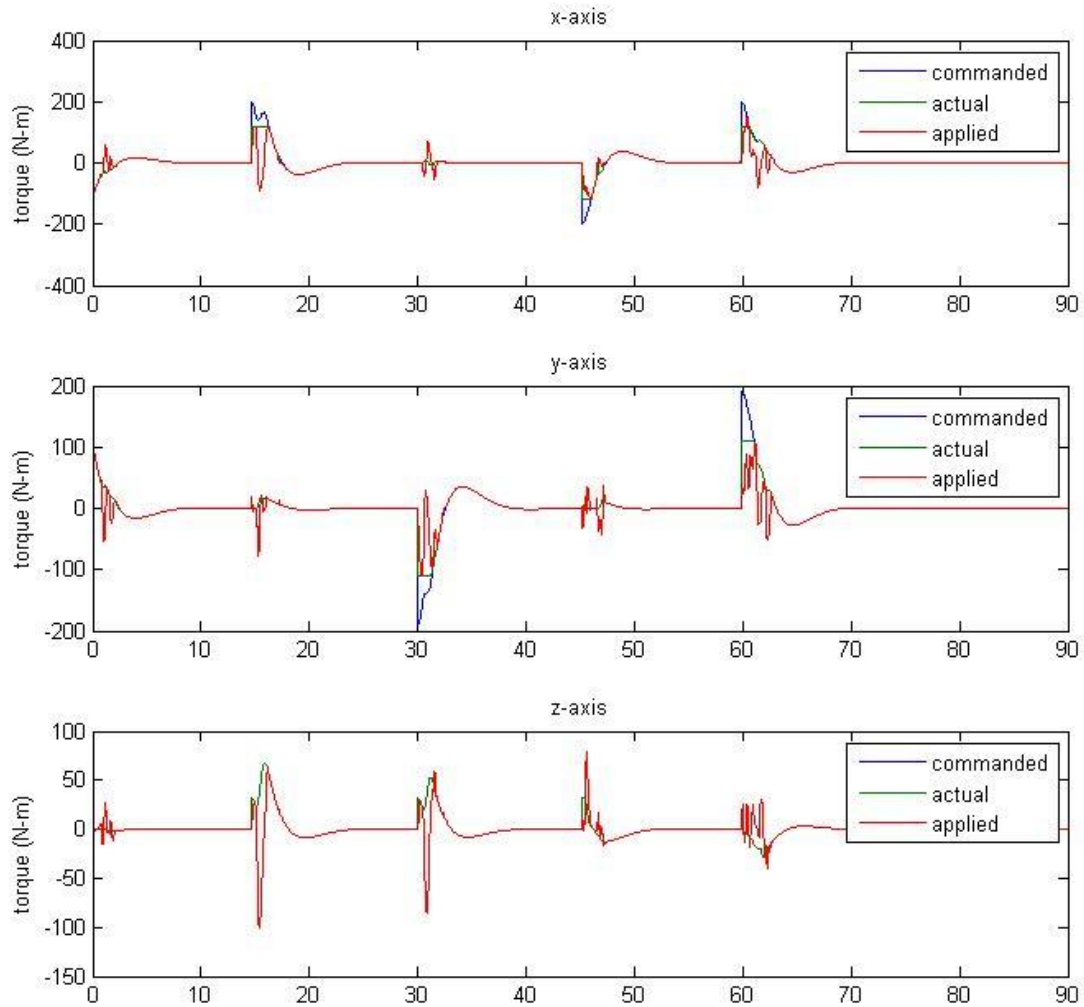Figure 5:   Simulation 2 Gimbal Rates

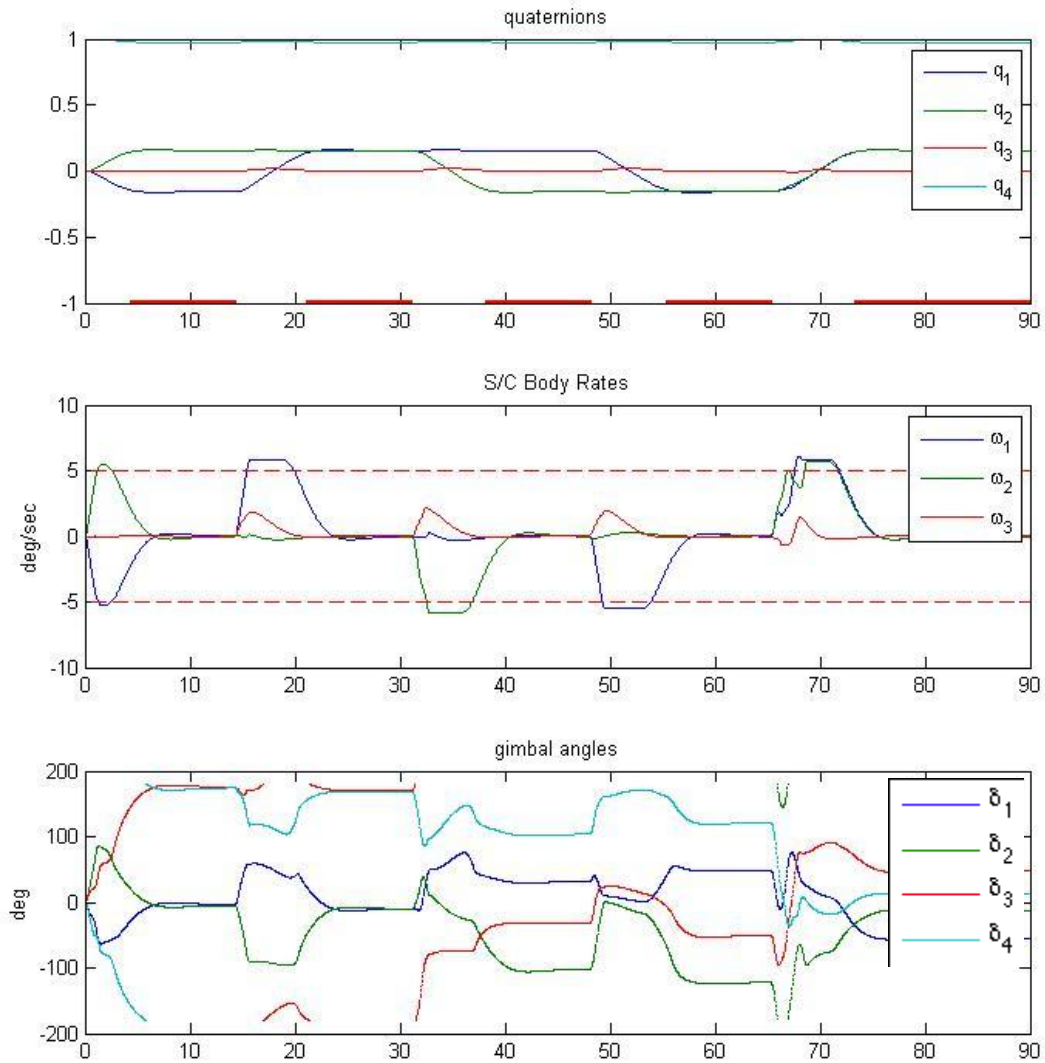Figure 6: Simulation 2 Torque

Figure 7:   Simulation 3 Orientation, Rates, and Gimbal Positions
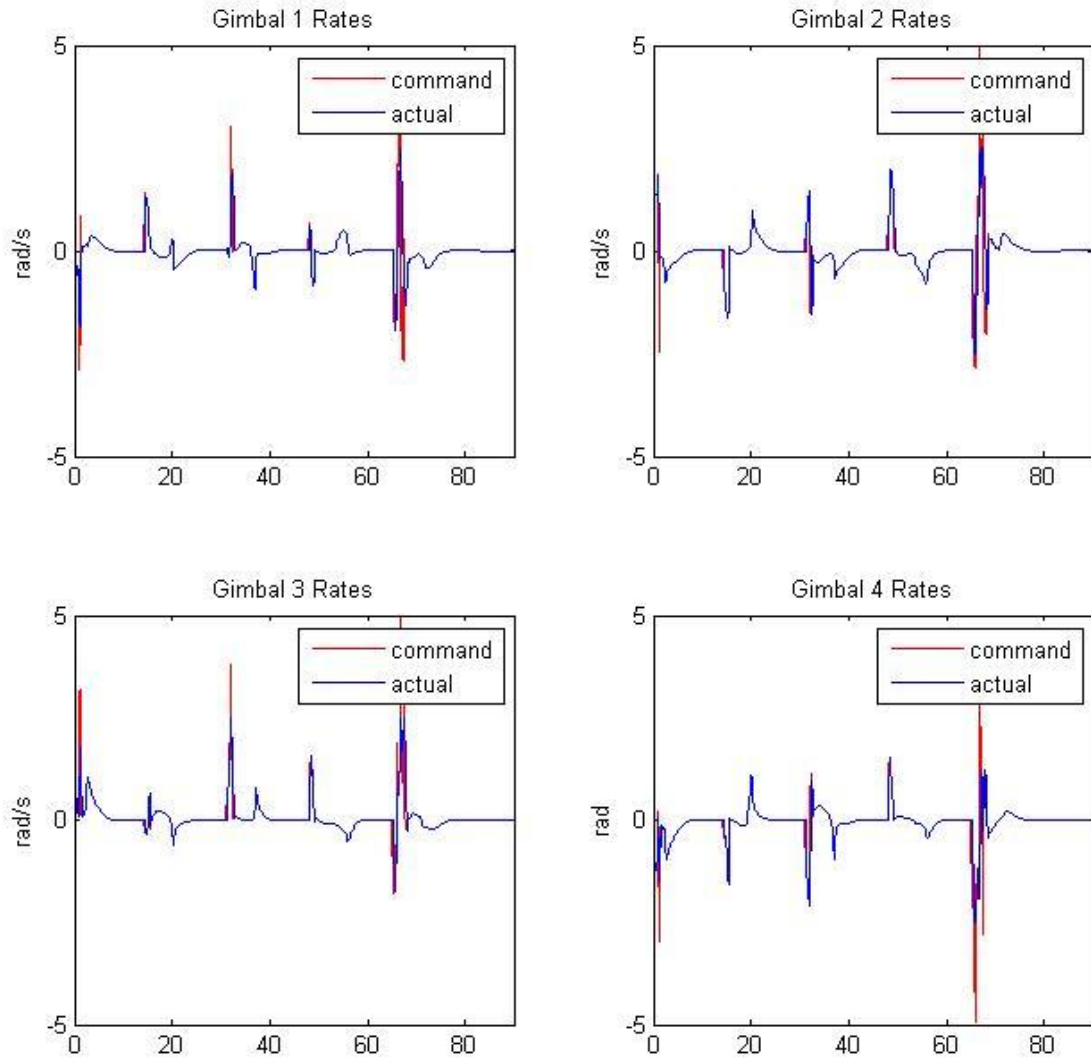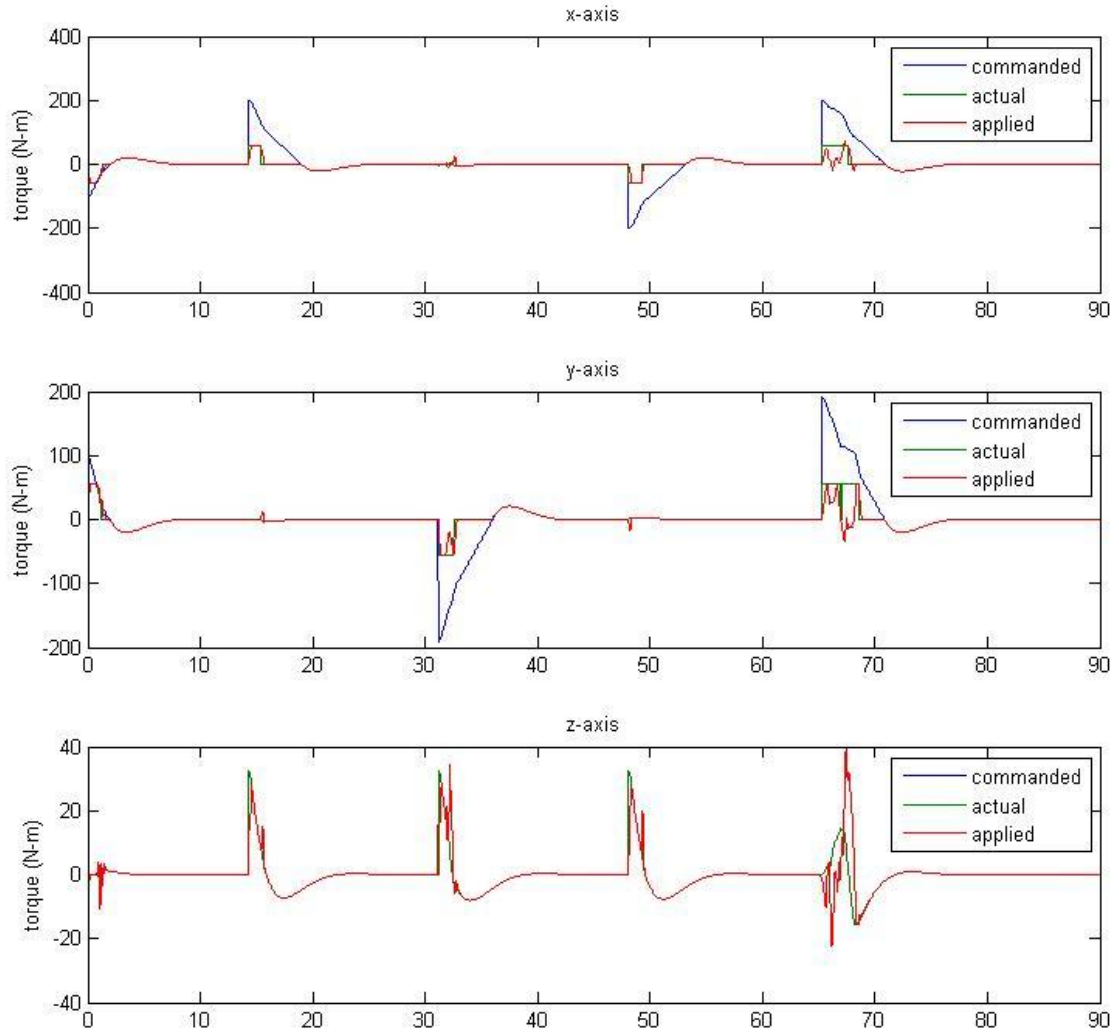
Figure 8:   Simulation 3 Gimbal Rates
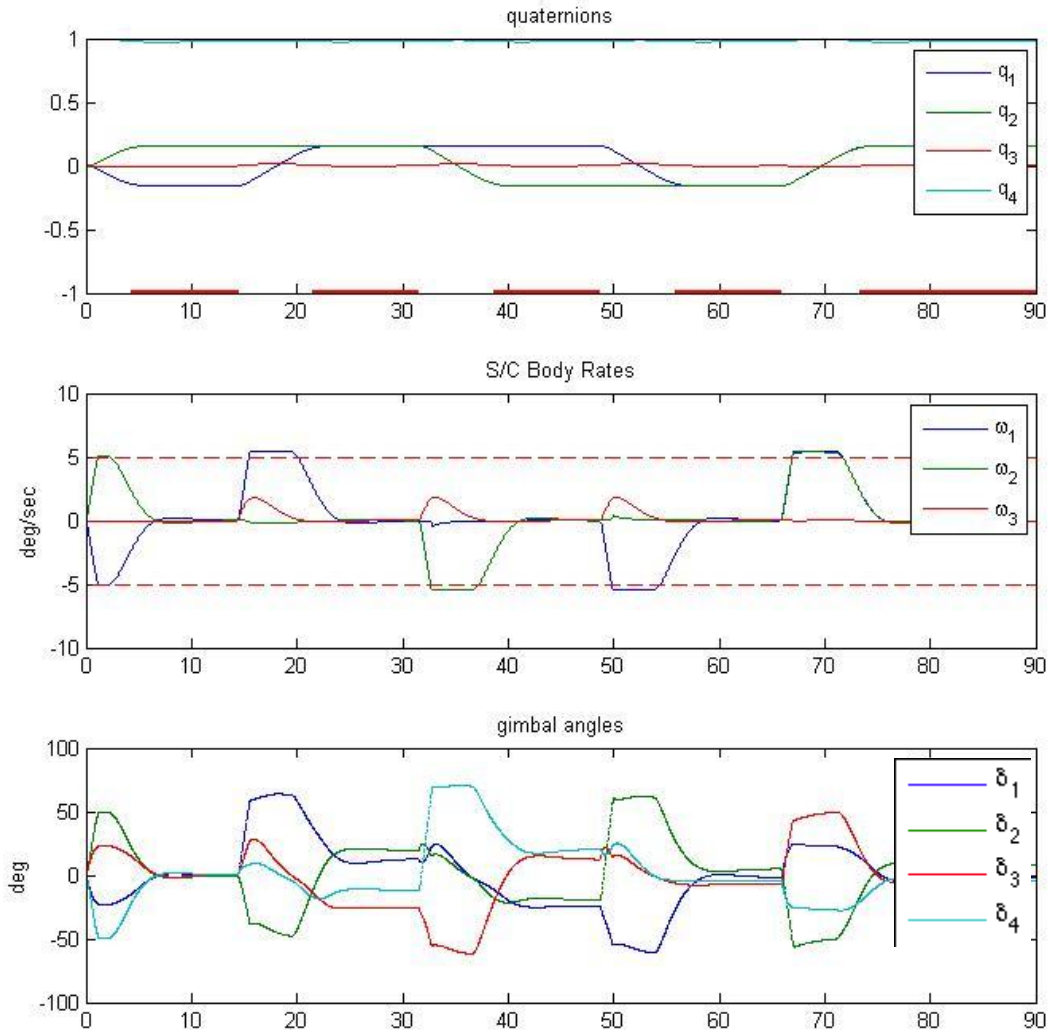
Figure 9:   Simulation 3 Torque

Figure 10:   Simulation 4 Orientation, Rates, and Gimbal Positions
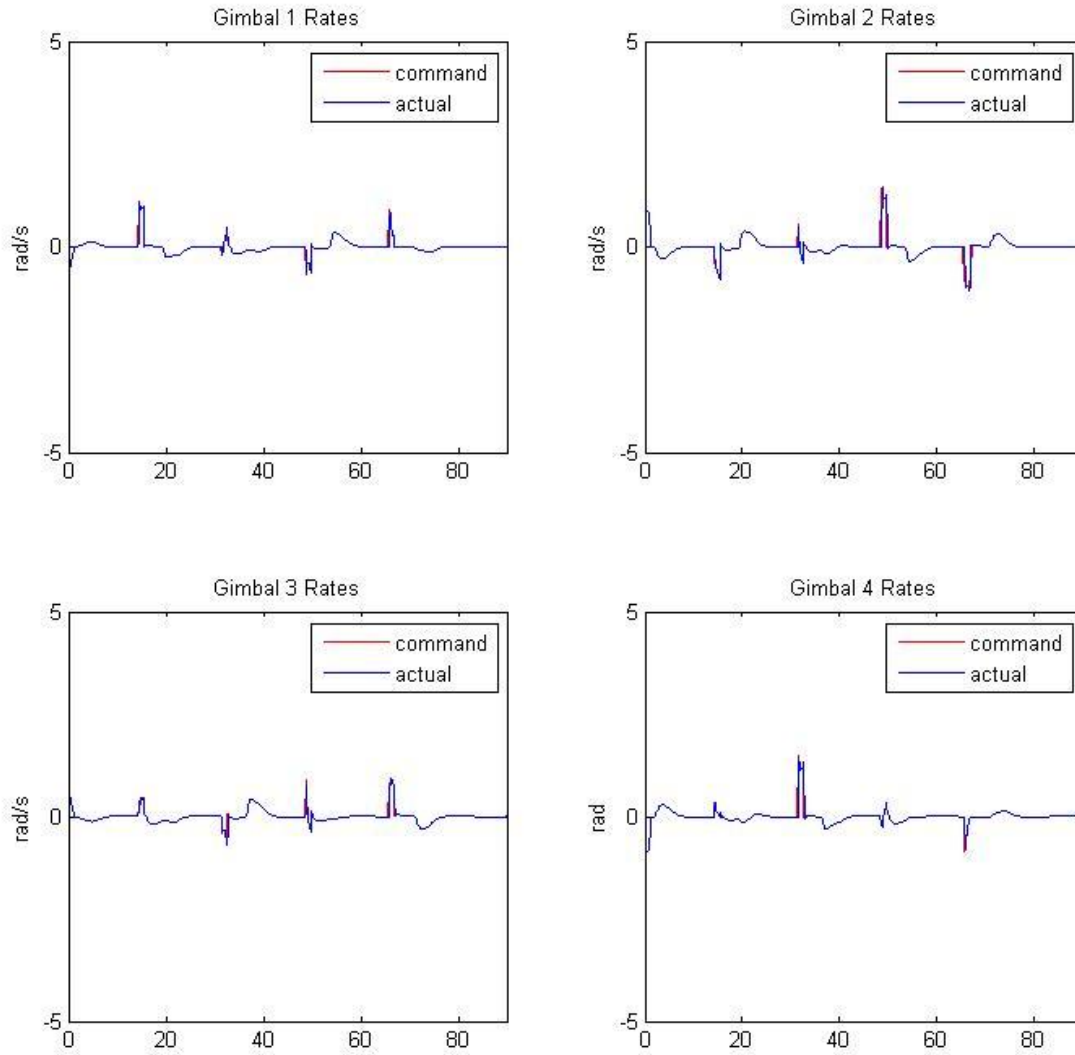
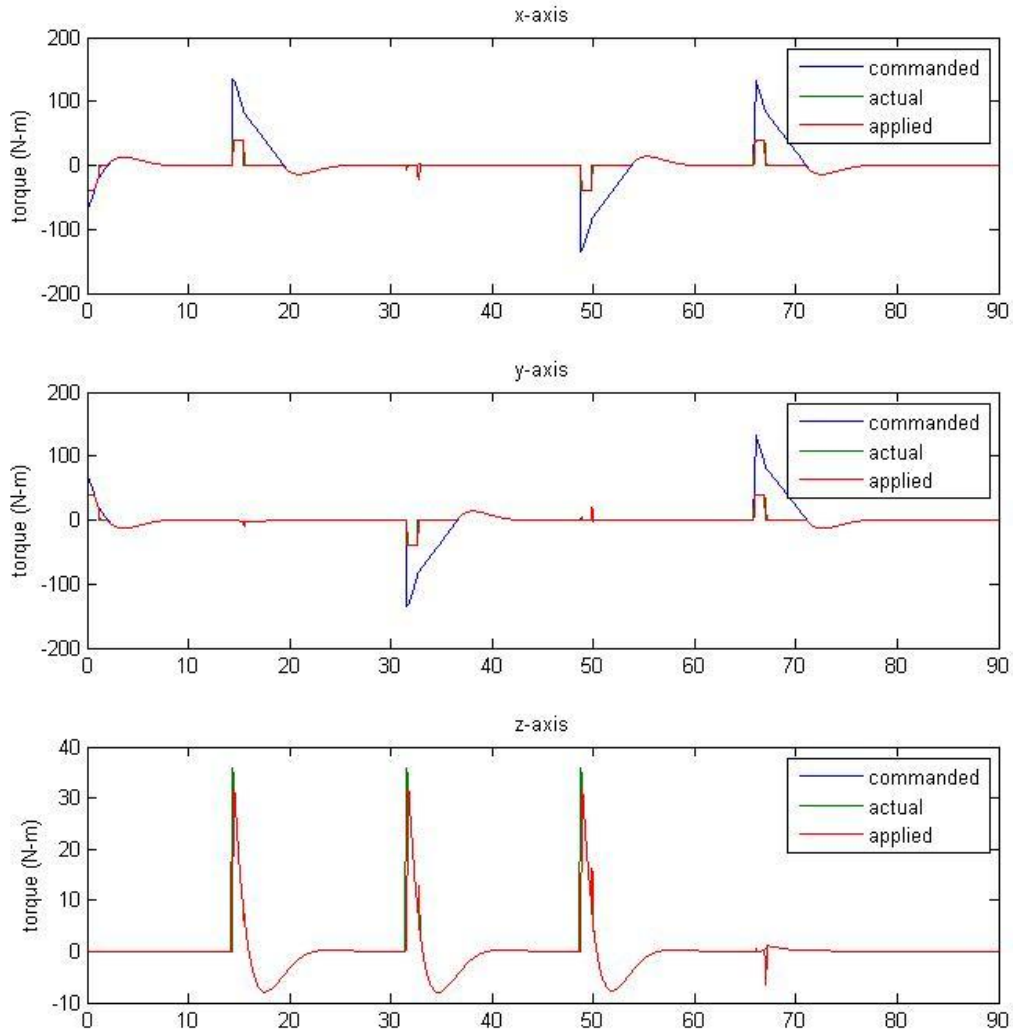Figure 11:   Simulation 4 Gimbal Rates
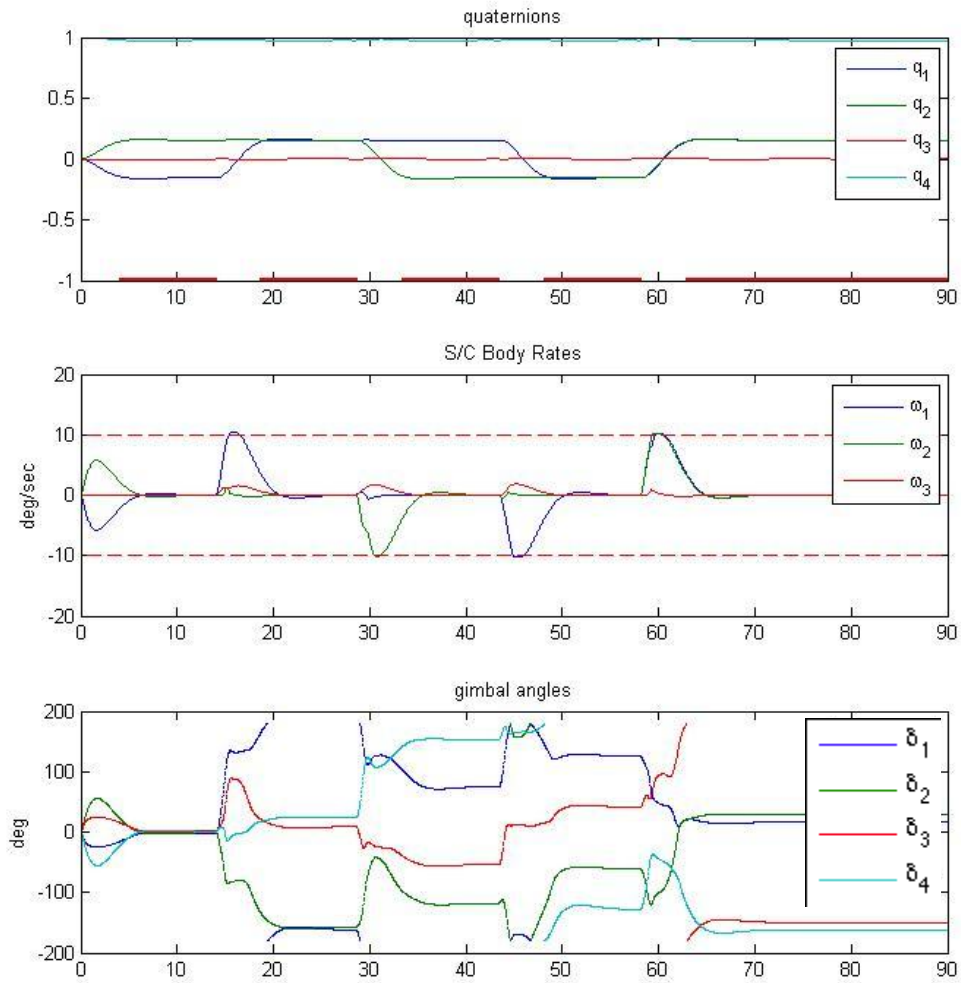
Figure 12:   Simulation 4 Torque

Figure 13:   Simulation 5 Orientation, Rates, and Gimbal Positions
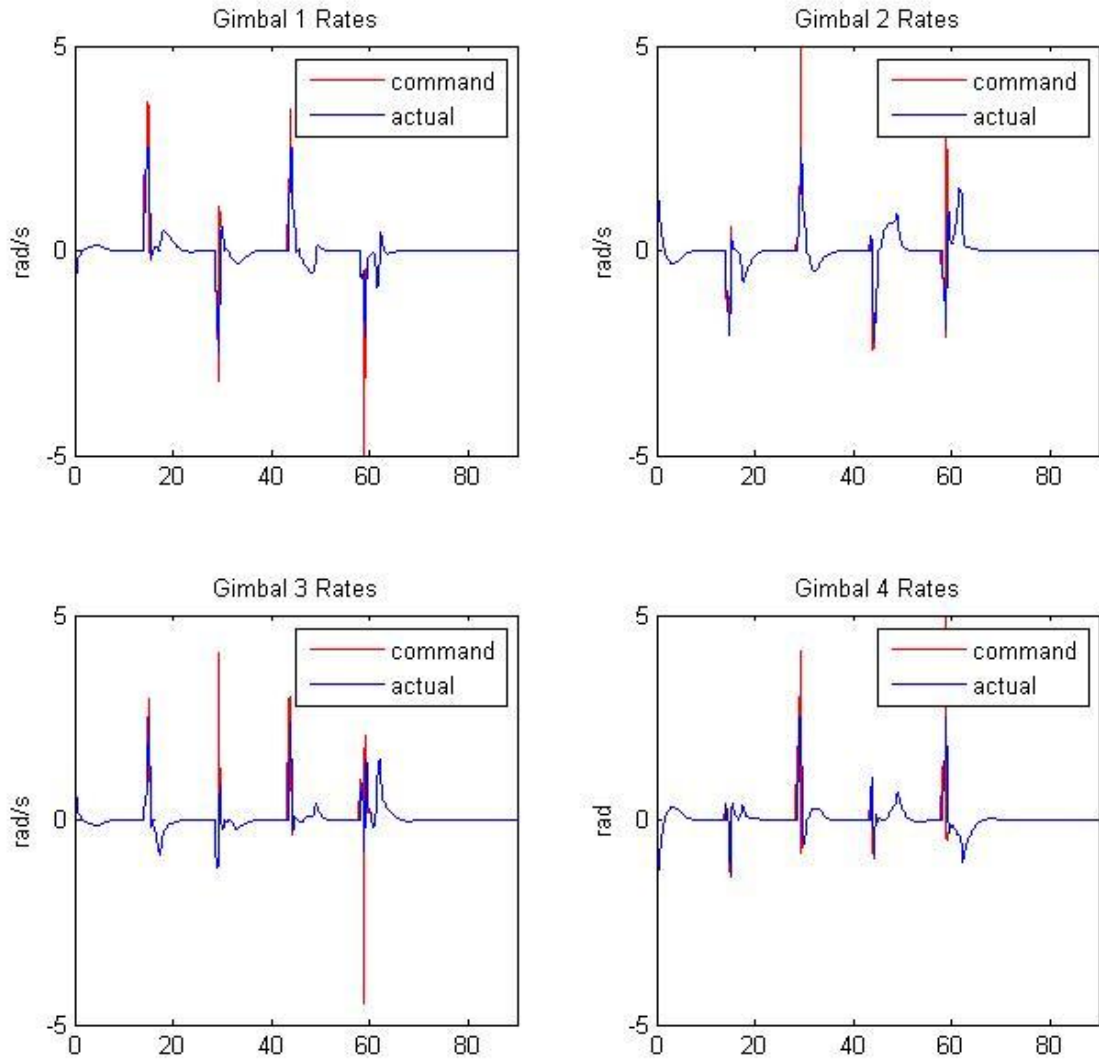
104

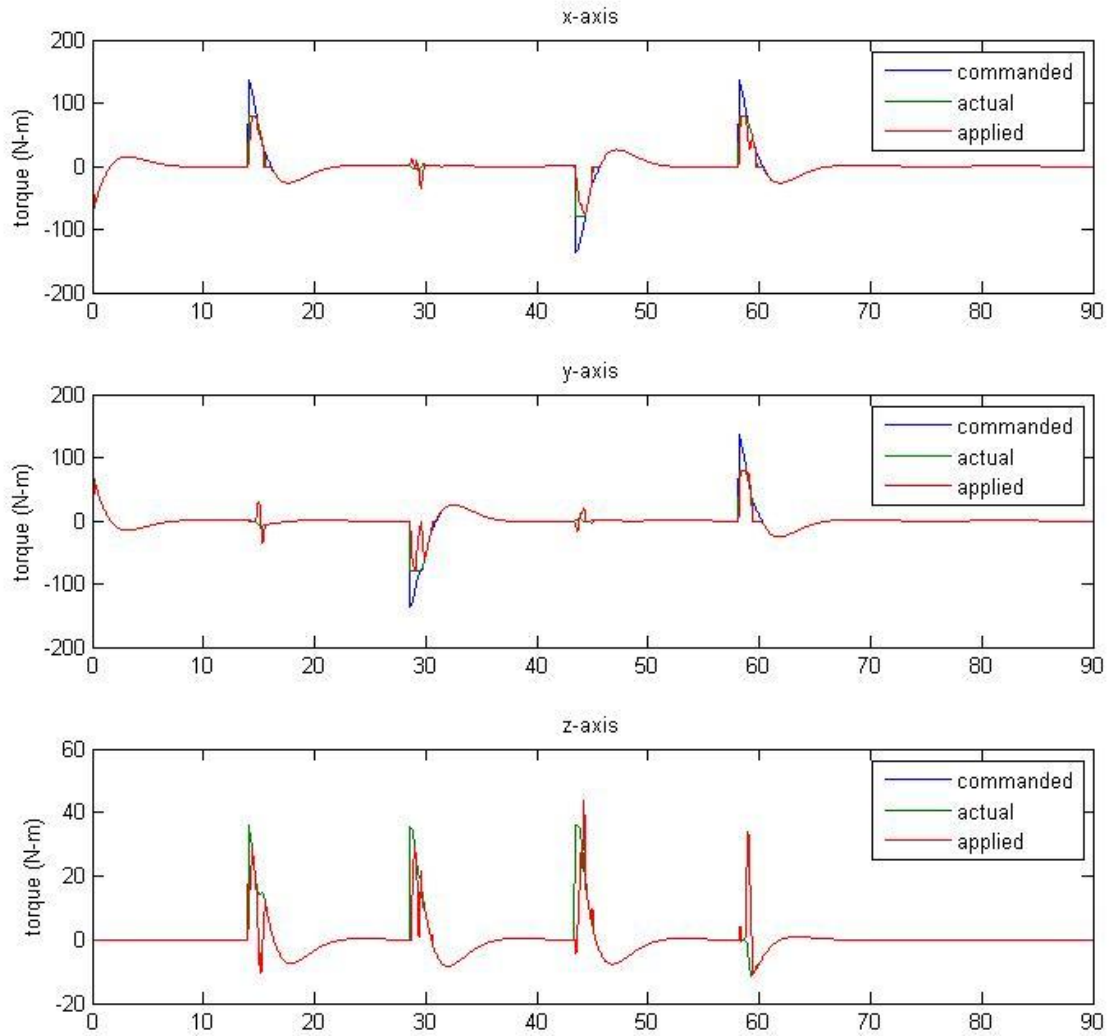Figure 14: Simulation 5 Gimbal Rates

Figure 15:   Simulation 5 Torque

Bibliography

1. Barden Super Precision Ball Bearings - Specialty Products, 2010.

2. Wikipeda. Wikipedia: Attitude control, . URL `http://en.wikipedia.org/wiki/Attitude_control`.

3. Christopher McChesney. *Design of Attitude Control Actuators for a Simulated Spacecraft.* MS thesis, Air Force Institute of Technology (AU), March 2011.

4. Jerry J. Sellers. *Understanding Space: An Introduction to Astronautics.* The McGraw-Hill Companies, Inc., New York, 3rd edition, 2005.

5. ByungMoon Kim, Efstathios Velenis, Patrick. Kriengsiri, and Panagiotis Tsiotras. "A Spacecraft Simulator for Research and Education,". In *Astrodynamics Specialists Conference*, pages 897–914. AIAA/AAS, July 2001.

6. Jana L. Schwartz, Mason A. Peck, and Christopher D. Hall. "Historical Review of Spacecraft Simulators". *Journal of Guidance, Control, and Dynamics*, 26(4):513–522, 2003.

7. NASA. Nasa/jsc neutral buoyancy lab overview, . URL `http://http://dx12.jsc.nasa.gov/about/index.shtml`.

8. NASA. Nasa glenn research center zero gravity facility overview, . URL `http://facilities.grc.nasa.gov/zerog`.

9. NASA. Nasa/jsc aircraft operations reduced gravity research program, . URL `http://jsc-aircraft-ops.nasa.gov/Reduced_Gravity/index.html`.

10. James E. Colebank, Robert D. Jones, George R. Nagy, Randall D. Pollack, and Donald R. Mannebach. *SIMSAT: A Satellite System Simulator and Experimental Test Bed for Air Force Research.* MS thesis, Air Force Institute of Technology (AU), March 1999. ADA361635.

11. David B. French. *Hybrid Control Strategies for Rapid, Large Angle Satellite Slew Maneuvers.* MS thesis, Air Force Institute of Technology (AU), March 2003. ADA412869.

12. Joseph M. Fulton. *Attitude Control and Multimedia Representation of Air Force Institute of Technology's (AFIT'S) Simulation Satellite (SIMSAT).* MS thesis, Air Force Institute of Technology (AU), March 2000. ADA380275.

13. Vincent J. Dabrowski. *Experimental Demonstration of an Algorithm to Detect the Presence of a Parasitic Satellite.* MS thesis, Air Force Institute of Technology (AU), March 2003.

14. Matthew B. Kimsal. *Design of a Space-Borne Autonomous Infrared Tracking System.* MS thesis, Air Force Institute of Technology (AU), March 2004. ADA425222.

15. Jason E. Smith. *Attitude Model of a Reaction Wheel/Fixed Thruster Based Satellite Using Telemetry Data.* MS thesis, Air Force Institute of Technology (AU), March 2005. ADA437523.

16. Jason W. Geitgey. *The Determination of Remaining Satellite Propellant Using Measured Moments of Inertia.* MS thesis, Air Force Institute of Technology (AU), June 2006. ADA453964.

17. Michael S. Hines. *Fuel Estimation Using Dynamic Response.* MS thesis, Air Force Institute of Technology (AU), March 2007. ADA469309.

18. Neal R. Roach, Wayne C. Rohe, and Nathan F. Welty. *A Systems Engineering Approach to the Design of a Spacecraft Dynamics and Control Testbed.* MS thesis, Air Force Institute of Technology (AU), March 2008.

19. C. Douglas McFarland. *Near Real-Time Closed-Loop Optimal Control Feedback for Spacecraft Attitude Maneuvers.* MS thesis, Air Force Institute of Technology (AU), March 2009. ADA496781.

20. Ryan E. Snider. *Attitude Control of a Satellite Simulator Using Reaction Wheels and a PID Controller.* MS Thesis, Air Force Institute of Technology (AU), March 2010.

21. Jorge Padro. *Development of a Star Tracker-Based Reference System for Accurate Attitude Determination of a Simulated Spacecraft.* MS thesis, Air Force Institute of Technology (AU), March 2012.

22. Jonathan Wright, Eric Swenson, and Fred Leve. "Hardware Testing of Hybrid Steering Logic for Single-Gimbal Control Moment Gyroscopes,". Technical Report AIAA 2012-4971, Air Force Institute of Technology, 2012.

23. Hyochoong Bang. University Nano-Satellite Activites in Korea: Current Status and Vision. 2010. URL `http://park.itc.u-tokyo.ac.jp/nsat/NS1/files/10th.AM/Presentation_Hyochoong-Bang.pdf`.

24. Peter C Hughes. *Spacecraft Attitude Dynamics*. Dover Publications, Inc, 31 East 2nd Street, Mineola, NY 11501, 2nd edition, 2004, 1986.

25. Leonhard Euler. General formulas for the translation of an arbitrary rigid body. URL `http://www.17centurymaths.com/contents/euler/e478tr.pdf`. Translation of original text published by Johan Sten.

26. John Schaub, Hanspeter & Junkins. *Analytical Mechanics of Space Systems*. AIAA Education Series. AIAA Education Series, 2nd edition, 2009.

27. William E. Wiesel. *Spaceflight Dynamics*. McGraw-Hill, 2nd edition, 1995.

28. Wikipeda. Wikipedia: Iss, . URL `http://en.wikipedia.org/wiki/International_Space_Station`.

29. Ball Aerospace DigitalGlobe. Digitalglobe fact sheet: Worldview-2. URL `http://www.digitalglobe.com/index.php/88/WorldView-2`.

30. Frederick A. Leve. *Novel Steering and Control Algorithms for Single-Gimbal Control Moment Gyroscopes*. PhD thesis, The University of Florida, 2010.

31. Gilbert Strang. *Linear Algebra and its Applications*. Thompson Corporation, 10 Davis Drive Belmont, CA 94002-3098, 4th edition, 2006.

32. P. L. Palmer S. Asghar and M. Roberts. Exact steering law for pyramid-type four control moment gyro systems. In *AIAA/AAS Astrodynamice Specialist Conference*, 2006.

33. Katsuhiko Ogata. *Modern Control Engineering*. Prentice-Hall, New Jersey, 4th edition, 2002.

34. Weiping Li Jean-Jacques Slotine. *Applied Nonlinear Control.* Prentice-Hall International, Upper Saddle River, New Jersy 07458, 1991.

35. Michael Faraday. Faraday's law of induction. URL `http://en.wikipedia.org/wiki/Faraday's_law_of_induction`.

36. Reston Condit. "Brushed DC Motor Fundamentals". Technical report.

37. Padmaraja Yedamale. Brushless dc motor fundamentals, 2003.

38. "Balance Quality Requirements of Rigid Rotors: The Practical Application of ISO 1940/1". Technical report, 2009.

39. Charles Gurrisi, Raymond Seidel, Scott Dickerson, Stephen Didziulis, Peter Frantz, and Kevin Ferguson. 'Space Stating Control Moment Gyroscope Lessons Learned". Number NASA/CP-2010-316272. NASA, 2010.

40. "M50 Control Moment Gyroscope".

REPORT DOCUMENTATION PAGE

Form Approved
OMB No. 0704–0188

The public reporting burden for this collection of information is estimated to average 1 hour per response, including the time for reviewing instructions, searching existing data sources, gathering and maintaining the data needed, and completing and reviewing the collection of information. Send comments regarding this burden estimate or any other aspect of this collection of information, including suggestions for reducing this burden to Department of Defense, Washington Headquarters Services, Directorate for Information Operations and Reports (0704–0188), 1215 Jefferson Davis Highway, Suite 1204, Arlington, VA 22202–4302. Respondents should be aware that notwithstanding any other provision of law, no person shall be subject to any penalty for failing to comply with a collection of information if it does not display a currently valid OMB control number. PLEASE DO NOT RETURN YOUR FORM TO THE ABOVE ADDRESS.

1. REPORT DATE (DD–MM–YYYY) 21-03-2013	2. REPORT TYPE Master's Thesis	3. DATES COVERED (From — To) Jun 2012 – Mar 2013

4. TITLE AND SUBTITLE Design of a Control Moment Gyroscope Attitude Actuation System For the Attitude Control Subsystem Proving Ground	5a. CONTRACT NUMBER
	5b. GRANT NUMBER
	5c. PROGRAM ELEMENT NUMBER

6. AUTHOR(S) Johnson, Samuel C, 2Lt, USAF	5d. PROJECT NUMBER
	5e. TASK NUMBER
	5f. WORK UNIT NUMBER

7. PERFORMING ORGANIZATION NAME(S) AND ADDRESS(ES) Air Force Institute of Technology Graduate School of Engineering and Management (AFIT/ENY) 2950 Hobson Way WPAFB OH 45433-7765	8. PERFORMING ORGANIZATION REPORT NUMBER AFIT-ENY-13-M-19

9. SPONSORING / MONITORING AGENCY NAME(S) AND ADDRESS(ES) Frederick Leve, Ph.D., Research Aerospace Engineer, Air Force Research Laboratory / Space Vehicles Directorate, Guidance Navigation and Control Group 3550 Aberdeen Ave, SE Kirtland AFB, NM 87117 Phone: (505) 853-7476	10. SPONSOR/MONITOR'S ACRONYM(S) AFRL/RV
	11. SPONSOR/MONITOR'S REPORT NUMBER(S)

12. DISTRIBUTION / AVAILABILITY STATEMENT
Distribution Statement A: APPROVED FOR PUBLIC RELEASE; DISTRIBUTION UNLIMITED

13. SUPPLEMENTARY NOTES This material is declared a work of the U.S. Government and is not subject to copyright protection in the United States.

14. ABSTRACT
It is the author's contention that there is room to improve the design process for lab-rated control moment gyroscopes (CMGs). Therefore, a framework for designing CMGs was developed. This framework was then used to design CMGs for the Attitude Control Subsystem Proving Ground (ACSPG), a simulated satellite operated by Air Force Research Laboratories (AFRL). This design and the methodology that led to this design is then presented. Simulation of the attitude control subsystem is also presented.

15. SUBJECT TERMS
Controls CMG "Simulated Satellite" "Control Moment Gyroscope" Design

16. SECURITY CLASSIFICATION OF:			17. LIMITATION OF ABSTRACT	18. NUMBER OF PAGES	19a. NAME OF RESPONSIBLE PERSON Dr. Eric Swenson, ENY
a. REPORT U	b. ABSTRACT U	c. THIS PAGE U	UU	126	19b. TELEPHONE NUMBER (Include Area Code) (937)255-3636, ext 7479 eric.swenson@afit.edu

Standard Form 298 (Rev. 8–98)
Prescribed by ANSI Std. Z39.18